High-pressure studies with x-rays using diamond anvil cells

2017 Rep. Prog. Phys. 80 016101

(http://iopscience.iop.org/0034-4885/80/1/016101)

IOP Publishing Reports on Progress in Physics
Rep. Prog. Phys. **80** (2017) 016101 (53pp) doi:10.1088/1361-6633/80/1/016101

Review

High-pressure studies with x-rays using diamond anvil cells

Guoyin Shen[1] **and Ho Kwang Mao**[1,2]

[1] Geophysical Laboratory, Carnegie Institution of Washington, Washington DC, USA
[2] Center for High Pressure Science and Technology Advanced Research, Shanghai, People's Republic of China

E-mail: hmao@carnegiescience.edu and gshen@carnegiescience.edu

Received 16 April 2015, revised 30 August 2016
Accepted for publication 30 September 2016
Published 22 November 2016

Corresponding Editor J Murray Gibson

Abstract

Pressure profoundly alters all states of matter. The symbiotic development of ultrahigh-pressure diamond anvil cells, to compress samples to sustainable multi-megabar pressures; and synchrotron x-ray techniques, to probe materials' properties *in situ*, has enabled the exploration of rich high-pressure (HP) science. In this article, we first introduce the essential concept of diamond anvil cell technology, together with recent developments and its integration with other extreme environments. We then provide an overview of the latest developments in HP synchrotron techniques, their applications, and current problems, followed by a discussion of HP scientific studies using x-rays in the key multidisciplinary fields. These HP studies include: *HP x-ray emission spectroscopy*, which provides information on the filled electronic states of HP samples; *HP x-ray Raman spectroscopy*, which probes the HP chemical bonding changes of light elements; *HP electronic inelastic x-ray scattering spectroscopy*, which accesses high energy electronic phenomena, including electronic band structure, Fermi surface, excitons, plasmons, and their dispersions; *HP resonant inelastic x-ray scattering spectroscopy*, which probes shallow core excitations, multiplet structures, and spin-resolved electronic structure; *HP nuclear resonant x-ray spectroscopy*, which provides phonon densities of state and time-resolved Mössbauer information; *HP x-ray imaging*, which provides information on hierarchical structures, dynamic processes, and internal strains; *HP x-ray diffraction*, which determines the fundamental structures and densities of single-crystal, polycrystalline, nanocrystalline, and non-crystalline materials; and *HP radial x-ray diffraction*, which yields deviatoric, elastic and rheological information. Integrating these tools with hydrostatic or uniaxial pressure media, laser and resistive heating, and cryogenic cooling, has enabled investigations of the structural, vibrational, electronic, and magnetic properties of materials over a wide range of pressure-temperature conditions.

Keywords: high pressure, diamond anvil cell, x-ray diffraction, x-ray spectroscopy, x-ray imaging, synchrotron radiation

(Some figures may appear in colour only in the online journal)

1. Introduction

1.1. High pressure—a dimension in physical sciences

Pressure (P) is an intensive variable, defined as a measure of how the internal energy of a system changes when it expands or contracts at constant entropy (S) or temperature (T):

$$P = -\left(\frac{\partial E}{\partial V}\right)_S = -\left(\frac{\partial F}{\partial V}\right)_T \tag{1.1}$$

where E, F, V are internal energy; Helmholtz free energy; and volume, respectively. As a fundamental thermodynamic variable, with one of the largest ranges [1], pressure is not only widely used to describe the extreme conditions of materials (such as those existing in impacts and detonations, or inside the Earth and celestial bodies), but it is also experimentally controlled to induce several important effects on interatomic interactions [2, 3]. Pressure tunes and alters all chemical, structural, mechanical, electronic, magnetic, and phonon properties. It pushes materials across boundaries between soft and superhard, brittle and ductile, insulating and metallic, ferromagnetic and superconducting, amorphous and crystalline, ionic and covalent, and vigorously reactive and inert. The recent development of synchrotron radiation (SR) probes [3–6] has opened a vast new window for studying materials *in situ* at high-pressure (HP), and at temperatures varying from cryogenic to thousands of degrees [7]. Indeed, pressure provides a fundamental dimension in physical sciences, and surprising HP physics and HP chemistry are revealed. Under high pressures, many new 'rules' in chemistry are established; novel materials are formed and discovered, and various routes for recovery to ambient pressure are established and explored. HP studies are crucial for understanding the interior mineralogy, composition, dynamics, and formation of candidate materials inside the Earth and celestial bodies. The impact of HP science has been widely recognized, particularly in the last decade with the synergy between advances in pressure vessel design and *in situ* probes.

1.2. Synchrotron x-rays—penetrating probes for minute high pressure samples

Pressure can be also viewed as the force acting perpendicularly on a unit area. Therefore, static high pressures are generated in laboratories at the expense of reducing sample volumes. At multi-megabar pressures, sample dimensions are typically less than 30 μm. To investigate physical and chemical properties *in situ* under HP, powerful penetrating microsampling probes must be developed to reach the minute samples through the wall of the pressure vessel and to separate the weak sample signals from the background signals of the massive surrounding vessel materials. The arrival of SR x-ray sources provides a perfect solution (figure 1). Since the 1980s, great efforts have been made to take advantage of the characteristics of SR for HP research, including: (1) high intensity over a broad energy range, (2) low emittance (small angular divergence), (3) tunable energy and bandwidth with the use of monochromators, (4) pulsed time structure, (5) polarization of the radiation, and (6) coherence of the x-ray wave. Recently constructed synchrotron facilities have achieved a high degree of orbit stability [8, 9], providing highly stable x-ray beams in terms of intensity and position that are critical for HP experiments. The unique SR characteristics are unleashing the rich potential of HP science.

HP science has become an important field for the application of SR. For instance, the spatial resolution and intensity of conventional x-ray, neutron, and ultrasonic sources are insufficient for resolving the μm-size samples at megabar pressures, while the conventional microprobes using focused ultraviolet radiation (UV microscopy), electrons (electron microscopy), ions (SIMS), or near-surface contacts (atomic force microscopy) require a vacuum environment which is opposite to the HP condition. The arrival of high-energy SR thus enjoys the unique advantage of exploring the vast frontier opened up for SR-HP applications. The high brightness of SR has enabled the development of various HP-SR techniques. Continuously tunable wavelength opens up new capabilities, in particular in HP x-ray spectroscopy and HP inelastic x-ray scattering [10–12]. The pulsed timing structure, together with the high brilliance, allows the study of time dependent phenomena [13, 14] such as phase transition kinetics, chemical reaction processes, transport phenomena, and metastable phases at HP and high/low temperatures. The polarization of synchrotron radiation has been extensively utilized for studying magnetic systems at HP [15, 16], while the coherence has been used for mapping structure and strain in nanometer-scale grains [17–19].

During the past decade, we have witnessed extraordinary advances in HP-SR studies, largely reflected in three frontiers. First, HP research is made much more versatile by integrating other dimensions of extreme environments, such as temperature, magnetic field, radiation flux. Secondly, while each individual SR technique, coupled with HP samples, provides a valuable probe for a specific property, the combination of several techniques forms a comprehensive toolbox for addressing major questions. Thirdly, HP-SR research impacts on multidisciplinary fields, including physics [20], chemistry [21], material sciences [22], geosciences [23, 24], and biosciences [25], and is driven by the scientific agendas of each community.

This article is organized according to the development of these three frontiers. We will first introduce the essential concept of diamond anvil cell technology, together with recent developments and its integration with other extreme environments. This is followed by the latest developments in HP-SR techniques, their applications, and current problems. We will then discuss the key multidisciplinary fields of HP scientific studies using x-rays. The focus is to summarize the fast-paced progress in the past decade, with the key background briefly discussed.

2. Generation of high pressure—the diamond anvil cell technology

Among commonly used HP apparatus are diamond anvil cells (DACs), large volume presses (LVP), and shock wave devices. DACs are capable of generating pressures beyond 400 GPa

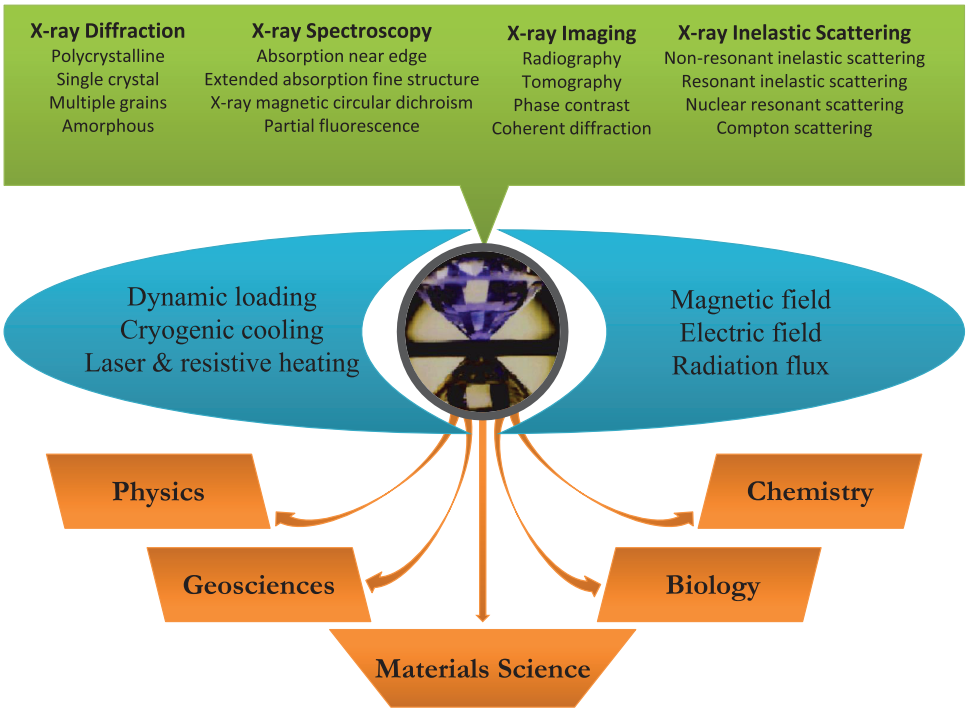

Figure 1. Various x-ray probes have been developed to study samples under extreme environments and their applications to multidisciplinary sciences.

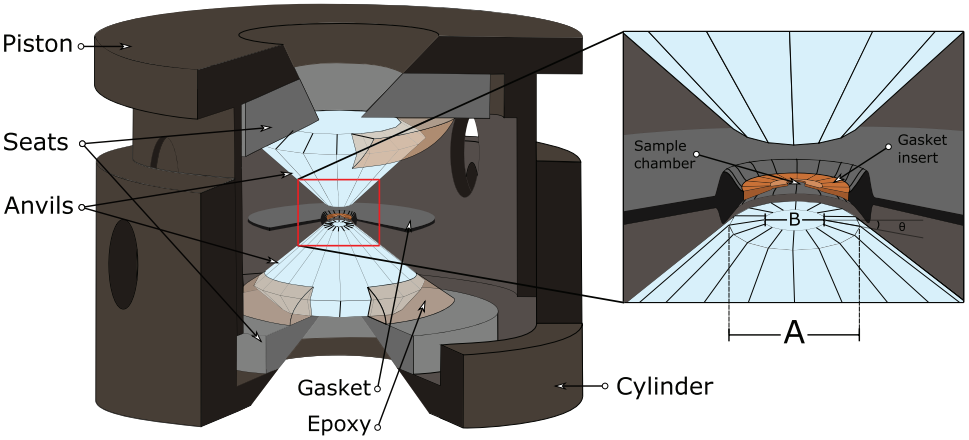

Figure 2. Illustration of the three basic components of a diamond anvil cell: opposing anvils, a confining gasket, and sample chamber. A beveled-anvil geometry is shown with culet size A beveled to B at a bevel angle θ.

[26, 27] (with a record claimed beyond 1 TPa). LVP generates modest pressures (currently up to 109 GPa) [28], with a relatively large sample volume, as the name infers. In shock wave experiments, the sample is subjected to transient high pressures and temperatures by dynamic processes. Multi-megabars in excess of 100 megabar pressures may be generated in a short time scale ranging from nano- to femto-seconds [29]. Here, we focus our discussions on the DAC, which consists of three basic components: opposing anvils, a confining gasket, and sample chamber (figure 2).

2.1. Anvils

Single-crystal diamond is generally used as the anvil material, due to its outstanding properties including: the highest known hardness and fracture toughness, highest known thermal conductivity, very low friction and adhesion, ultra-high melting temperature, the highest electron dispersion, high dielectric breakdown, radiation hardness, high magnetic-field compatibility, and biocompatibility. These properties have been exploited in the DAC techniques [30]. Diamond as the key anvil materials is adopted to endure the harshest extreme environments, and at the same time, as the window material for measurements with x-ray energies above 5 keV, UV–VIS–IR radiations below 5 eV, ultrasound, neutrons, and electric-magnetic probes [31, 32]. The DAC is the only static HP apparatus for studies in multi-megabar pressures regions [26, 27, 33], temperatures as high as 7000 K [34] and as low as 0.03 K [35], and a full range of *in situ* characterizations of material properties at controlled and defined extreme *P-T* conditions. Diamond is also of superior chemical inertness as a chamber in contact with a wide variety of samples, although

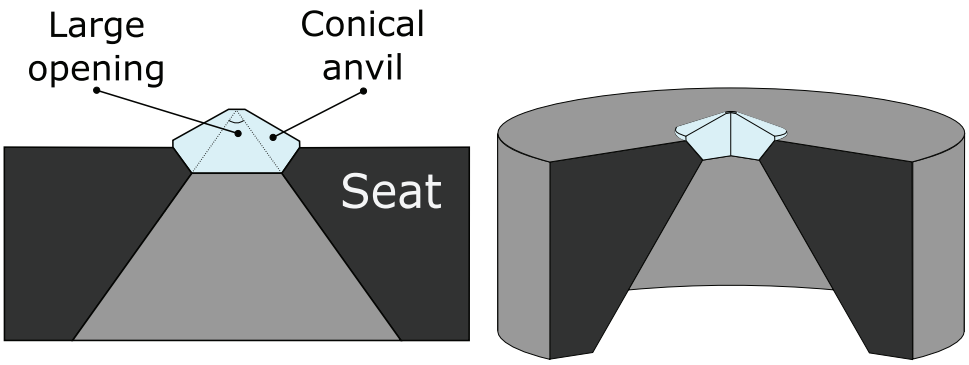

Figure 3. Geometry of Almax–Boehler type anvils supported by conically shaped areas, providing large access openings for optical and x-ray measurements.

there are reports showing that diamond can be attacked by some samples (e.g. Li [36]), and a trace amount of carbon from diamond may react with the sample (e.g. [37]). Sintered nanocrystalline diamond has been recently used as anvil material for its high strength, lack of single crystal x-ray reflections [38, 39], and its lower thermal conductivity in laser heating studies [40]. Other hard materials, such as sapphire and moissanite, have also been used for special applications, but with limited pressure ranges [41–43].

A typical diamond anvil has a small culet on one end and a large base (table facet) at the other end (figure 2). Recently, a conical anvil design has been introduced for large access openings [44]. The force applied to the table facet or the conical area of opposing anvils is transmitted directly to the small culet facet, where the pressure is amplified according to the area ratio. The anvils sustain increasing pressures up to the strength limit of the diamond. At extreme conditions, the diamond anvil in the culet region may deform elastically, to a large extent. For example, a bending of 17° within a 300 μm culet area has been observed [45, 46]. With such a large deformation, small defects or strain may cause fractures prematurely in diamond [7]. The quality of anvils becomes critical for reaching extremely HP conditions. Factors in selecting diamond anvils include: size, shape, birefringence, optical transparency, orientation, fluorescence, etc. For example, a well-tested, beveled-anvil geometry with culet size of 300 μm beveled to 50 μm at a bevel angle of 8.5° has been widely used for reaching above 300 GPa in DAC [47]. Using a double stage mechanism, pressures above 500 GPa have been reported [27, 48, 49]. However, so far no other groups have succeeded in generating similar high pressures using this technique [50, 51]. In particular, the pressure distribution around the tip of the second anvil remains unknown.

The diamond anvil also provides an axial window through the parallel table and culet facets. However, the extreme conditions require maximum mechanical support, by minimizing the angular opening of the seats supporting the tables, thus reducing the axial access to the sample. In addition, the diamond becomes increasingly absorbant of x-ray energies below 10 keV. For instance for Ce L_3-edge at 5.7 keV, the transmission is only 10^{-2} through 1 mm thick diamond, or 10^{-10} through the 5 mm thick pair of anvils. Progresses in several areas during the past decade have been made in resolving the access dilemma without sacrificing the HP capabilities. A new type of conical anvil and seat [44, 52] has much larger axial aperture (>90°) than the conventional flat seat supports (<40°). The larger support area of the conical seat allows significantly higher loads (figure 3). Bassett *et al* [53, 54] drilled holes or grooves on the diamonds to reduce the optical path through them down to several hundred microns, thus greatly reducing the diamond absorption between 5 and 10 keV and enabling HP x-ray spectroscopy of transition element *K*-edges (e.g. Mn [55] and Fe [56]) and rare-earth element *L*-edges (e.g. Ce [57, 58]). Perforated and partially perforated anvils have been commercially available and widely used for either reducing the diamond absorption [59] or minimizing the background scattering signals from the anvils [60, 61]. The development of panoramic DAC with the Be gasket [62, 63] or other low-*Z* materials [64] opened windows through the radial direction (i.e. perpendicular to the compression axis), and overcame both the geometric and absorption constraints of the conventional DAC.

The so-called designer anvils with diamond encapsulated thin-film microcircuits have been fabricated and used for HP electrical conductivity and magnetic susceptibility measurements [65, 66]. The embedded leads or coils are electrically insulated from the metallic gaskets commonly used. Such diamond encapsulated probes remain functional to multi-megabar pressures.

2.2. Gaskets

The gasket is an essential component in the DAC and serves several critical functions, including supporting the pressure by virtue of the anvil-gasket friction and encapsulating the sample. In some applications, the gasket may be used as windows for x-ray and neutron radiations, and/or outlets for electrical probes. High strength metals are often chosen as gasket materials. A gasket must also possess a certain level of ductility to allow the volume reduction corresponding to the pressure increase in the sample chamber. Around the diamond culet area, the gasket forms a thick ring that supports the anvils like a belt (figure 2), without which the anvils would not survive above 30–40 GPa. The effectiveness of the support depends on the tensile strength and thickness of the gasket. Between two parallel culets, the gasket sustains a large pressure

gradient from the minimum stress at the edge of the culet to the maximum stress near the center. In HP experiments above ~30 GPa, the gasket thickness (l) no longer depends upon its initial thickness; it is rather an intrinsic behavior of the gasket material related to a function of the shear strength (σ) and the pressure gradient along the radius (r) [67, 68].

$$l = 2\sigma/(\partial P/\partial r) \tag{2.1}$$

Various materials are used as gaskets to optimize specific functions and experimental goals. Hardened steel, high strength tungsten and rhenium are among the commonly used gasket materials. Composite gaskets can be constructed to optimize different functions at different parts of the gasket, e.g. insulating inserts (MgO, Al_2O_3 or cBN) are added to metallic gaskets for the introduction of electrical leads into the HP region. Using a composite gasket which includes diamond powders [69] or diamond coating on the flat region of the gasket greatly increases the shear strength (σ) and consequently increases the gasket thickness by 2–3 times (equation (2.1)), thus effectively increasing the sample volume. To eliminate the grain boundary fracture and to avoid interference of x-ray scattering from crystalline gasket materials, high-strength bulk metallic glass has been used as gasket to above 100 GPa [70]. Chemical inertness must also be carefully considered when choosing gaskets for reactive samples.

An important development is the use of the gasket as an x-ray window, allowing x-ray measurements in radial geometry [62, 63] down to x-ray energies ~5 keV. The gasket materials are chosen for mechanical strength, transmission at energies of interest, and low scattering background. High-strength beryllium [63], amorphous boron epoxy inserts [71] with kapton belts [64], and compressed superhard graphite [72] inserts with beryllium belts [73] have been used to reach megabar pressures. Cubic BN [74, 75] mixed with a small amount of epoxy is also widely used as a gasket or insert material for high strength, large thickness, electrical insulation, and x-ray transparency.

2.3. Pressure medium in the sample chamber

After gaskets are machined or indented to match the shape of the diamond culets, a hole is drilled at the center by a mechanical drill, electrical discharging machining, or laser ablation, [76] to form a sample chamber (figure 2). Multiple holes may be drilled [77] for comparative studies or to avoid chemical reactions.

When a solid sample is surrounded by a fluid medium during compression, the sample is subjected to a hydrostatic pressure, where the stress is uniform in all directions. At sufficiently HP, all fluids solidify, with liquid helium solidifying at the highest pressure of 11 GPa at 300 K [78]. Pressure is then transmitted through the solid medium which has a finite strength, leading to non-hydrostatic conditions with pressure anisotropy, inhomogeneity, and gradient. To eliminate or reduce such effects, pressure media are chosen for their low strength and chemical inertness to the sample. A mixture of methanol–ethanol in 4:1 ratio is commonly used as a fluid medium to 10 GPa [79], above which its strength rises sharply. Inert-gas solids are commonly used as pressure media to produce quasihydrostatic conditions up to 8 GPa in argon, 20 GPa in neon, and over 100 GPa in helium [80–82]. Hydrostatic limits of 11 commonly used pressure transmitting media were carefully reviewed by Klotz *et al* [83].

Gas pressure media can be loaded by placing the entire DAC in a large gas pressure vessel, with the cell incompletely closed so that the medium can enter the gasket hole [84]. The gas is pumped into the vessel to a nominal pressure of ~200 MPa and fills the DAC sample chamber as well as its surroundings. A feed-through mechanism is then used to close the DAC sample chamber and seal the sample in the gas medium inside the gasket. The gas-loading method [85, 86] has the advantage of loading gas mixtures without phase separation and low melting temperature gases such as He, H_2, and Ne, without trapping bubbles in the gasket. However, the method uses a significant quantity of HP gas that requires rigorous safety precautions. A simple alternative is to use liquid nitrogen cooling to liquefy gases inside the DAC. This method is used extensively for loading argon as a medium, and has the advantage for loading expensive and rare gases in μl quantities (e.g. isotopically enriched ^{83}Kr [87]).

On the other hand, pressure anisotropy and gradients provide opportunities for studying materials' mechanical properties. When properly quantified, experiments under deviatoric stress can provide rich additional information about strength, plasticity and rheology of the samples that are unavailable with hydrostatic experiments [88]. The uniaxial compression of a DAC is suitable for quantitative studies of deviatoric stress at ultrahigh pressures [89–91].

2.4. Pressure determination

For pressures above several GPa, the primary pressure scales are either based on the pressure-volume (P-V) equation of state (EOS) or the acoustic velocity-density relation. A commonly used primary scale is based on shock-wave measurements of particle velocity (U_P) and wave velocity (U_S) that are used to calculate the P-V relations at isothermal conditions. The shock-wave scale carries uncertainties of about 6–10% [92].

Another primary scale is based on the density (ρ) measured with x-ray diffraction and the acoustic velocity ($V\phi$) measured with ultrasonic or Brillouin scattering methods on the same sample under the same compression conditions. Pressure is then derived directly by

$$P = \int V\phi^2 \mathrm{d}\rho. \tag{2.2}$$

Using this approach [93], ρ can be determined by x-ray diffraction to an accuracy of better than 0.2%, and $V\phi$ can be determined by single-crystal Brillouin spectroscopy, impulsive stimulated light scattering, or phonon inelastic x-ray spectroscopy to an accuracy of 1%.

Once a primary standard is established, any other pressure-dependent variable can be used as a secondary standard for pressure determination. Secondary standards are chosen for their accessibility, sensitivity, and resolution. Using the P-V

EOS of well-studied materials (e.g. MgO, NaCl, Au, Pt, W) as a primary or secondary standard, pressures can be determined by measuring the volumes of these standard materials by HP x-ray diffraction. Another popular and convenient secondary standard is the optical methods, e.g. using the ruby fluorescence shifts. Tiny ruby grains are added in the sample chamber [94], and the pressure-shift of the ruby fluorescence wavelength can be easily probed with a laser beam through diamond windows [82, 92, 95]. The accuracy of the Mao *et al* ruby scale [95] is found to be accurate within 2% up to 55 GPa using the Brillouin scattering and x-ray diffraction techniques [93]. At higher pressures, the quasi-hydrostatic ruby scale [95] appears to underestimate pressures, based on a comparison of recent x-ray diffraction data for metal standards such as Au, Pt, Ta, W, Cu, and Al [82, 96]. More consistent scales have been proposed by the more recent ruby scale of Dewaele *et al* [82] and an internally consistent scale by Fei *et al* [97]. At megabar pressures, Raman shift of diamond anvils may be used to measure pressure [26]. Raman shift of cBN [98] are pursued for having 1% precision in pressure, after considering the propagation of errors from various sources.

2.5. High pressure samples

Handling HP samples can be challenging, not only because of small sizes, but also the inaccessibility and possible changes in crystallinity, mechanical properties, and chemical reactivity. Mastery of HP sample preparation is a prerequisite for successful experiments.

HP samples are always surrounded by other materials (media, gasket, pressure standards, insulating layers, etc). Chemical reactivity needs to be carefully considered in selecting these materials, including possible reactivity changes at HP [99, 100]. Most HP experiments are conducted on polycrystalline samples. Recently, a growing effort has been made on measurements using single crystals [101–103]. To preserve the crystallinity of single-crystal samples, the use of hydrostatic medium is necessary. Sample size may be chosen for optimizing x-ray scattering efficiency. For instance, one absorption length (transmission intensity attenuation to $1/e$) provides optimal scattering efficiency. However, the available HP sample size is constrained by the chamber size in the DAC and the desired pressure range. With the high brilliance of synchrotron x-ray probes, samples as small as a few microns are usually sufficient for obtaining good signals in x-ray measurements. Typical sample configurations are shown in figure 4. A small probing size allows studies of multiple samples in a single chamber [82, 97] or in multiple chambers [77]. With the development of micro-manipulating techniques and submicron x-ray probes, special sample configurations (e.g. sample grid, multilayers) may be used for combinatorial studies.

2.6. Rapid compression and decompression

Pressures in the DAC are often controlled mechanically by tightening screws, and the DAC is usually viewed as a type of static HP device. When screws are rapidly turned, pressures may be changed quickly; for example, synthesizing metastable

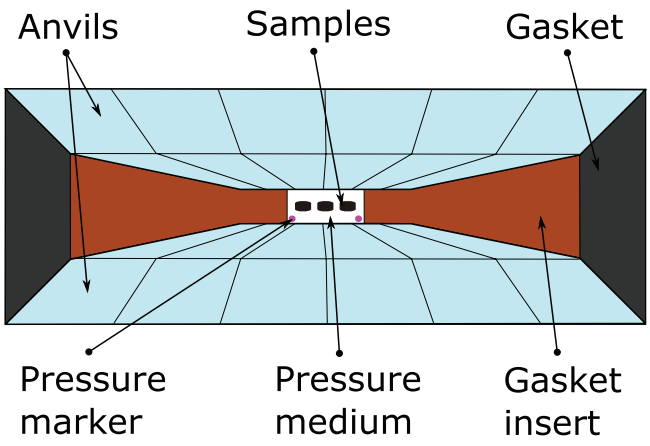

Figure 4. A typical sample configuration in a diamond anvil cell.

phases of Si and Ge when quickly decompressed from HP phases [104, 105]. Recently, the dynamic DAC (dDAC) has been developed for repetitively applying time-dependent load-to-pressure cycles [106–108]. Electromechanical piezoelectric actuators are used to replace screws in dDAC and enable rapid and precise control of a time-dependent application of load or pressure. A compression rate as high as >35 TPa s^{-1} has been reached for a Mo sample in the megabar pressure region (figure 5). In the dDAC, the pressure variation is achieved through the change in sample chamber volume, as the actuators change the load on the cell. Reproducible cycles of the load/pressure can be achieved only within the gasket's elastic limit, which is usually low, but increases with increasing pressure. If the load exceeds the elastic limit of the gasket, the gasket will be plastically deformed and the sample pressure will not recover to its initial state.

The membrane (or diaphragm) technique [109] is widely used for remotely controlling pressure, particularly for low temperature experiments. Recently, the membrane control has been used for rapid compression and decompression coupled with fast x-ray detectors, such as Pilatus [108, 110](figure 5). Phase transformation pathways are strongly influenced by the time dependence of the driving mechanism (compression, thermal transfer, strain, irradiation, etc). This rapid compression and decompression capability allows studies of the nucleation of phase transitions, phase growth, and metastable phases at various compression rates [105, 107, 111, 112]. In particular, this capability covers the region of compression rates between static techniques (DACs and LVPs) and dynamic shock-driven devices (gas guns, explosive, magnetic pulse compression, and laser shock), a region that has been sparsely explored.

2.7. Integration of pressure and temperature

Adding another intensive variable, temperature, greatly expands the bountiful ground of HP studies in the vast *P-T* space. Various temperature-controlling techniques have been integrated with the DAC ranging from sub-*K* to over 7000 K.

2.7.1. Cryogenic temperatures. DAC can be inserted in a cryostat and cooled down to below 4 K. There are various

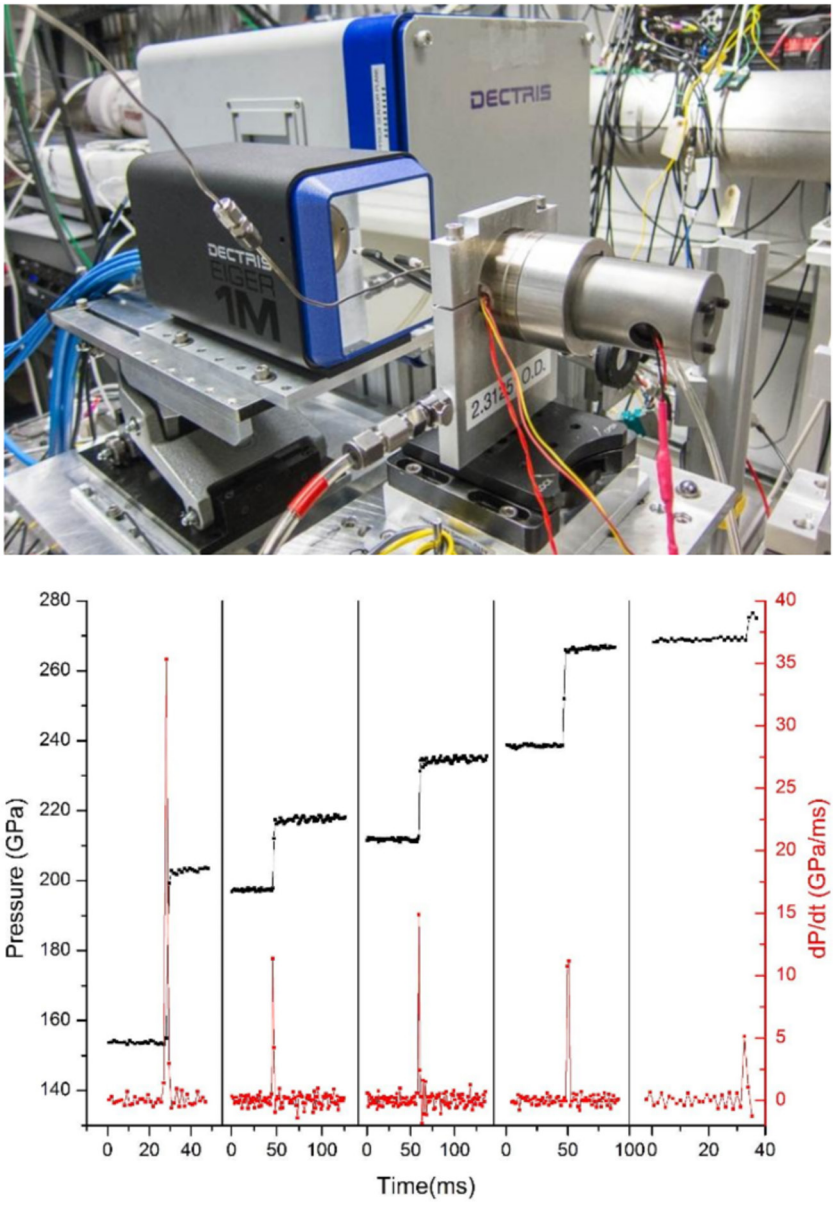

Figure 5. (top) A setup for rapid compression and decompression experiments at the HPCAT 16-ID-B beamline. (bottom) A compression rate of >35 TPa s^{-1} has been reached on a Mo sample between 150 and 280 GPa.

types of cryostat for accommodating different temperature ranges, types of DACs, and probe requirements [108, 113, 114] (figure 6). Gas (N_2, He) flow cryostat can be routinely operated at ~5 K, and can reach temperatures below 2 K [115]. It is versatile and can accommodate practically any type of DAC; including large DAC such as the long piston-cylinder DACs with lever arm control. Compact cold-finger cryostats provide much more flexibility and large access openings, but with a limited low temperature down to 7–8 K. Compact size and large openings allow rotation of the cryostats during exposure for single crystal diffraction and inelastic x-ray scattering. Cryostats designed for DAC can have multiple windows (kapton, mylar, or other materials of choice) to accommodate optical and x-ray diffraction and inelastic scattering measurements in forward, lateral, or backward scattering geometry.

Pressure in cryostats/DACs can be controlled remotely at low temperature by either helium compressed diaphragm (membrane) control, or mechanical means (gearbox, lever arm assembly). The pressure at cryogenic temperatures can be measured with online ruby/Raman systems [108, 116], or using x-ray diffraction standards such as Au, NaCl, or MgO. Temperature of the sample in a cryostat is typically controlled by adjusting the flow rate of cryogen into the cryostat and a heating wire attached to a proportional-integral-derivative (PID) control loop. Multiple stages may be added to a cryostat to achieve temperature lower than liquid helium. For example, temperatures down to 2 mK [35] can be reached by employing a dilution refrigerator or dry dilution refrigerator.

Specific cryostats are designed to meet the constraints of experimental conditions. Some typical requirements for HP studies include (1) precise motion controls including rotation around the vertical axis, (2) large openings (>60°) for single crystal x-ray diffraction and inelastic x-ray scattering, (3) versatile geometry for accommodating a variety of DACs, (4)

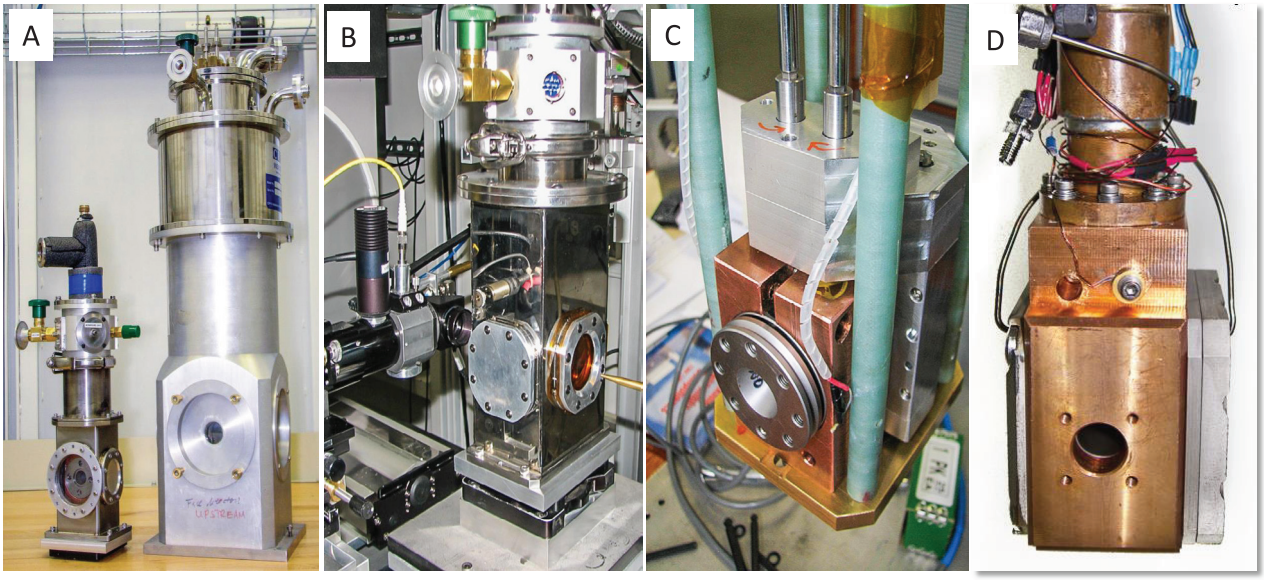

Figure 6. Photographs of various types of cryostats used for high pressure x-ray studies at HPCAT. (A) Compact cold-finger cryostat for diffraction and spectroscopy measurements and large flow cryostat for diffraction. (B) A compact combination cryostat for diffraction and absorption measurement at HPCAT 16-BM-D beamline, with an online ruby system and MAR345 area detector on the background. (C) Symmetric DAC coupled with a mechanical pressure control device (gearbox) in large flow cryostat. (D) Double-diaphragm pressure control frame, allowing precise pressure control at different temperatures, for compact cryostat. (Courtesy of Stanislav Sinogeikin.)

remote pressure controls using either pneumatic or mechanical methods, and (5) the position stability of the DAC while its temperature changes.

2.7.2. External resistive heating. HP samples can be heated by conduction with the heat source outside the sample chamber. There are two major varieties of the resistive heating methods—heating elements that are either external or internal to the sample chamber. External furnaces provide precise and well-controlled temperature conditions. The entire DAC may be heated by a resistively heated furnace up to 700 K. For higher temperatures, a small heater very close to diamond anvils may be used for temperatures up to 1200 K [117, 118]. With a graphite heater around diamond culets, temperatures as high as 1700 K have been reported [119]. However, there is an intrinsic temperature limit, due to the rapid graphitization of diamond above 1900 K, even in an inert environment or vacuum [120]. In addition, due to the softening of the stress-bearing components, including the gasket, the seats for anvils, and the diamond anvil itself, maximum attainable pressure is then limited.

Similar to the cryogenic cooling technique, one advantage of the external heating technique is the independent control of temperature, i.e. temperature controls are not affected by the changes of samples (phase transitions, property changes, etc) or pressure conditions. Specific *P-T* paths may be performed with *in situ* x-ray measurements, such as isothermal compression [97] or isobaric path [121].

Temperatures are measured by placing thermocouples close to the sample position, often attaching them to one or both diamond anvils. Notably, the temperature readings may vary as the thermocouple locations are changed, leading to a sizable offset between the thermocouple readings and the true temperature at the sample location. This offset in temperature is often overlooked in literature and can be monitored and corrected by using the infrared spectral radiometric thermometry. For example, temperatures down to 530 K can be measured by collecting thermal radiation in the 1–2 μm wavelength range [122].

2.7.3. Internal resistive heating. On the other hand, the internally heated method locally heats the sample *inside* the sample chamber. Placing heating components in the 100 μm size DAC sample chambers has proven extremely challenging. Often, the sample itself is used as a conductive heating element and heating is applied electrically [123, 124]. Alternatively, a metallic wire placed inside the gasket can be used as an internal heater for heating samples nearby; for example, MgO and Pt has been placed in a tiny hole in a Re wire for x-ray diffraction studies up to 1900 K at 80 GPa [125]. Temperatures are measured by thermal radiation, and may be reached close to the melting temperatures of the conductors. A successful loading may result in stable heating in an area of $>$20 μm in dimension, sufficiently large for many x-ray measurements. More sophisticated internal heating techniques may require building a resistively heated wire circuit in the diamond anvil culet, using the chemical vapor deposition method [126, 127].

2.7.4. Laser heating. The transparency of diamond allows applications of near- and mid-infrared lasers (CO_2, Nd:YAG, Nd:YLF) to heat samples between two diamond anvils at HP. DAC samples can achieve temperatures in excess of 7000 K. This method has led to major discoveries of new high *P-T* phases [128–131]. The infrared laser passes through the transparent diamond and only heats the IR-absorbing samples, without heating the gasket and other DAC components, thus avoiding interference with the DAC operation and sample probing. Largely due to the steep temperature gradients

outside the heating spot, inconsistent results were reported initially by different laboratories, causing confusion about the efficacy of the laser heating technique. Now, significant progress in shaping and defining the temperature distribution in the laser heated DAC has been made. The double sided heating technique [132, 133] exploits optimal laser characteristics, sample configuration, and optical arrangement.

The newer fiber lasers, widely used in most laser-heated DAC applications, have greater design flexibility than traditional YAG or CO_2 lasers and prove considerably more energy efficient. The high energy efficiency has resulted in high thermal stability, thus delivering laser beams with high stabilities in power, power distribution, and pointing angles. Furthermore, fiber laser is available with hundreds of Watts power and better collimation than the rigid YAG or YLF laser. A high power fiber laser (>200 W) allows defocusing the laser beam and achieving large (>100 μm in diameter) heating areas on the sample [134]. With developments in x-ray beam controls, an x-ray beam size of 3–5 μm FWHM is common at several beamlines, with the tail at full width of 1% maximum less than 30 μm. A larger heating area relative to the x-ray beam size means less temperature gradient and more accurate x-ray measurements at extremely high *P-T* conditions.

In designing the laser delivering optical system, a number of factors should be optimized simultaneously, such as (1) compactness, (2) stability, (3) focus size control, (4) power uniformity at the focal area (to minimize the radial temperature gradient), and (5) double sided heating (to minimize the axial temperature gradient). Different modes of lasers [135] or beam profilers [136] have been used to achieve flap-top profiles in laser power distribution. However, due to possible inhomogeneities in HP samples, even a flat-top laser may not provide uniform heating of the sample. Using high power lasers, which allow defocusing to a large degree, is an effective way to reduce radial temperature gradient. Together with double sided heating, a uniformly heated volume can be generated at HP in DAC. With x-rays measuring bulk properties, a uniformly heated volume much larger than the probing x-ray beam size is a prerequisite for all successful quantitative x-ray measurements, as illustrated in figure 7.

Because diamond has the highest known thermal conductivity, any heating by the laser would be conducted away by the anvil when a sample is in direct contact to the diamond anvils, resulting in the inefficient heating of the sample. Compensating the heat lost by greatly increasing the laser power will risk damaging the diamond anvils. Therefore, the design of the sample configuration and careful preparation of the cell are keys for efficient heating and minimizing temperature gradients. Employing insulating layers (e.g. Ne, Ar, MgO, Al_2O_3, NaCl, KCl, etc) with sufficient thickness and thermal resistance between the sample and anvil is crucial in the design of sample configurations and for achieving successful heating.

The accuracy and precision of temperature measurements in the laser-heated DAC have improved significantly with the use of spectral radiometry. The thermal radiation spectrum is fitted to the Planck radiation function to determine the temperature [123, 137]:

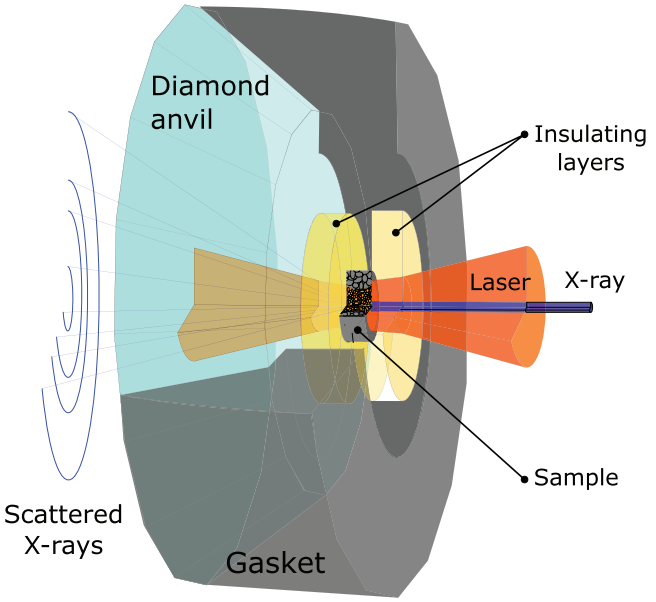

Figure 7. Double-sided laser heating generates a uniformly heated volume, larger than the probing x-ray beam size. Insulating layers are essential for efficient heating and minimizing temperature gradients.

$$I_\lambda = c_1 \varepsilon_\lambda \lambda^{-5} e^{-(1-c_2/\lambda T)} \tag{2.3}$$

where I is spectral intensity, λ wavelength, ε emissivity, and two constants $c_1 = 2\pi hc^2 = 3.7418 \times 10^{-16}$ Wm^2 and $c_2 = hc/k = 0.014\,388$ mK, where h is Planck constant, c speed of light, and k Boltzmann constant. Temperature measurements are limited to above 1000 K, due to the insensitivity of the CCD detector in the long wavelength (IR) region which is essential for characterizing temperatures below 1000 K. The problem could be resolved by using an IR sensitive InGaAs detectors and IR optics to extend the temperature measurement down to 500 K [122]. The region between 300 and 500 K can be easily reached by external heating tapes, hot plates and many other simple methods, and can be considered as small perturbation of ambient temperature.

The laser heated DAC experiments have become a routine capability in HP studies with x-rays. Many synchrotron facilities are equipped with double sided laser heating systems [132, 134–136, 138–141]. Portable laser heating systems have recently been developed [122, 142, 143], expanding the use of the laser heating techniques into specialized beamlines without permanent laser heating systems.

2.7.5. Modulated laser heating. An important advantage of the laser heating technique is its localized heating in space. With modulated heating, localization can be also achieved in time [134, 144–148]. Fast-modulated laser heating in a DAC can suppress thermally activated diffusion, suppress possible chemical reactions of the sample and environment, and reach even higher temperatures. The timing structure of synchrotron radiation is suitable for developing time-resolved x-ray measurements of samples following pre-designed heating paths. A laser pulse can be synchronized with synchrotron pulses, together with gated x-ray detector (e.g. Pilatus) and

time-resolved radiometric temperature measurements [148, 149]. The modulated laser heating holds great potential for the applications of the laser heated DAC, such as the accurate measurement of melting curves, phase transition relations, thermal diffusivity, and *P-V-T* EOS.

3. *In situ* HP-SR x-ray techniques

In the past decade, we have witnessed a significant surge of HP studies using synchrotron radiation. Many previous technical limitations in capability, precision, and accuracy have been removed through the optimization of source radiation, insertion device, x-ray optics, sample environment, experimental configuration, motion control, automation software, advanced detectors and analyzers, and computing power. Among the wide array of HP x-ray techniques, structure determination using x-ray diffraction (XRD) remains the dominant one, while significant progress has been made in integrating other x-ray techniques for HP research, such as x-ray radiography and tomography [77, 150, 151], x-ray spectroscopy (absorption, emission) [10, 152], inelastic x-ray scattering (IXS) [11], and nuclear resonant scattering [153–155]. New HP synchrotron techniques are emerging rapidly; for example, in HP nano-imaging techniques (full field, position-scanning, and coherent diffraction imaging) [18, 151] and time resolved HP x-ray techniques [13, 148, 156].

3.1. General features in HP x-ray probes

3.1.1. Incident x-ray beam. The high energy x-rays penetrating the pressure vessel are partially absorbed by the vessel materials as shown in figure 8. The high brightness and high collimation of SR allows small focused beams to impinge on the sample. It took nearly three decades to reduce the x-ray beam size from 30–50 μm to the current 2–3 μm in HP-SR research. This substantial reduction is responsible for many recent breakthroughs in HP science using SR. Beam sizes of a few tens of nanometers have been reached at specialized beamlines. Integrating HP with sub-μm beams enables the study of more complex and smaller samples at increasingly higher pressures and more extreme temperatures.

The x-ray beam size is commonly characterized by the full width at half maximum (FWHM) of peak intensity. Assuming a Gaussian distribution, the FWHM accounts for about 75% of the total flux. The beam size at full width at tenth maximum (FWTM) may be 2–3 times larger. The x-ray beam outside the FWHM area is often regarded as 'tail'. Although the tail accounts for only ~25% of the total flux, it may extend to surrounding materials with a much greater thickness, volume, or x-ray scattering power than the sample, contributing an overwhelming amount of unwanted background signal. Therefore, properly screening the beam tail is important in any HP-SR experiment, particularly for samples with relatively low scattering power such as amorphous materials or low-*Z* materials. Usually clean-up slits or pinholes, located as close to the sample position as possible, are installed [157, 158] to cut down the tail.

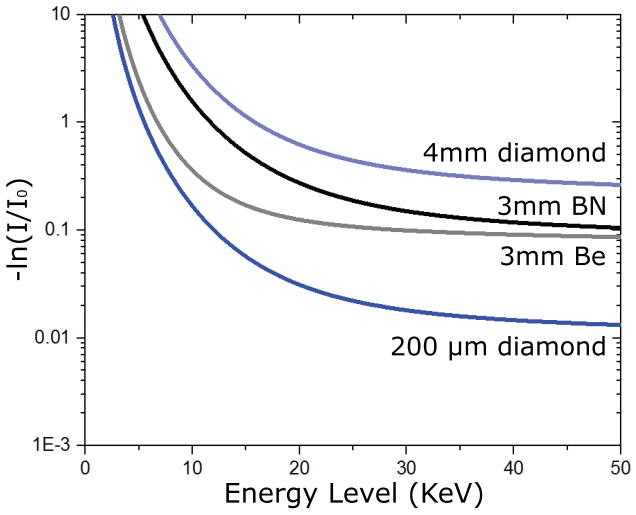

Figure 8. X-ray absorption length of commonly used materials in diamond anvil cells as a function of x-ray energy. The absorption length (μt) is defined as $\mu t = -\ln(I/I_0)$, where μ is the absorption coefficient; t the thickness of the material along the x-ray path; I and I_0 are intensities of the incident and transmitted x-rays, respectively.

3.1.2. Separating sample signals from background. While maximizing signal-to-background ratio is important in all types of experiments, it is particularly critical in HP studies, because the volume ratio between samples which yield valuable signals and the surrounding materials which yield undesired background can be as little as 10^{-5}–10^{-9} (figure 2).

Proper collimation on the detection side is thus essential to reduce the background from surrounding materials along the incident beam path, before and after the sample. When HP devices were first integrated with SR, the energy dispersive x-ray diffraction technique (EDXRD) with a point detector was widely used. In EDXRD, a tight collimation (a lozenge shape collimation together with the small incident beam) can be established for selecting scattering signals from sample areas. Even today, EDXRD is still an effective technique for studying weakly scattering samples, such as amorphous and low-*Z* materials [159, 160]. Alternatively, a soller slit may be employed for background discrimination when the angular dispersive x-ray diffraction technique (ADXRD) with a 2D area detector is used [161]. In IXS measurements, however, the collimation requirement is in conflict with the need of large solid angles for collecting weakly scattered signals. Recently, this problem has been reduced by using an x-ray focusing optic (e.g. x-ray polycapillary). As shown in figure 9, a focusing optic can be used for the collection of scattered x-ray with a sizable solid angle similar to an objective lens in the optical microscopy [162]. The focus provides desired depth resolution, significantly discriminating background signals originating from materials surrounding the sample.

Separating sample signals from background can also be achieved by using temporal discrimination methods. In nuclear resonant x-ray scattering, incident x-rays of meV resolution is tuned near the exceedingly narrow nuclear resonant line (at neV level). The delayed signals caused by the narrow nuclear absorption are slower than other prompt scatterings from electrons. By using time discrimination electronics, nuclear

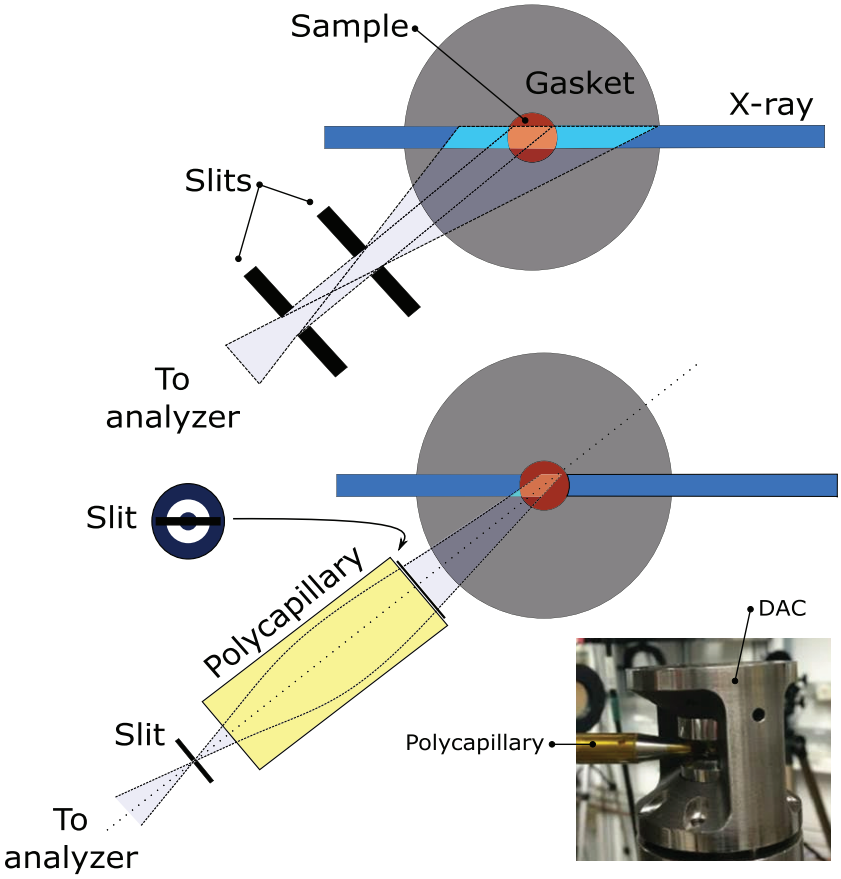

Figure 9. Illustrations of a slit system and a polycapillary optic, used to suppress signals from surrounding gasket materials in inelastic x-ray scattering measurements. A shaped slit in front of the polycapilary defines the momentum transfer. The inset is a photograph of a polycapillary optic placed close to the sample in a diamond anvil cell. (Courtesy of Paul Chow.)

resonant signals can be highly selective to specific elements and well separated from other background signals [154].

3.2. HP x-ray diffraction

X-ray diffraction (XRD), which provides structural information of high precision and accuracy, has long been the dominant application of SR for HP research and is likely to remain so in the future. In general, the structural information is averaged over the sampling volume. The basic information from XRD includes unit cell parameters, atomic positions, thermal parameters, and even electron density distributions. With special XRD geometry and sample configuration, we may get information of strain, preferred orientation, site occupancy, and order–disorder. In addition, by tuning x-ray energies close to absorption edges of certain elements, anomalous XRD provides element-specific structural information.

Samples in various forms (single-crystal, polycrystalline, nano-crystals, amorphous/liquid) have been studied using HP XRD for structure and/or pair distribution functions [163, 164], phase transitions (including melting), *P-V-T* EOS, elasticity, and lattice strains [92, 165]. Several HP XRD techniques have been developed accordingly, including single-crystal XRD, polycrystalline (powder) XRD, and amorphous XRD. Recently, the multigrain crystallography method which identifies multiple single crystals in a polycrystalline sample, has been proposed [166] and applied successfully to HP studies (e.g. [167, 168]).

3.2.1. HP angular dispersive XRD. Angular dispersive XRD (ADXRD), using monochromatic radiation and two-dimensional (2D) detectors, has been the primary technique in HP XRD. In HP experiments, samples may be subjected to some degrees of stress, causing diffraction lines broadening by non-hydrostatic conditions. Resolution in ADXRD is typically at $\Delta d/d \sim 3 \times 10^{-3}$ (e.g. [157]) which is in general adequate for studying simple structured materials at HP conditions. With the developments in the HP technology, hydrostatic or quasi-hydrostatic conditions can be routinely achieved. The improved sample environment permits the studying of low symmetry materials and detecting subtle changes in volume or structure distortion in HP transitions, such as pressure-induced Fermi-surface nesting [169], electronic topological (Lifshitz) transitions [170], morphotropic transitions [171], and 3*d* electron magnetic collapse [172–174].

The resolution in *d*-spacing can be improved by reducing incident beam divergence, lowering x-ray energy, and improving angular resolution in detecting systems; for example, by increasing sample-detector distance, reducing slit size or effective pixel size, or using an analyzer such as a silicon crystal [175]. High resolution is achieved at the cost of throughput. It is practical to have several switchable modes in HP

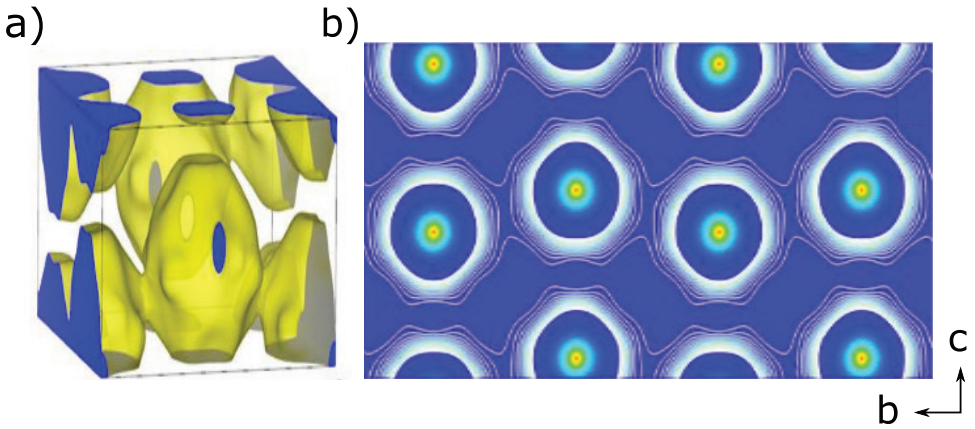

Figure 10. Electron density distribution in β-Ge (a phase irrecoverable in ambient conditions), determined *in situ* at 12 GPa using the high pressure single-crystal technique: (a) 3D electron density map. (b) A contour map along [101] direction. The electron density topology is consistent with a model of covalent bonding in the *ab* plane and metallic bonding along the *c* axis.

ADXRD, with high-throughput, low-resolution mode coupled by 'zoom-in' mode producing high-resolution XRD results. In HP ADXRD with DAC, an x-ray energy ranging from 10 keV to 100 keV is selected based on factors such as the coverage in reciprocal space, accessible angular openings of the HP device, penetrating power, and detector efficiency.

3.2.2. HP energy dispersive XRD. Using a polychromatic x-ray beam and an energy dispersive point detector at a fixed 2θ angle, EDXRD is mainly used for studying liquid and amorphous materials. In EDXRD, one takes the advantages of low background due to well-defined collimation in the beam path to the detector, and large coverage in reciprocal space. In general, EDXRD provides limited sampling of reciprocal spaces of crystallites in the sample because of the fixed 2θ angle, and is not suitable for probing samples near melting or with rapid crystal growth. Consequently, EDXRD may not provide reliable intensity measurements, making it difficult to obtain crystal structure information such as bonding characteristics and atomic positions. A technique has been developed for large volume presses by employing both ADXRD and EDXRD concepts [176]. By scanning an energy-calibrated multichannel solid state detector, a large number of EDXRD patterns are obtained at pre-determined angular step-size. The entire dataset can be re-arranged as ADXRD patterns by plotting intensities of each channel (corresponding to a given photon energy or wavelength). Subsets of the data covering narrow energy bands may be binned to give ADXRD patterns at a single wavelength with improved counting statistics; these may be combined with a multi-pattern Rietveld analysis to efficiently utilize the entire data set. While high photon-energy data provide coverage at the low *d*-spacing range, low photon-energy data cover the high *d*-spacing range. This scanning angle technique has been applied to DAC [177]. The multi-energy ADXRD data carry much more information than regular single-energy ADXRD, which could provide site-specific and element specific structural information for full structure refinement.

3.2.3. HP polycrystalline (powder) XRD. With an incident x-ray beam passing through the surrounding material and impinging upon a polycrystalline sample, the XRD rings are recorded on the detector. Polycrystalline XRD has been well established for studying HP crystallography, phase identification, *P-V-T* EOS, melting, pressure-induced amorphization, texture, preferred orientation, line broadening analysis of particle size and strain effects, residual stress, etc. In polycrystalline XRD, good particle statistics are crucial for the sufficient quality of HP XRD. Another critical factor determining the quality of diffraction data is the resolution ($\Delta d/d$) because the polycrystalline XRD measures diffraction rings from all of the lattice planes simultaneously.

Intensity information is often used for structure refinement via the Rietveld method [178]. However, background subtraction by removing intensity contributions from the surrounding materials (anvils, gaskets) is not trivial and precautions need to be taken when using Rietveld refinement and interpreting the results from those analyses. Background subtraction methods [179–182] developed for measuring pair distribution functions (PDF) of amorphous/liquid materials at HP may be applied to Rietveld refinement of polycrystalline samples. Although the Rietveld method is a very powerful tool for structure refinement, it does not provide the initial model to be refined. Traditional methods of structure analysis, such as Patterson synthesis or direct methods, are often used to establish the basic features of the structure, after which the Rietveld refinement can be carried out. Recently, many successful structure predictions have been made by first principle calculations [183, 184]. These predictions can be used as initial input models in structure refinement too.

3.2.4. HP single-crystal XRD. In comparison to HP polycrystalline XRD techniques at synchrotron HP beamlines, HP single-crystal XRD is relatively under-utilized. Recently, rapid developments in HP single-crystal XRD have been made [102, 103, 185, 186]. In single-crystal XRD, the orientations and intensities of diffracted beams are measured. The high flux and small beam at synchrotron HP beamlines allow for efficient studies of 1–10 μm crystal size. Detailed crystallographic information, such as structure model (atomic position, occupancy, thermal displacement parameter) and electron density distribution can be obtained (figure 10). From single-crystal data, space groups and Miller indices can be unambiguously

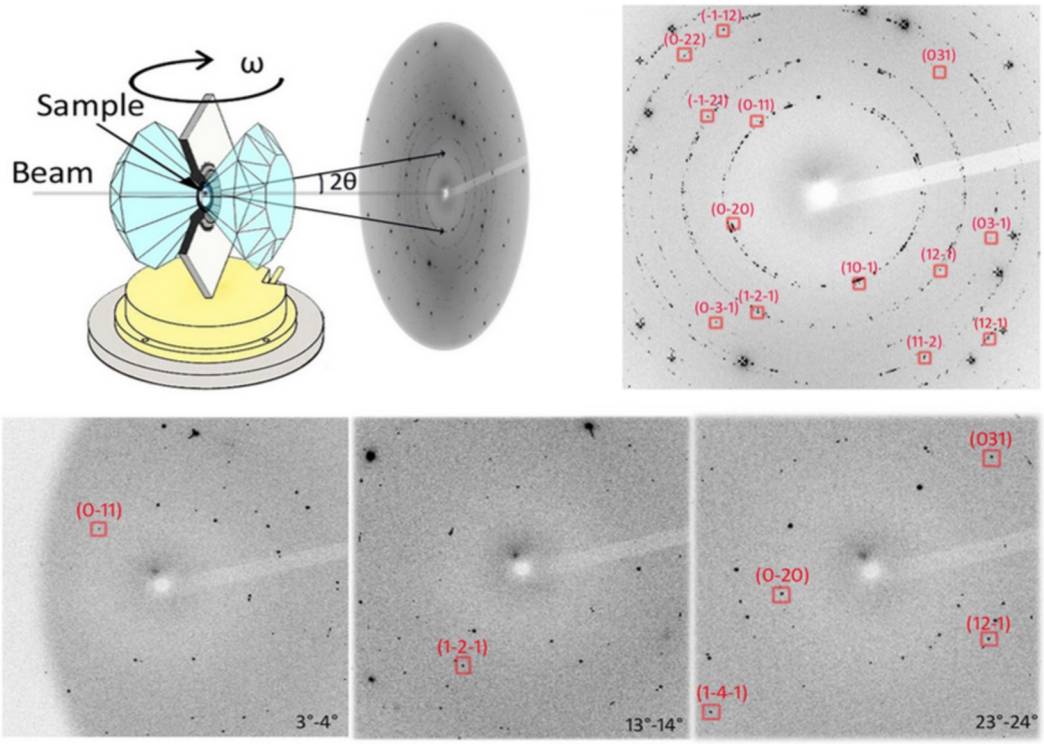

Figure 11. Spotty diffraction patterns (common in high pressure experiments) are used to obtain single-crystal diffraction data for structure refinement. These diffraction patterns were collected from a β-Ge sample at 12 GPa, after heat treatment at 300 °C for 8 h. More than 15 good quality crystallites are identified.

determined. Because the diffraction is measured at different orientations, the single-crystal XRD technique also has advantages in dealing with materials of low crystallographic symmetries. Single-crystal XRD was first applied to HP using the EDXRD technique [80, 187]. Recently, synchrotron monochromatic beams have been widely used in HP single-crystal XRD by rotating samples coupled with either a point detector [188] or an area detector [102, 167, 189]. Many HP beamlines in the world have established routine procedures for conducting HP single-crystal XRD experiments.

When there are constraints in rotating the sample, HP single-crystal XRD experiments may be conducted by scanning monochromatic energies with an area detector [190] or by using polychromatic beam (the Laue approach). The HP Laue approach does not require rotation of the sample and could provide information on deformation, mosaicity, and strains [191, 192], thus enabling fast measurements at sub-second time scale.

3.2.5. HP multiple grain XRD. Polycrystalline structural refinement for ultrahigh-pressure samples becomes increasingly challenging and the results could be uncertain. Single-crystal structural refinement is necessary [193] but successful examples of growth and preservation of several μm-size single crystals above 100 GPa are extremely rare [80, 194]. With the developments of micro-beam technology using SR, the minimal size needed for single-crystal diffraction has been reduced to sub-μm. Traditional powder samples may be treated as multiple grains. Grain growth can be further promoted by laser heating and other heating means integrated with DAC, often resulting in 'spotty' patterns in diffraction images (figure 11). A new tool of '*multigrain crystallography*' has been recently developed with the quality of the resulting refinements comparable to single-crystal work [166]. In the multigrain approach, the same data collection procedures as those in the single-crystal XRD are used. Diffraction signals up to hundreds of single crystals are simultaneously collected. The multigrain approach is an effective way to increase redundancy and completeness in data collection, thus significantly improving the HP single-crystal data quality. HP multigrain XRD possesses great potential for the crystallographic studies of materials under HP, as demonstrated recently in studies of crystal structural determination of (Mg,Fe)SiO_3 bridgmanite [195], post-bridgmanite [167], SiO_2 [168], and β-Ge [103].

3.2.6. HP amorphous XRD. XRD has been widely used to determine structure factors of liquid/amorphous materials at HP [179, 196, 197]. Interesting phenomena have been observed, including coordination number change [60, 61], polyamorphism [198, 199], and long-range topological order [200]. In DAC experiments, the amorphous XRD method is often utilized with a high energy monochromatic beam, in order to have a large coverage in momentum transfer $Q = 4\pi\sin\theta/\lambda$ [61, 180, 181] for sufficient real space resolution. Although the experimentally measured $S(Q)$ is sensitive to changes of structure, it can be complicated to interpret. The pair distribution function $g(r)$ provides a far more intuitive characterization of local structure, as it gives the probability of finding one atom at a given distance from another. The resolution of this real-space structure is inversely proportional

to the highest Q. The high real-space resolution is required to accurately determine the bond lengths and angles that comprise the local structure.

The EDXRD method with polychromatic radiation has also been used for amorphous XRD studies [197, 201]. EDXRD data are collected at multiple 2θ angles to increase coverage in the reciprocal space for the accurate determination of the radial distribution function (e.g. [197]). The synchrotron incident beam spectrum is simulated using a Monte Carlo approach and Compton scattering effects are based on theoretical predictions [202]. The advantage of this method is the excellent collimation, through which background scattering from surrounding materials can be largely eliminated [203, 204]. This is a particularly useful technique for liquids with low scattering power (e.g. oxides and silicates). With the use of a soller slit system, diffraction from surrounding materials can be effectively minimized and ADXRD has been successfully applied to the study of liquid structures, utilizing the Paris–Edinburgh (PE) presses [161].

One challenging aspect in HP amorphous XRD is the weak scattering from non-crystalline materials. This has been partly overcome with the high brightness of the third generation synchrotron sources. In addition, efforts have been made to properly subtract background signals [179, 182], and to reduce unwanted scattering by using partially perforated anvils [180, 181].

When studying non-crystalline structures, it is critical to pursue information on the individual partial-correlation functions of the material of interest. By tuning incident x-ray energy, anomalous scattering can be used to amplify or suppress scattering from specific atomic species. Partial information may also be obtained by combining neutron scattering data, where scattering intensity is often different from the monotonic Z-dependence of x-ray cross-sections [205].

3.2.7. HP radial XRD. When a sample is subjected to uniaxial compression in a DAC, radial XRD (R-XRD) technique may be applied with the primary x-ray beam in the radial direction, perpendicular to the DAC loading axis. R-XRD allows measurements of how the d-spacings vary with ϕ, the angle between scattering direction and the compression axis. The difference in d-spacings obtained from the $\phi = 0°$ and $\phi = 90°$ gives the deviatoric strain; $\varepsilon = (d_{0°} - d_{90°})/3d_{\mathrm{P}}$, where $d_{\mathrm{P}} = (d_{0°} + 2d_{90°})/3$ is the d-spacing under the mean pressure σ_{P} and $\sigma_{\mathrm{P}} = (\sigma_3 + 2\sigma_1)/3$ where σ_3 and σ_1 are axial and radial stresses, respectively. This data can be used to determine the deviatoric stress $t = \sigma_1 - \sigma_3$. HP R-XRD provides useful information on sample stress, strain, deformation, and slip mechanism [206–209]. The dependence of d-spacings as a function of the angle provides information on strains under deviatoric stress conditions. The relative intensity at different angles reveals the preferred orientation of a polycrystalline sample. The inverse pole figure from such data can be used to determine sample deformation and slip mechanism (e.g. [90]).

In specially designed multianvil devices such as the deformation DIA [210, 211] or rotational Drickamer apparatus [212], R-XRD is used to measure stresses in a sample under a controlled differential stress field during deformation. Strains can be measured using radiography, consequently permitting measurements of the stress–strain curves of bulk samples at HP [213, 214].

3.3. HP x-ray spectroscopy

X-ray spectroscopy (XRS) can be used as a probe of electronic structure, such as band structures and bonding. In the last decade, significant developments in HP XRS have been made, thanks to the advent of the third generation synchrotron radiation. Many new HP XRS capabilities have been enabled and established at HP beamlines in the world. With emerging new synchrotron sources and upgrades of many existing third generation sources, together with developments in HP devices designed for HP XRS, we are entering a highly productive period for HP research using XRS. We discuss the following methods for HP studies: x-ray absorption near edge spectroscopy (XANES); extended x-ray absorption fine structure (EXAFS); x-ray magnetic circular dichroism (XMCD); and (resonant) x-ray emission spectroscopy (R-XES).

3.3.1. HP x-ray absorption near-edge spectroscopy. In x-ray absorption spectroscopy, incident x-rays are absorbed when their energy exceeds the excitation energy of deep-core electrons of a specific element, causing a sharp edge-like absorption spectrum. XANES measures the energy dependence of the x-ray absorption coefficient to tens of eV above and below the edges for core-level electrons of an element of interest. It provides information on the symmetry-projected conduction band density of states that is related to the electronic properties, including oxidation state, crystal-field splitting, hybridization, charge transfer, and electronic ordering. HP XANES instrumentation is among the simplest in HP experiments. Only the monochromator needs to be scanned across the specific energy edge of the element of interest. The monochromatic x-rays are focused by mirrors upon the sample in DAC. The absorption is measured by monitoring the intensity change of either the transmission or the fluorescence signals, due to the absorption/reemission process, and is normalized relative to a reference intensity measured before the sample.

XANES was one of the first XRS techniques applied at HP [215], but was previously limited to a narrow range of energies due to the absorption and diffraction glitches by diamond anvils. To greatly reduce the diamond in the beam path, counter bores (perforation) can be drilled in diamond anvils, as used in Bassett-type hydrothermal DAC for studying ions in aqueous solutions at moderate P-T conditions [53]. High quality XANES data (e.g. [216]) have been collected for transition metals in DAC experiments with energies down to 5 keV. When studying absorption edges over 30 keV, using nanocrystalline diamond as an anvil material can avoid glitches resulting from the diffraction of the single-crystal diamond anvils [217, 218]. An alternative beam path through high-strength beryllium and boron gaskets are used in DAC [72, 219, 220].

An energy dispersive XANES technique has been developed [221], where a focused polychromatic beam (~5 μm) of extremely high flux passes through the sample, and is collected by an energy dispersive detector, capable of fast capturing the

XANES signals at micro-second level [142, 222]. The fast measurement and small beam size in this technique allows mapping of XANES images by scanning the sample position [223].

3.3.2. HP extended x-ray absorption fine structure. EXAFS measures the energy dependence of x-ray absorption coefficient to typically 500–1000 eV above the edges. EXAFS arises from scattering of electrons in the environment of an atom, from which local structural information (interatomic distances and coordination) is obtained. Thus it provides element-specific local structural information that is particularly valuable for amorphous materials or clusters in low concentrations, where the XRD method is inapplicable.

Similar to HP XANES, perforated diamond anvils [152] or x-ray transparent gaskets [219] have been used to extend EXAFS measurements down to 5 keV. Diffraction caused by single-crystal diamonds is detrimental to the EXAFS spectroscopy and is now effectively avoided by using nanocrystalline diamond as an anvil material [217]. The use of nano crystalline diamond is particularly beneficial in EXAFS studies over 30 keV. EXAFS has been used for studying the pressure effects on the structures of liquids [224] and amorphous solids [218, 225]. Mobilio and Meneghini [226] provide a review of the variety of synchrotron-based x-ray techniques for studying amorphous materials, including techniques like anomalous scattering that can be used in conjunction with EXAFS.

3.3.3. HP x-ray magnetic circular dichroism. XMCD measures the difference of two x-ray absorption spectra (XAS) taken in a magnetic field, by the use of circularly polarized x-rays [59]. By taking one with left circularly polarized light and another with right circularly polarized light, the difference in the XMCD spectrum provides information on the magnetic properties of the atom, such as its spin and orbital magnetic moment. XMCD is therefore similar to conventional optical MCD with visible light (magneto-optical Kerr effect) [227]. For HP applications, XMCD allows the use of high energy x-rays to penetrate the surrounding materials; it can be observed in both XANES and EXAFS. XMCD in XANES can measure spin-resolved conduction band densities of states, whereas XMCD in EXAFS provides local magnetic structural information. The sign of the dichroism gives the ferromagnetic coupling between atoms in materials [59, 228].

HP XMCD has been well developed for studying HP effects on ferro(ferri)-magnetic materials, yielding element and orbital-selective magnetization [16, 59, 229–231]. In particular, XMCD is advantageous in cases where more than one magnetic element is present. The selectivity is beneficial for elucidating the role of selected electronic orbitals in mediating magnetic interactions. Neutron scattering techniques, on the other hand, probe the magnetic moment of all scattering atoms simultaneously. Similarly, SQUID magnetometry lacks element-specificity and is limited to lower pressures, due to restrictions in sample environment [232, 233].

3.3.4. HP x-ray emission spectroscopy. In XES experiments, deep-core electrons in the sample are excited by x-rays. The subsequent fluorescence radiation provides information on the filled electronic states of the sample, such as the core-level binding energies and the valence band density of states. It provides a unique probe for the diagnosis of pressure-induced magnetic spin collapse in transition elements [234, 235], and a general probe for valence band [103, 236]. The information provided by XES is complementary to that provided by XAS on unoccupied states. Moreover, the final state of the fluorescent process is a one-hole state, similar to the final state of a photoemission process.

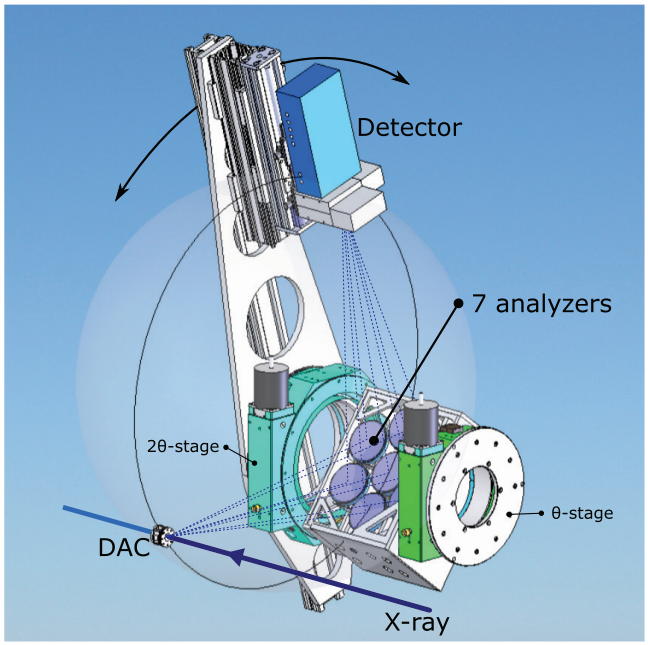

Figure 12. A Rowland circle spectrometer with synchronized $\theta - 2\theta$ scans of the analyzers and detector. A new design of a 7-element analyzer system is shown, with a conical collection angle matching the opening of the diamond anvil cell. (Courtesy of Eric Rod.)

HP XES data are typically obtained by a Rowland circle spectrometer with synchronized $\theta - 2\theta$ scan of the analyzer and detector (figure 12). The excitation x-ray source only needs to have higher energy than that of the fluorescent photons. Therefore, white, pink, or monochromatic x-rays can be used as the excitation source. The energies of the fluorescent photons are analyzed with a sub-eV energy resolution of the emission spectral line shape. Similar to HP XAS, the development of x-ray transparent gaskets has extended the low end of the energy window down to 5 keV. HP XES measurements for all elements above Ti can now be performed by using proper analyzer crystals [237]. Multiple analyzers can be used to increase solid angle coverage in data collection and thus the signal level [238]. Recently, a short-distance spectrometer of large solid angle coverage has been developed, with which data collection time in HP XES is reduced from hours to only several minutes [239]. The XES technique has been extended to high *P-T* conditions with laser heated DAC techniques [138, 240]. Examples of HP XES include the study of predicted high-spin/low-spin transitions in iron oxides and sulfides, such as (Mg,Fe)O and Fe_2O_3 [241–243], silicate bridgmanites [244, 245], and silicate post-bridgmanite [246] to above 100 GPa.

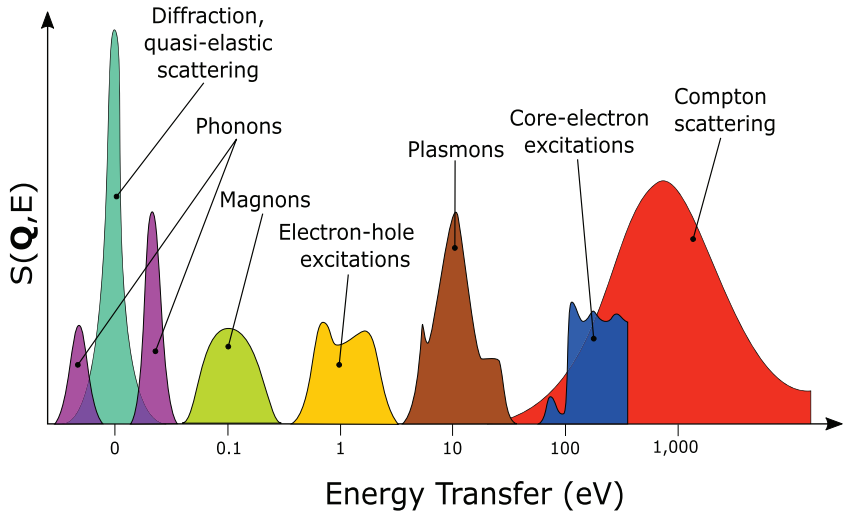

Figure 13. Approximate energy scales of different elementary excitations in condensed matter systems.

3.3.5. HP resonant x-ray emission spectroscopy and partial fluorescence yield. Both resonant XES (RXES) and partial fluorescence yield (PFY) can be viewed as a combination of XES and XAS. Instead of collecting transmitted x-rays or total fluorescence yield as in XAS, emission spectra are measured at each step as the incident beam energy is changed or scanned across an absorption edge. Therefore, the emission signal can be collected in a 2D map of the incident energy versus emission energy. The projection to the incident and emission planes gives the PFY and RXES, respectively [11]. The energy resolution in XAS (using a transmission geometry or total fluorescence yield) is limited by the core-hole lifetime broadening. This broadening can be partly overcome by detuning the incident photon energy with respect to the resonance energy. Because the lifetime broadening of the final state is considerably smaller than that of the core excited state, this resonant method significantly enhances footprints of electron states, and has a remarkable sharpening effect in projected spectra in PFY [11, 247]. For example, HP PYF spectra have allowed for resolving crystal-field splitting of Fe^{3+} in Fe_2O_3 [247]. For RXES, there may be no clear sharpening effect. Depending on the density of states, the band width of XES measured around an absorption edge can be either narrower or broader than that measured under non-resonant conditions [248]. HP RXES has been successfully used for quantitatively measuring the development of multiple electronic configurations with differing 4*f* occupation numbers, revealing information on the delocalization of the strongly correlated 4*f* electrons [249, 250]. Intermediate spin state of Fe_3O_4 at 15–16 GPa has been identified by combining XMCD and RXES [56].

3.3.6. HP x-ray fluorescence spectroscopy. X-ray fluorescence spectroscopy (XFS) measures the solubility of materials in fluids at HP [251, 252]. The method can be used for multi-element analytical probes and for studies of dissolution kinetics [253, 254]. In XFS experiments, the fluorescence signals (e.g. K_α, K_β, or both) are collected by a solid-state energy dispersive detector. Currently, the detection limit for HP XFS is at a few ppm level for elements down to atomic number 22 (Ti) and to a pressure of 10 GPa at high temperatures to at least 1273 K [254–256]. A confocal geometry has been developed for minimizing unwanted background signals [257], further improving efficiency and consequently lowering the detection limit.

3.4. HP inelastic x-ray scattering

Inelastic x-ray scattering (IXS) measures the dynamic structure factor $S(E,Q)$, which is a function of momentum transfer Q and energy transfer E. The dynamic structure factor contains information of all electronic excitations, including phonons, magnons, core-electron excitations, plasmons, the collective fluctuations of valence electrons, and Compton scattering (figure 13). Compared to other inelastic scattering techniques (inelastic neutron scattering, inelastic electron scattering, light Brillouin and Raman scattering), IXS is well suited for HP sample environments because of the penetrating power of hard x-rays, small focused beamsize from highly collimated synchrotron radiation, and large Q coverage (figure 14). Contrary to Brillouin or Raman spectroscopy at visible wavelength, which is limited to the very small Q range near the Brillouin-zone center, the wave-vectors in hard x-rays IXS are large and can be tuned continuously across the whole Brillouin zone. Inelastic neutron scattering usually requires large sample sizes, making the measurements on pressurized samples particularly challenging with only a limited pressure range (<1.8 GPa [258],). In addition, neutron scattering has limited Q coverage at low energy-loss region. Inelastic electron scattering requires an ultrahigh vacuum, in direct contradiction to HP conditions.

The cross section in IXS is usually small, requiring broad angular acceptance for enough signals. However, HP samples are imbedded inside massive pressure vessels. The use of large angular acceptance causes overwhelming contributions from surrounding materials, often rendering HP IXS experiments unfeasible. Therefore, tight collimation in the detection side is essential, causing the count rate in HP IXS experiments to be several orders of magnitude less than those at ambient conditions. Recently, this problem has been partially overcome by using an x-ray focusing optic (e.g. x-ray polycapillary,

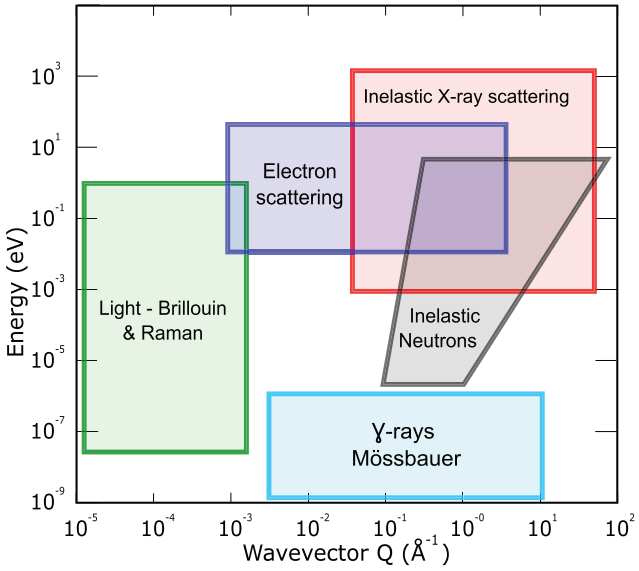

Figure 14. Energy ranges and wavevector coverages to measure the dynamic structure factor with various techniques.

figure 9) [162]. The focus provides the desired depth resolution, significantly discriminating sample signals from those arising from surrounding materials.

In the last decade, several methods have been developed for HP studies: non-resonant inelastic x-ray scattering or x-ray Raman scattering, resonant IXS (RIXS), nuclear resonant IXS (NRIXS), nuclear forward scattering (NFS), and Compton scattering (CS). Depending on the energy resolution required, different x-ray spectrometers have been constructed: low energy resolution IXS (LERIX) with a typical energy resolution of 1 eV, medium energy resolution IXS (MERIX) with 30–300 meV, and high energy resolution IXS (HERIX) with 0.3–3 meV.

3.4.1. HP non-resonant inelastic x-ray scattering. In non-resonant IXS (NIXS), high energy x-rays excite core electrons to an unoccupied state [259, 260]. It is analogous to the optical Raman scattering in terms of the excitation process, thus sometimes referred to as *x-ray Raman scattering*. The difference lies in the exciting energy that is in the x-ray regime, with corresponding excitations from core electrons. The use of high energy x-rays provides the penetrating power and removes the constraints of soft x-rays or electron beams in the studies of electronic structure of the material, making the NIXS a well-suited technique for studying electronic properties at HP using HP devices.

Near core-electron absorption edge features, for example, reveal information on chemical bonding. Such information is particularly pronounced and important for light elements, but has been inaccessible for HP studies as the pressure vessel completely blocks the soft x-rays or electron beams. With NIXS, the high-energy incident x-ray penetrates the pressure vessel and reaches the sample. The scattered photon transfers a portion of energy corresponding to the *K*-edge of the low-*Z* sample, but can still exit the vessel to be registered on the analyzer-detector system. Inelastic *K*-edge scattering spectra of second-row elements from Li (56 eV) to O (543 eV) at HP opened up a wide new field of near *K*-edge spectroscopy of the second row elements, such as graphite [72, 261], boron [262, 263], hydrocarbons [264], oxygen in glasses (SiO_2, B_2O_3, GeO_2, $MgSiO_3$) [265–267], and H_2O [268, 269]. Because the features in NIXS are sensitive to local 'short range' structure, the technique has been particularly useful in revealing structural changes in non-crystalline materials at HP. Pressure has dramatic effects on the energy and dispersion of all electronic bands. HP NIXS probes valence and conduction electronic structures at low energies up to a few tens of eV from the elastic line, and has been successfully applied to study Fermi surface [270], excitons [271, 272], plasmons [273, 274], and their dispersions at HP, by scanning both energy E and momentum transfer Q to obtain the dielectric function $\varepsilon(E, Q)$ and the dynamic structure factor $S(E, Q)$. Depending on the resolution required, two kinds of instruments are used: LERIX and MERIX. In general, LERIX setup is used in many HP NIXS experiments; while MERIX is more commonly used in resonant IXS.

3.4.2. HP resonant inelastic x-ray scattering. When the energy of the incident x-rays is tuned to resonate with one of x-ray absorption edges of the system, it is the so-called resonant inelastic x-ray scattering (RIXS) [275]. The resonance can greatly sharpen the IXS features and enhance the inelastic scattering cross section by orders of magnitude [11, 275]. RIXS in transition-metal and rare-earth systems gives important information on the electronic states, such as the intra-atomic multiplet coupling, electron correlation, and inter-atomic hybridization. Unusual phase transitions driven by electron correlation effects occur in many transition metals and their compounds at HP. The nature of these transitions, including the relationships between the crystal and electronic structures and the role of magnetic moment and order, is an area of active study [11, 249, 275–277]. For the incident energy at the main absorption edge, RIXS is dominated by charge excitations. In the pre-edge region, *d*–*d* excitations and orbital transitions are emphasized.

Both LERIX and MERIX instruments can be used for HP RIXS studies [11], depending on the energy resolution required for the subject of study. Because the incident energy is chosen by the absorption edges of the system, keeping high energy resolution in RIXS is not a trivial task. Significant efforts have been made to improve the energy resolution to probe fine electronic structures, including Bragg angle close to back-scattering geometry and the use of diced crystals coupled with an area detector [275, 278]. For RIXS using MERIX instruments, only a limited number of suitable analyzers have been established [279].

3.4.3. HP meV resolved inelastic x-ray scattering. Exploration of phonon dispersion used to be the domain of inelastic neutron scattering (INS). Although it has been long recognized that x-rays may also be used to probe lattice dynamics, it was not until the arrival of the third generation synchrotron that the meV resolved IXS (also referred as HERIX) was established for measuring phonon dispersion, first at HASYLAB [280], Germany, and then at ESRF [281], APS [282], and Spring-8 [283]. The HERIX instrument is designed to study the phonon

dispersion in crystals and the collective atomic excitations in disordered systems. Again, the penetration ability of high x-ray energies and the small beam make this technique suitable for HP studies.

HERIX has been applied to studying the HP elasticity anisotropy of *f*-electron metals [284, 285]. Sound velocities of materials at HP to over 1 Mbar have been measured [12, 286–288] using HERIX. With single-crystal samples, complete phonon dispersions in the Brillouin zone can be mapped by HERIX at HP [101, 289, 290]. However, lattice dynamical data at HP are still limited, largely due to constraints by the strict requirements of sample quality, hydrostaticity, and, to some extent, beam time availability. Recently, a compact laser heated DAC has been integrated with the HERIX instrument [291]. Sound velocities of iron and iron alloys have been measured at HP-HT conditions [292–295].

Most HERIX experiments remain flux limited. Special effort must be made to both maximize the transmitted radiation and minimize backgrounds. Air scatter can be a significant background at low momentum transfers (e.g. $<20\,\mathrm{nm}^{-1}$, and especially $<5\,\mathrm{nm}^{-1}$), while diamonds, gaskets, or pressure medium can contribute both inelastic (phonons) and elastic scattering. Often, single-crystal windows (e.g. diamond anvils) produce only a well-defined phonon background.

3.4.4. HP nuclear resonant inelastic x-ray scattering. In nuclear resonant IXS (NRIXS), incident x-rays of meV resolution are tuned near the exceedingly narrow nuclear resonant line (at neV level). By using time discrimination electronics, the delayed signals caused by the narrow nuclear absorption provide NRIXS data [154] (figure 15). The narrow meV bandwidth of x-rays is in a range comparable to that of vibrational excitations. Thus, nuclear resonant scattering yields element specific information on lattice dynamics, such as the partial phonon density of states (DOS), through an inelastic scattering process. In principle, the DOS provides constraints on vibrational dynamic, thermodynamic, and elastic information of a material, including vibrational kinetic energy, zero-point vibrational energy, vibrational entropy, vibrational heat capacity, Debye temperature, Grüneisen parameter, thermal expansivity, longitudinal velocity, shear velocities, bulk modulus, and shear modulus.

NRIXS measurements were first carried out on ^{57}Fe in its bcc iron at ambient conditions [296, 297]. The NRIXS technique has been extended to HP and obtained the DOS of ε-Fe up to over 1 Mbar [63, 155] and as a function of pressure and temperature with resistively heating and laser-heating techniques [138, 298, 299]. The measurement of Debye sound velocity [300, 301] distinguishes compression and shear wave velocities as well as their temperature and pressure dependence. This technique also allows determination of anisotropy of sound velocities and mode Grüneisen constants [300, 302].

3.4.5. HP nuclear forward scattering. In nuclear forward scattering (NFS), synchrotron x-rays are used to excite the resonant nuclei coherently and the re-emitted radiation is recorded by the avalanche photo-diode detector in the forward direction [154, 303] (figure 15). The timing circuit measures the time elapsed between excitation and re-emission and removes prompt events. The delayed forward scattering measures the Mössbauer effect in time domain; hyperfine splittings are reconstructed from the time-dependent intensity. Thus NFS is also called *synchrotron Mössbauer spectroscopy*.

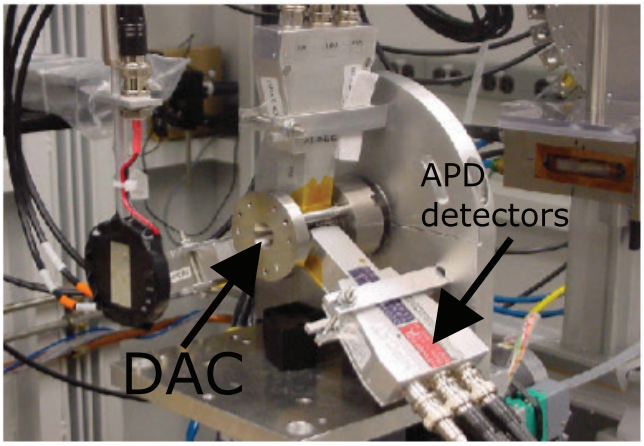

Figure 15. Photograph of an experimental setup for NRIXS at 16-ID-D HPCAT: a panoramic DAC is surrounded by three avalanching photodiode (APD) detectors placed very close to the sample position.

Because of the high brilliance and highly focused beam, NFS is well suited for, and has been extensively used in, HP studies. The NFS hyperfine signals are very sensitive to internal magnetic fields, electric field gradients, and isomer shifts [304–306], and has been used to study HP behavior of materials at megabar pressures, such as magnetic collapse [173, 244, 241, 242], site occupancy [245, 307], and valence and spin state [308–311]. Fast NFS experiments have been performed to determine the HP melting temperatures of iron [312], by measuring the Lamb–Mössbauer factor which describes the probability of recoilless absorption.

3.4.6. HP Compton scattering. Compton scattering is an inelastic scattering at high momentum transfer that probes electron momentum distributions. Using intense high energy x-ray source, high resolution Compton profiles can be measured. The challenge at HP is mainly related to the elimination of the background scattering from surrounding materials, such as the gasket and anvils. In Compton scattering measurements, the background scattering often overlaps with the spectral region of actual interest.

There have been few reports on Compton scattering studies under HP. The availability of intense synchrotron radiation sources, particularly the high brightness at very high energies (~50 keV), together with the development of high-resolution spectrometers, are opening up new classes of Compton scattering experiments on small samples at HP. The method has been applied to elemental solids such as Na, Li, and Si [313–315].

3.5. HP x-ray imaging

From the beginning of HP-SR experiments, HP x-ray imaging techniques have been used for locating HP sample position

and defining sample shape [316, 317]. Now, a variety of HP x-ray imaging techniques have been developed for various imaging purposes, such as HP radiography, HP tomography, using the full-field imaging method or the position scanning method. Recently, HP coherent x-ray diffraction has been developed for nano-size materials. X-ray topography provides information of internal strain and defects of crystals. Although there is no HP topography work reported so far, x-ray topography images are used for selecting diamond anvils [318] and improving the synthetic procedures in the CVD diamond crystal growth process [319].

3.5.1. HP x-ray radiography. HP radiography provides density contrast information through which the sample configuration inside the pressure chamber can be monitored. Often, because of the small beam in HP synchrotron experiments, radiography images are obtained by scanning sample positions. The position scanning radiography is used in almost all HP synchrotron experiments and provides information on sample allocation, sample configuration, anvil deformation etc [45]. By selecting proper monochromatic beams, absorption intensity contrast may be used for density determination for amorphous and liquid materials [77, 320, 321].

It should be noted that the position scanning imaging can be applied in any x-ray measurements. For example, by fast XAS measurements, images in chemical compositions and valence states may be obtained [223]. With increased brilliance and detection efficiency, many other measurements, such as XRD, XES, NFS (Mössbauer), may be used for mapping samples, providing images based on information of structure, valence state, spin, site occupancy, etc. HP scanning imaging has great potential for detailed information not only from a single spot but from the entire sample. The image resolution in the position scanning method is limited by the beam size.

HP radiography can also be obtained by the full-field method, in which the incident beam is large, relative to the sample size. Intensities of the transmitted x-rays are recorded by a camera and monitored by a phosphor screen which converts x-ray contrast into visible light. The full-field radiography is fast, allowing for efficient recording dynamic processes in HP experiments. For example, a probing sphere can be *in situ* monitored for viscosity measurements of liquids at HP [322–324]. Full-field radiography is often used in HP ultrasonic measurements for sample dimensions. X-ray focusing optics (e.g. zone-plate) may be used as an 'objective lens' similar to an optical microscope. With this, the resolution in full-field imaging can be increased significantly at the cost of the field-of-view. Such a transmission x-ray microscope (TXM) has a typical resolution of ~20–30 nm with a field-of-view of about 15 μm in diameter [325, 326].

3.5.2. HP x-ray computed tomography. With the development of micro- and nano-beam technology and intense synchrotron high energy x-ray sources, it is now possible for x-ray computed tomography (CT) to provide images with high spatial and temporal resolutions in three dimensions and as a function of time (4D). X-ray CT has become a powerful tool for the real-time characterization of microstructural and morphological evolution under HP. Laboratory-based x-ray CT systems are limited to relatively low x-ray energies and lengthy (1–2 h) image acquisition times. Third-generation synchrotron light sources afford unprecedented x-ray flux; by coupling with a high-speed camera, we can obtain x-ray radiographs at millisecond level and collect tomographic data in ~1 s. Adding a sample compression cell makes it possible to study the dynamic deformation of materials *in situ* at a 10^{-2} strain rate.

One of the most important variables under pressure is the volume or density. Unlike the Bragg peaks of crystals that measure unit cell volume directly, amorphous diffraction peaks only give a rough estimate of the volume [327]. HP x-ray CT can provide direct volume determinations with tens of nanometer resolution, and has been successfully used to determine the effect of pressure on the volume change [325, 327, 328].

X-ray CT is capable of non-destructive imaging with a 30 nm spatial resolution allowing the 3D tomographic reconstruction of samples with very small features. This has been recently demonstrated in the molten iron distribution in the 3D reconstructions of samples prepared at varying pressures and temperatures using a laser-heated DAC [329]. In previous measurements, the determination of dihedral angles, which describe the ratio of the solid–liquid interfacial energy and the solid–solid interfacial energy, using transmission electron microscopy or backscattered electron microscopy may not generate satisfactory statistics, especially for HP conditions. Furthermore, when the solid phase is anisotropic, the interfacial energy may vary with crystallographic direction, leading to multiple dihedral angles, for which 2D imaging cannot account. With the x-ray CT, the 3D imaging shows that, as the pressure increases from 25 to 64 GPa, the iron distribution changes from isolated pockets to an interconnected network (figure 16) [326], which has important implications in the formation of the Earth's core.

3.5.3. HP x-ray phase contrast imaging. In x-ray radiography or tomography, imaging relies on the absorption (or density) contrast. In phase contrast imaging (PCI), it records variations in the radiation phase [330, 331]. Variations in attenuation (thickness, density) and the x-ray refractive index of a sample lead to a change in the shape of an x-ray wavefront passing through the sample. By recording the intensity of the wavefront at a sufficient distance from the sample, intensity variations due to sharp changes in attenuation and refractive index in the sample can be detected. At grain boundaries, the sharp variations in refractive index can lead to strong phase contrast, even with polychromatic radiation [330]. PCI is especially useful in imaging weakly scattering materials, where the density contrast may also be weak. Subtle phase retrieval may be obtained by using x-rays of differing energies [332].

The use of PCI in HP studies is only beginning to be recognized. With fast detectors, fast PCI measurements have been used for studying the dynamic response of materials at extreme conditions. Dynamic phenomena at ns to μs timescales can be recorded with 3 μm spatial resolution [13, 14]. PCI has been used to study the immiscibility of two or more liquids in a system [333] (figure 17).

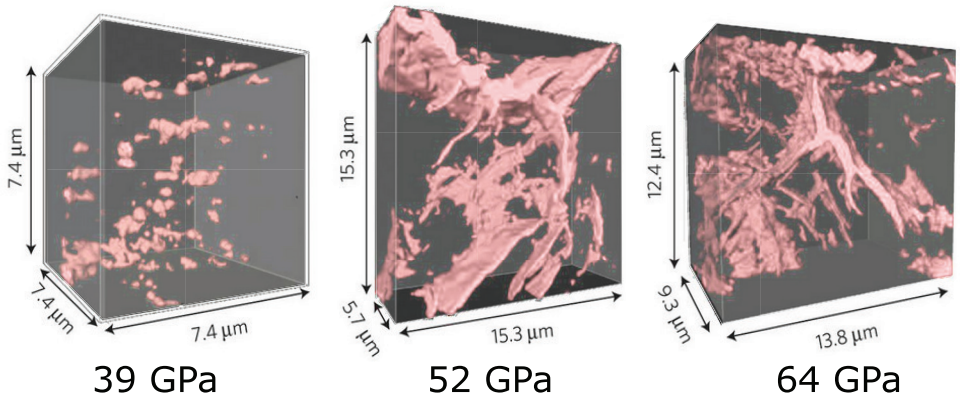

Figure 16. Sub-μm resolution tomography images showing the 3D distributions of iron alloy melt in bridgmanite. Samples were synthesized in laser heated diamond anvil cells at various pressures. (Modified with permission from [326]. Copyright 2013 Nature Publishing Group.)

3.5.4. HP coherent imaging. Coherent diffraction imaging (CDI) has been a subject of considerable research over the past decade [334–336]. The CDI technique allows for 2D or 3D reconstructions of nanoscale structure images. In CDI, a highly coherent x-ray beam is scattered by the object and produces a diffraction pattern downstream. This recorded pattern is then used to reconstruct an image via an iterative feedback algorithm, converting the reciprocal space pattern into a real space image. As coherent x-rays pass through a distorted crystal, both the scattering intensity and phase will be affected. CDI is therefore sensitive to the internal strain distribution of individual nanometer-sized single crystals [19, 336].

CDI has been used for morphology and 3D strain distributions of HP samples [17–19] (figure 18). Compared to the state-of-the-art XRD technique, which provides internal strain distribution along the beam penetration direction with about 1 μm point-to-point spatial resolution and a strain sensitivity of 10^{-3} [337], CDI provides superior spatial resolution (<30 nm) and strain sensitivity (1×10^{-4}) [19].

Another coherent based imaging technique is x-ray photon correlation spectroscopy (XPCS) [338], which has become a powerful probe of materials dynamics. XPCS is the x-ray analog of dynamical light scattering and measures speckle pattern by the scattered coherent light originating from a material with some inhomogeneities. When the arrangement of the system changes over time, the time dependence of the speckle pattern in XPCS can be used for studying the dynamics of the system [339]. XPCS can be well integrated with HP devices to address the dynamics of HP liquids/fluids, HP melting, HP glass transition, etc. No HP XPCS work has been reported so far.

4. High-pressure research using synchrotron x-rays

With the advancement of powerful microsampling synchrotron probes, materials' structural, electronic, magnetic, mechanical, and phonon properties have been widely studied under HP in the past decade. Matter under extreme conditions has become a forefront area of research activities across the scientific disciplines, including physics, chemistry, materials science, earth and planetary sciences, and biology. Some studies

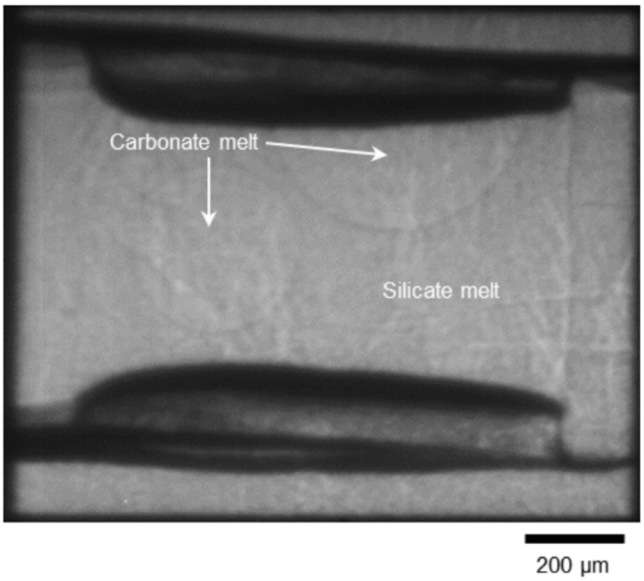

Figure 17. A phase contrast image of carbonate and silicate melts using a polychromatic x-ray beam, which shows two immiscible melts at high pressure. (Courtesy of Yoshio Kono.)

deal with old quests that have finally become within our grasp; some are surprising, novel phenomena that challenge our conventional wisdom; some have big societal impacts in various fields. In this section, we review the progresses in HP scientific studies using synchrotron x-rays in recent years.

4.1. Structure of materials

The ability of pressure to change inter-atomic distances strongly leads to a variety of pressure-induced structural and electronic changes, resulting in intriguing structural forms at HP. Determining the atomic arrangement is an essential prerequisite for understanding the effect of compression or decompression on materials and their structure-property correlations for predictive models of novel materials and new applications.

4.1.1. HP crystallography. Crystallography deals with the arrangement of atoms in crystalline solids. It has been the

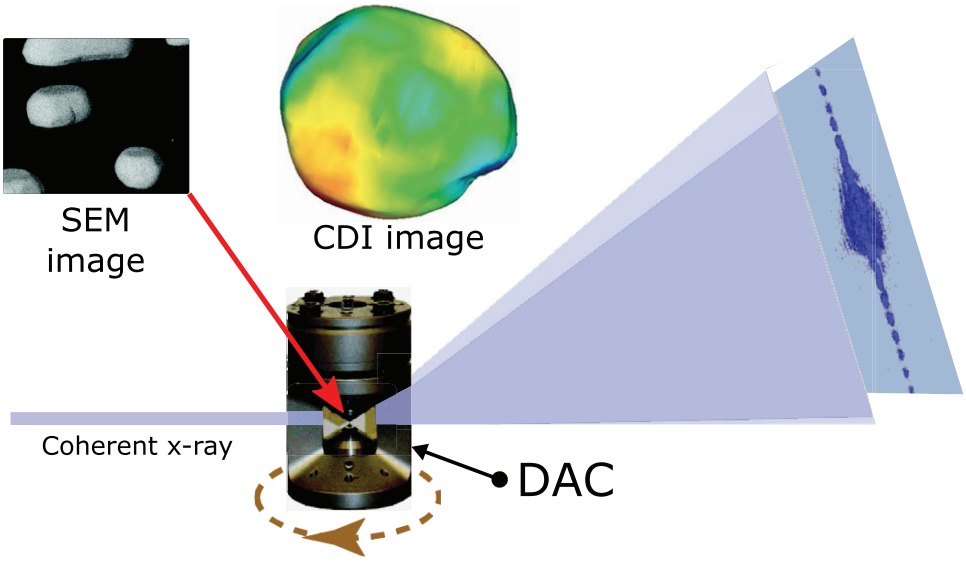

Figure 18. A large opening panoramic diamond anvil cell for collecting coherent diffraction images at high pressure. The left inset shows a scanning-electron microscopy (SEM) image of gold nanoparticles distributed on a silicon substrate. The right inset displays the coherent diffraction image of phase shift distribution pasted on the 30% isosurface plot. (Modified with permission from [19]. Copyright 2013 Nature Publishing Group.)

primary field of HP studies using synchrotron radiation, and will likely remain so in future because of its key role in understanding the effects of compression on structures. In early years after the invention of the DAC, initial experiments were successfully used for crystallographic structural determinations at HP [340–344]. In the last two decades, with the greatly improved x-ray flux and small probe size from SR and developments in HP technology, HP crystallography has undergone a significant surge, not only in the number of studies carried out by the fast growing community, but also in the ability to determine the detailed crystal structures of materials at extreme conditions, including surprising novel structures at HP. An example is the complexity of structure revealed at HP. Contrary to the conventional understanding that the crystal structures at HP becomes increasingly simple like arrays of closely packed balls, HP increases the interaction of the inner electrons, and atoms may become irregularly-shaped and non-spherical, resulting in very complicated crystal structures and very large unit cells [345, 346] (figure 19). The striking structural complexity is found to exist in many elements, including the widespread existence of incommensurate structures at HP [347–350].

A comprehensive review by McMahon and Nelmes [351] categorizes the complex structures into four types: incommensurate composite structures, incommensurate modulated structure, modulated layer structures, and other complex structures. Incommensurate composite structures comprise of two interpenetrating components, a 'host' and a 'guest', which are incommensurate with each other along one or more axes, e.g. in Ba [352], Sr [353], Rb [354], Sb [355, 356], and Sc [357]. Incommensurate modulated structure can be viewed as a basic structure with the atoms displaced by a modulation wave, which is incommensurate with the basic unit cells. Examples of these types of structures include Te, Se, S, I, and Br [349, 350, 358–360]. Modulated layer structures consist of various different stacking sequences of similar 8-atom and

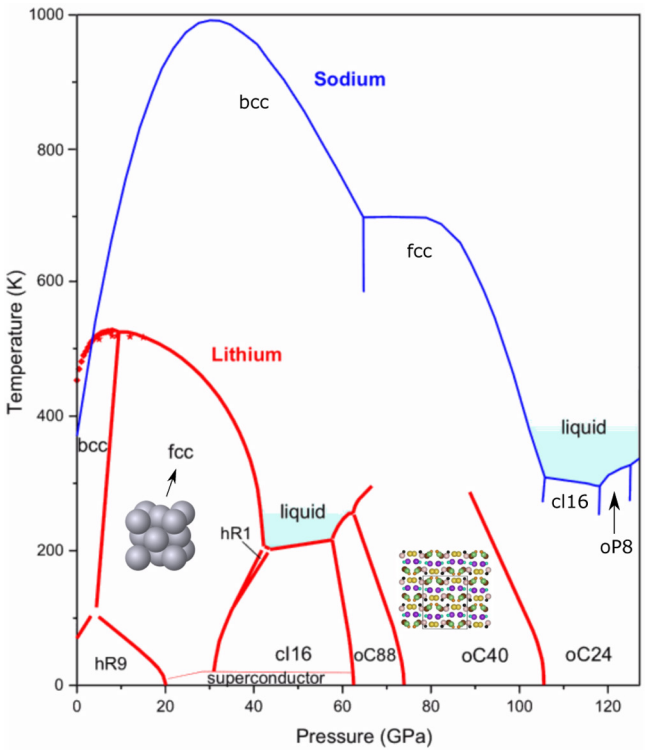

Figure 19. Phase diagram of lithium (red) and sodium (blue). Both lithium and sodium display steep melt-downs, with melting temperatures even below room temperature at 50 GPa and 110 GPa, respectively. The underlying solids have complex structures with large unit cells. (Courtesy of O Degtyareva (modified).)

10 atom layers at HP, such as in Li [361], Cs [362], Rb [363], and Ga [364]. These complex structures are not only widely observed, but are stable over wide ranges of *P-T* conditions.

The development of HP single-crystal XRD [102, 185, 365, 366] has even enabled detailed structural studies of complex phases for weakly scattering materials and at pressures above 200 GPa. Besides the information on atomic arrangement,

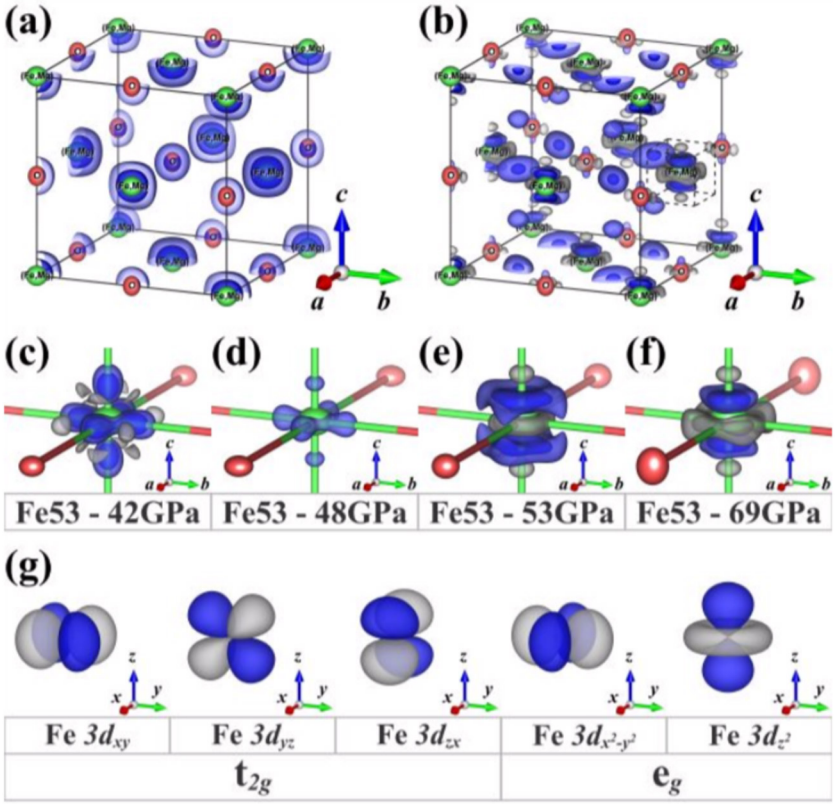

Figure 20. Electron density distributions of a ferropericlase sample at high pressures. (a) $(Mg_{0.47}, Fe_{0.53})O$ at 69 GPa, illustrated in the form of thermal ellipsoids at 50% probability. Fe/Mg: light green, O: light red. (b) The deformation density map of $(Mg_{0.47}, Fe_{0.53})O$ at 69 GPa. The positive and negative electron densities are illustrated by blue and gray colors, respectively. The contour is set at 0.5 $Å^{-3}$. (c)–(f) The deformation density maps at a local position at pressures of 42, 48, 53 and 69 GPa, respectively. (g) Illustrated *d*-orbitals of Fe^{2+}.

electron density analysis under pressure has recently been performed [102, 103, 367, 368]. For instance, the change in electron density distributions has been monitored across a spin transition of Fe^{2+} in (Mg,Fe)O (figure 20) [369]. In the deformation density maps (figures 20(c)–(f)), the positive deformation is shown in a blue color and the negative in grey color. In Fe^{2+}, there are five d-orbitals, with three t_{2g} (d_{xy}, d_{yz}, d_{zx}) and two e_g (d_{x2-y2}, d_{z2}) orbitals shown in figure 20(g). A high (low) spin state of Fe^{2+} would mean positive (negative) deformation values on the axis directions and negative (positive) in the diagonal directions. Figure 20(c) shows a clear high spin state as indicated by the positive electron density in the axis direction and negative in the diagonal directions of the basal plane, corresponding to the t_{2g} orbitals. Both positive and negative deformation densities decrease at 48 GPa (figure 20(d)). At 53 GPa, the inverse signs are observed, and become more obvious at 69 GPa (figures 20(e) and (f)), indicating the high spin to low spin transition.

In many cases, our structural knowledge at HP is based on limited information from powder x-ray diffraction, because it is often difficult to preserve a single-crystal sample at HP due to phase transitions and/or non-hydrostaticity. HP multigrain crystallography has been recently developed for single-crystal structure determination [152], which is particularly useful for studying the structural properties of phases that are not recoverable at ambient condition. For instance, structure refinement has been made for $(Mg,Fe)SiO_3$ post-bridgmanite at pressures above one megabar [167]; electron density distribution of β-Ge has been determined at 12 GPa [103, 370]. With the precise structural determination enabled by the multigrain approach, it is anticipated that many previously determined HP structures will be revisited with the technique. For example, a new hexagonally structured $(Mg,Fe)SiO_3$ phase has been discovered at a pressure range of 95–108 GPa [195], suggesting that the lower mantle may contain previously unidentified major phases; dislocations in grains of $MgGeO_3$ post-bridgmanite has been determined at 90 GPa [371]; the crystal structure of seifertite (SiO_2) as a minor phase in a sample at 129 GPa has been refined [168].

4.1.2. Non-crystalline materials. Due to the lack of long-range periodicity, atoms in non-crystalline materials have more degrees of freedom, with richer physics and chemistry under HP [372–379]. Structural determination for non-crystalline materials has been challenging. The observation of 'halos' in XRD from liquids and glasses mean that non-crystalline systems possess a distinct local structure. The pair distribution function, extracted from XRD or EXAFS, is often used for structural description [60, 179, 196, 380] and directly compared to theory and simulation results. The dynamical x-ray structure factor, often obtained from IXS and nuclear scattering, provides information on collective excitations in liquids and glasses [381]. X-ray imaging enables the measurement of material properties including density [77, 327, 328]

and viscosity (e.g. [159]) in liquids. HP XRS allows direct probing of the chemical bonding changes of light elements in non-crystalline materials [268, 382]. Relatively speaking, HP XRD remains a primary technique for studying the structural evolution of non-crystalline materials [98, 121, 199, 205, 263, 265, 320, 383, 384–388], pressure-induced amorphization or melting [346, 389–398], and pressure-induced crystallization [58, 346, 392, 396, 399–401].

HP x-ray studies on non-crystalline materials started in the early 1970s on liquid sodium, up to 5 GPa [402]. Since the late 1980s, SR x-rays have been widely used for pressure induced structural changes in Se, Ga, and Bi liquids [197] and SiO_2 glass [201] using EDXRD, and coordination changes in GeO_2 glass [225] using EXAFS. Subsequently, ADXRD has been used for studying the structure factors of HP fluids [182] and amorphous iron [403] in the DAC. Coupled with laser heated DAC, the structure of liquid iron has been measured up to 58 GPa [404]. Recently, XRD measurements with a laser heated DAC provided evidence of a liquid–liquid transition in cerium [405].

Experiments on glassy and amorphous materials have shown that the amorphous–amorphous transition may occur in simple systems; for example, in H_2O [406], SiO_2 [60], GeO_2 [61, 205, 320], and metallic glasses [216, 388]. The ability to induce amorphous transitions with pressure, especially those that can be recovered to ambient conditions, provides a way of tuning materials properties that are likely unobtainable using any other method. For example, an unusual thermally induced densification, as large as 16%, is observed in a GeO_2 glass at 5.5 GPa [121]. The XRD data show that the large thermal densification is associated with a 4- to 6-fold coordination increase of Ge. In addition, identifying second order and other gradual transitions in disordered materials is important both for materials science and technological advancements.

The concept of polyamorphism (i.e. multiple structures of amorphous materials with the same composition separated by a first order phase transition) remains a fundamentally important and unresolved phenomenon [407]. A wealth of indirect evidence for such transitions has already been established in H_2O [406], SiO_2 [201, 408, 409], GeO_2 [61, 225, 410], Si [199, 411, 412], I [413], Se [413, 414], S [414, 415], P [198, 416], Ce [405]. However, unambiguous evidence for liquid–liquid transition has yet to be presented in the liquid state for any system.

Integration of multiple techniques is often essential for comprehensive studies of the relationship between structure and properties such as density, ultrasound velocity, viscosity, electric and thermal conductivity [159, 417]. Figure 21 shows an example of viscosity and structure data of KCl and NaCl liquids up to 7.3 GPa [324]. The viscosity of liquid KCl increases rapidly at 1.5–2.2 GPa, above which it remains virtually constant. Structural data of KCl liquid also showed a pronounced change. In contrast, no anomaly in viscosity and structure is observed for NaCl liquid under HP. These observations suggest that viscosities of KCl and NaCl liquids strongly correlate with the structure. The viscosity anomaly in liquid KCl is found to be at pressures close to those of the B1-B2 transition in solid KCl.

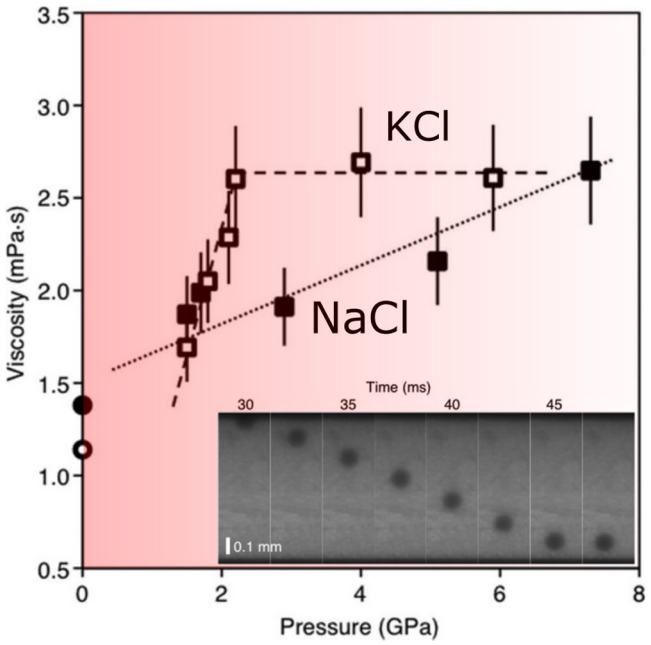

Figure 21. A falling sphere technique revealed an anomaly in the viscosity of liquid KCl at around 2 GPa, also associated with a pronounced change signified by the ratio of the nearest- and the second-neighbor distances. The results suggest that the viscosity anomaly in liquid KCl strongly correlates with structural changes. The inset images show the falling sphere recorded by fast x-ray imaging. (Modified with permission from [324]. Copyright 2013 by the American Physical Society.)

4.1.3. The ordering state in materials. In crystalline materials, short-range order (SRO) is generally correlated with long-range-order (LRO). For example, a perfect crystalline material displays a high degree of order in both SRO and LRO. Existence of defects, such as vacancies and stacking faults, decreases the coherence of crystal lattice, lowering the degree of order in both SRO and LRO. Some materials may show disorder in a particular sublattice, displaying crystallographic disorder in certain directions [418, 419]. If we consider quasi-periodicity as a LRO, quasicrystals can be viewed as having LRO as much as crystals. On the other hand, amorphous materials often show a high degree of SRO, especially when strong interatomic interactions are present, but lack LRO. Some amorphous materials may display medium-range order (MRO) at the nanometer scale [201, 403, 420]. Thus, in amorphous materials SRO is not directly correlated with LRO.

Recently, the ordering state of materials has been extended by expanding into regions where amorphous clusters can form a periodic lattice or where a glass possesses a hidden single-crystal order. Wang *et al* [421] showed that C_{60} molecules from a crystalline solvated fullerene phase undergo an order-to-disorder transition under HP but keep their translational symmetry (figure 22). It is remarkable that a material can still possess long-range order even though its fundamental building blocks are disordered. In contrast, HP experiments on metallic glasses revealed a glassy state possessing a topological LRO, which is referred to as a perfect glass state [200]. These studies open the door for exploring materials with various degrees of ordering state, with potential for a variety of physical and chemical properties.

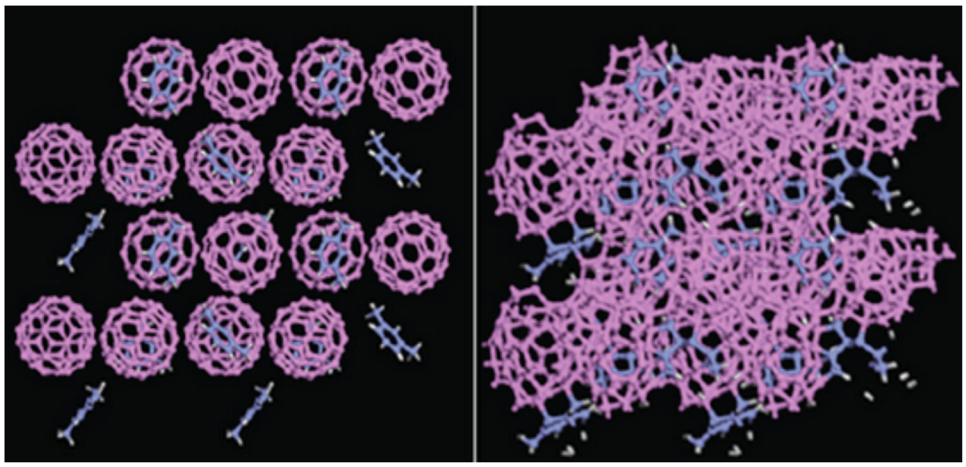

Figure 22. C_{60} can still possess long-range order even though its fundamental building blocks are disordered. (left) The pristine structure of the C_{60} cages which is elastic below ~30 GPa. (right) Above 30 GPa, many carbon–carbon bonds break down, causing locally disordered building blocks, while the long range order still holds. (Modified with permission from [421]. Copyright 2012 American Association for the Advancement of Science.)

4.2. Equations of state

Equation of state (EOS) describes the relationship between state variables (pressure, volume, temperature, etc), displaying the state of matter under a given set of physical conditions. The application of pressure for EOS studies is of primary importance because the complementary variable to pressure is volume, whereas that to temperature is entropy. In theoretical simulations, it is comparatively easier to calculate the free energy of materials with different volumes, than to deal with all different sources of entropy. Thus, experimental data of pressure-volume EOS is widely used for validations of theoretical models.

The Birch–Murnaghan EOS is a type widely used in HP studies. It is based on finite strain theories using the Eulerian strain measure, with its third-order form as:

$$P = \frac{3K_{T0}}{2}(X^{-7} - X^{-5})\left[1 - \frac{3}{4}(4 - K'_{T0})(X^{-2} - 1)\right] \qquad (4.1)$$

where $X = (V/V_0)^{1/3}$ is the linear compression; subscript 0 denotes the parameter at ambient pressure; K_{T0} and K'_{T0} are bulk modulus and its first pressure derivative, respectively. For materials under very strong compression, EOS based on exponential repulsive potentials, such as that of Vinet [422], are superior to finite strain theories. The Vinet EOS is expressed by:

$$P = \frac{3K_{T0}(1 - X)}{X^2}\exp\left[\frac{3}{2}(K'_{T0} - 1)(1 - X)\right] \qquad (4.2)$$

A variety of other equations of state that are applicable to various classes of materials have been proposed (e.g. [423, 424]). To describe thermal equations of state, several forms are proposed, including high temperature Birch–Murnaghan EOS, thermal pressure EOS, and lattice dynamics model (see [425] and references therein).

With the advances in SR-HP techniques, there is a growing amount of published EOS data. At the same time, the high volume of experimental data shows some discrepancies in literature primarily due to pressure scales and possible different sample environment, e.g. non-hydrostatic stresses. XRD data indicate that the pressure derived from different scales varies as widely as 7% at 100 GPa and room temperature (e.g [82]). The discrepancy could be even larger at high temperatures. Because the primary scales are still largely based on shock compression data, which carry a 5–7% uncertainty, an internally consistent approach has been used to establish a set of calibrates that are self-consistent with each other [82, 97, 426]. This approach is an important and necessary step towards a solution in dealing with large volumes of data. With the development of even smaller x-ray probes and efficient detection techniques, combinatorial studies for a large set of materials may be applied in a single sample chamber for internally consistent EOS data. Ultimately this must rely on the establishment of an absolute pressure scale based on self-consistent EOS measurements by simultaneous XRD and acoustic measurements (see section 2.4).

Ultrahigh pressures achieved successful determinations of EOS even at the early stages of synchrotron use; e.g. iron to 3 Mbar [33] and hydrogen to over 1 Mbar [80]. Large amounts of data on thermal EOS have been obtained using resistively heated DAC (e.g. [97, 125]) or LVPs (e.g. [427]). Although laser heated DAC can reach much higher temperature conditions, it remains experimentally challenging for thermal EOS studies (see section 2.7.4). A uniformly heated volume, much larger than the probing x-ray beam size, is required for reliable thermal EOS measurements.

Recently available fast x-ray detectors together with the high brightness of synchrotron beams allow fast data collection at synchrotron facilities. Applying this to EOS studies, thousands of data points can be collected quickly, as pressure or temperature is changed [110] (figure 23). Since pressure can be determined by including a few internal standards, high precision EOS data can be obtained.

4.3. Phase relations

The compression energy is comparable to typical bond strength. For example, for pressures below 10 GPa, the compression energy is comparable to hydrogen bonds; at $P > 100$ GPa, it is large enough to break a number of chemical

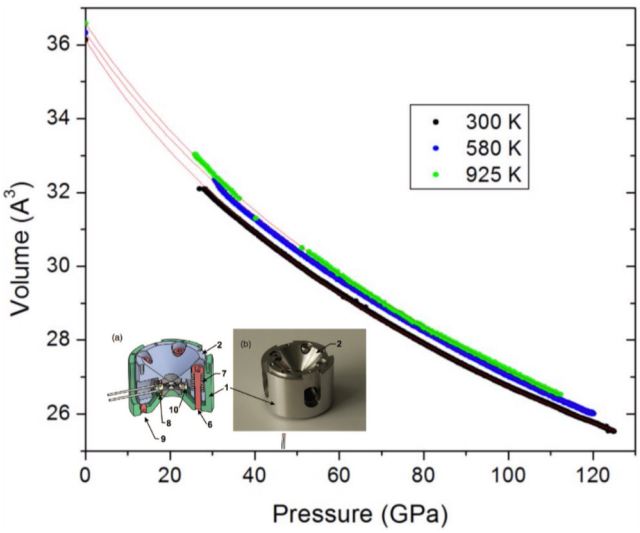

Figure 23. Fast collection of XRD data using rapid compression devices integrated with high temperature furnaces [108, 110]. Samples at elevated temperatures can be compressed in a few seconds to megabar pressures, resulting in thousands of XRD images in one fast loading process.

bonds, leading to a variety of pressure-induced structural and electronic phase transitions. Synchrotron x-ray probes have been widely used for phase relation studies.

4.3.1. Phase transitions. HP studies with x-rays contribute greatly to our knowledge of the phase diagrams of materials, as demonstrated in several books [428–430]. Atomic coordination and the structures of materials are governed, to a first approximation, by the geometric relation of 'hard-sphere' atomic radii. This geometrical concept has been one of the guidelines in searching for possible HP polymorphs, based on the low-*P* analogs of the next row elements on the Periodic Table [431]. For example, the classic *B*1-*B*2 transition in NaCl requires that the ratios of *r*(Na)/*r*(Cl) reduce below 0.73; this can only occur if *r*(Cl) decreases relative to *r*(Na) at high pressures [432]. This was later verified in all alkali halides. Another example is silicate materials. The small silicon fits in the site, surrounded by four large oxygen anions, at relatively low pressures. However, as pressure increases the ionic radius ratio of silicon and oxygen increases with the high compressibility of the oxygen anion relative to silicon, resulting in the conversion of all silicon tetrahedra in minerals into silicon octahedra at deep mantle conditions [433, 434].

For many oxides and silicates, the application of pressure forces the atoms to occupy a smaller volume, leading to HP structures composed of the closest-packed arrays of atoms. However, as discussed in section 4.1.1, because of the interaction of the inner electrons, irregularly-shaped atoms, and the resulting complicated structures, the phase diagrams of even single elements can be very complex. Both Li and Na display unusual 'melt-down' phenomena induced by quantum effects. When they eventually solidify at lower temperatures, the simple metals adopt a range of highly complex structures previously unobserved in any element. Na remains a liquid at room temperature at 110 GPa, while Li has a melting point of 190 K at 45 GPa, by far the lowest melting point among the elemental metals [345].

The HP effect is particularly dramatic on the relatively compressible simple molecular compounds. Under HP, molecular CO is converted into an extended polymeric solid with very high energy density [435]. Dry ice CO_2 becomes quartz-like and exhibits a rich phase diagram [436–442] and pressure-induced amorphization [443, 444]. With different arrangements of hydrogen bonding, H_2O alone has fifteen stable phases and an additional fifteen distinctive metastable crystalline, amorphous, and fluid phases [98, 268, 393, 395, 445–458]. Intermolecular interactions dictate the rich HP polymorphism [459] of solid oxygen. HP IXS of oxygen *K*-edge excitations to 38 GPa shows that O_2 molecules interact predominantly through the half-filled $1\pi_g^*$ orbital <10 GPa [460]. Enhanced intermolecular interactions develop because of increasing overlap of the $1\pi_g^*$ orbital in the low-pressure phases, leading to electron delocalization and ultimately intermolecular bonding between O_2 molecules at the transition to the ε-phase. The ε-phase, consisting of $(O_2)_4$ clusters [347, 348], displays the bonding characteristics of a closed-shell system.

HP studies also provide detailed knowledge of atomic-scale structural changes across phase transitions, which is essential for understanding the process and mechanism of the transitions. For example, silicon displays an intriguing precursor lattice at HP, which provides a clue to understand the process and mechanism of phase transitions in solids. The results from HP single-crystal XRD show that an embryonic phase can dynamically co-exist with the host lattice through collective motions [102]. This collective mechanism for the phase transition goes beyond previously considered reconstructive or displacive processes.

Despite the fast growing information on the phase diagrams of materials from HP studies with x-rays, the accurate determination of the phase equilibria and phase diagrams is not a trivial experimental task due to the kinetics of phase transitions and possible metastabilities. Depending on experimental conditions, such as hydrostaticity, compression and decompression rates, and temperature ranges, the determined phase relations may vary. The coexistence of two phases can appear in a large pressure range (e.g. [461]). Pressure induced amorphization has been reported for many materials. However, some of the effects previously reported as amorphization were likely due to the formation of nanocrystals or structural intermediates [462], or amorphization could be bypassed, if more hydrostatic pressure media were used [463–465].

4.3.2. High pressure melting. As a special case of phase transition, HP melting is the subject of extensive studies. When materials melt, their physical properties, such as density, viscosity, absorption properties, and electrical resistance, undergo a sudden change. Such property changes characterize a first order phase transition and are often used to signify melting. Unlike other first order phase transitions, melting is characterized by the loss of long-range order and resistance to shear. To definitively identify melting, both of these two characteristics must be demonstrated. Visual optical observation is

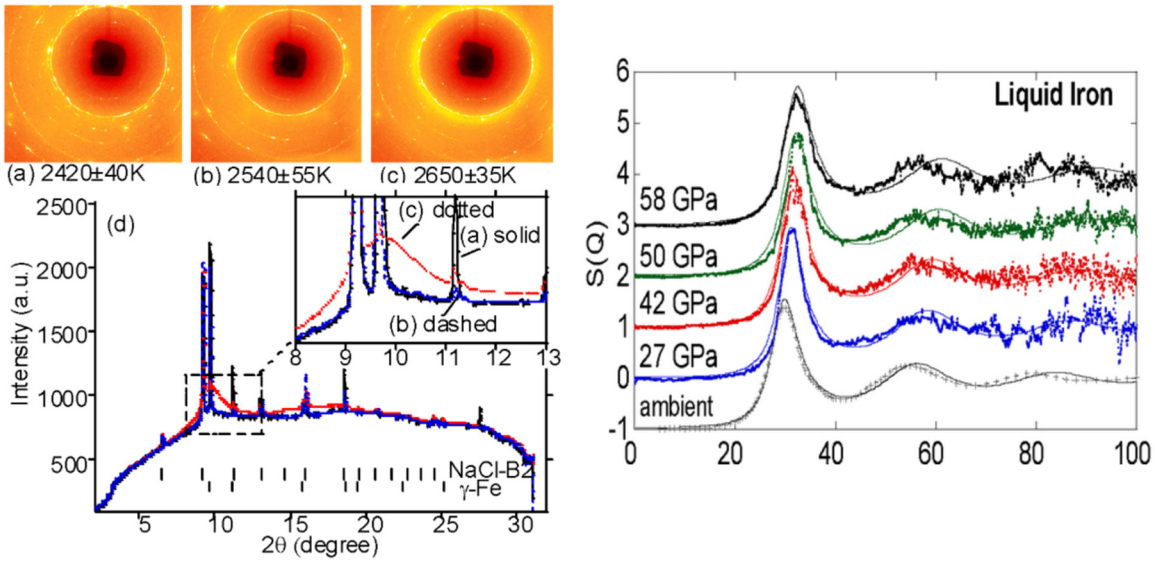

Figure 24. X-ray diffraction data signifying the melting of iron at 58 GP. The melting is identified by the appearance of a diffuse scattering band from molten iron. (a), (b), and (c) are x-ray diffraction/scattering images recorded at different temperatures; (d) integrated patterns corresponding to these images. The structure factor of liquid iron essentially preserves the same shape along the melting curve up to 58 GPa. (Modified with permission from [404]. Copyright 2004 by the American Physical Society.)

a common way to determine whether melting has taken place. It is obvious that fluid flow observation is a good measure of the loss of resistance to shear, therefore it has been widely used [466–469]. However, visual observation (fluid flow) is less obvious as pressure increases, making it difficult to unambiguously define the onset of melting.

Synchrotron XRD has been combined with laser heated DAC and used in melting studies to document the loss of long range order [404, 470, 471]. Melting at HP is identified by the appearance of diffuse scattering from the melt, with the simultaneous loss of crystalline diffraction signals (figure 24).

In addition to XRD, synchrotron NFS (section 3.4.5) is a promising probe to identify melting. NFS measures the atomic thermal displacement that can be used for documenting the rigidity of a material. Upon melting, the strong elastic resonance signal diminishes in NFS. The mean square thermal displacement of atoms (Lamb–Mössbauer factor) can be measured as a function of temperature, providing a plot for determining the onset of melting [302, 312]. Synchrotron x-ray absorption has also been successfully used for melting identification [142, 472].

Despite the success of using synchrotron x-rays in HP melting studies, discrepancies still exist in literature on melting lines, reflecting the difficulty of HP melting experiments due to the extreme conditions involved, possible chemical reactions, and/or unexpected diffusions. Unlike solid–solid phase transitions, kinetics is not a major limiting factor in determining melting. The challenge is mostly from several experimental aspects, including the *identification* of the onset of melting at well-defined *P-T* conditions (*assignment*), and fast measurements to avoid the effect of possible diffusion and chemical reactions. Another challenge is that the tail of x-ray beam, though typically $<10\%$ in intensity, contributes ~50% in total x-ray scattering (diffraction) due to the large covered volume. The laser heating area has to be sufficiently large to avoid contamination from the x-ray tail.

4.4. Electronic properties

Pressure dramatically alters electronic properties, such as bonding, hybridization, valence change, spin-paring, electron delocalization, etc, which has been widely studied, using HP single-crystal XRD, HP XRS, and HP IXS probes.

4.4.1. Bonding at high pressure. Bonding is usually characterized by the primary source of binding energy, such as ionic, covalent, metallic, van der Waals, and hydrogen bonding. However, at HP, a distinction on the classification of bonding becomes less clear. A few rules of thumb exist for structural and bonding changes at HP [473, 474].

In ionic bonding materials, such as NaCl and MgO, the atoms may be viewed as soft spheres, with anions more compressible than the cations. Much of the phase diagrams and the coordination number increases of such materials can be explained by the packing of various sizes of spheres. Covalent bonds tend to be directional between two (or more) nuclei, decreasing the interatomic repulsion. Upon compression, the nuclei are brought closer to one another, increasing the interatomic repulsion. The electron distribution must change and adapt to the compression, leading to changes in electronic structure. As a result, novel structural types with unusual bonds are observed even in elemental solids. Ge, a typical sp^3 covalent bond framework, transforms from cubic (α-phase) to tetragonal (β-phase) around 11 GPa. Pressured induced changes in electron density distribution happen at pressures far below the α-β transition pressure [103]. It is generally accepted that the metallic character of the β-Ge is related to the increased coordination and strong participation of *d*-orbitals in the bands. The observation of pressure-induced changes in electronic structure revealed a pre-transition process, providing information on how the covalent bonds form on the *ab* plane and the metallic bonding along the *c*-axis.

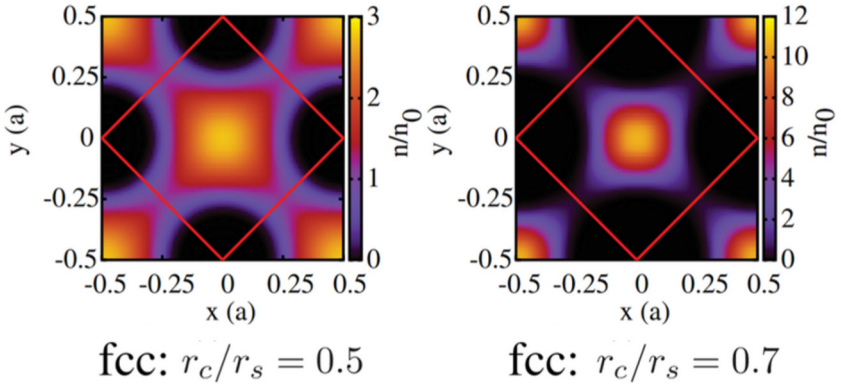

Figure 25. Interstitial electron localization. Electronic density displays a localized character as the ratio r_c/r_s approaches close packing. (Modified with permission from [479]. Copyright 2008 by the American Physical Society.)

The bonding in metals is viewed as positive ions embedded in a sea of electrons, with the negative electrons holding the ions together in a closely packed framework. The packing of equal-sized spheres maximizes at about 74% ($\pi/\sqrt{18}$) of the available space. Deformed spheres may yield more efficient packing [473, 475]. There could be many ways of deformation to reach an optimal packing of spheres. One example is the appearance of sublattices in elemental metals displaying complex structures [476]. An interesting aspect is that instead of adopting more close-packed structures, the observed structures consist of an open framework and the bonding appears to be more directional.

Hydrogen bonds are essentially ionic bonds involving H and O. A hydrogen atom is covalently bonded to an oxygen atom and attracted electrostatically to a neighboring oxygen ion. H_2O, a typical hydrogen bonding material, forms a symmetric hydrogen-bond state 'ice X' at 60 GPa [450]. In the ice X, the intermolecular O…H 'hydrogen bonds' no longer exist. All O–H bonds are equal in length and the molecular distinction of H_2O has completely disappeared.

4.4.2. Insulator, semiconductor, and metal. Insulator, semiconductor, and metal are categorized by their electrical conductivities. To transport electrons, partially filled states near the Fermi level are required. Metals have many partially filled states with energies near the Fermi level. Insulators, on the other hand, have few partially filled states, with the Fermi levels lying within band gaps. Semiconductors have a small band gap or intermediate states (e.g. by chemical doping where electrons are excited into conduction bands or holes in the valence bands).

Because compression leads to increased interaction among filled and unfilled orbitals, the metallization of insulators and semiconductors has been recognized since the early stages of HP research [477]. Indeed, many materials display electronic transitions under HP without distinct structural changes. For example, a pressure-induced semiconducting to metallic transition is found in multilayered MoS_2 at approximately 19 GPa [478]. The metallization is associated with only a slight lattice distortion and is characterized by pressure induced charge localization around the Mo atoms, which in turn gives rise to increased interaction between neighboring layers of sulfur atoms. It is also very common that pressure induced insulator-semiconductor-metal transitions are accompanied by structural changes. Well-known examples include Si and Ge, both transforming from semiconductors to metallic phases at 13 GPa and 11 GPa, respectively, accompanied by structural transitions from cubic to tetragonal β-tin structure.

For 'simple' metals such as Li and Na, we might expect them to become increasingly better conductors. Indeed, IXS experiments show that under 3.7 fold densification the solid Na of both bcc and fcc symmetry can be regarded as simple metals [274]. However, at extreme compression, core electrons overlap, shaping the local volumes available to electrons. It was predicted that the valence electrons could move to interstitial locations between the cores, and the crystal structure of the metal adapts to accommodate such electron-occupied interstices [479, 480] (figure 25). Sodium transforms into a dense insulating material that is optically transparent and lacks metallic characteristics at 200 GPa [481]. Lithium transforms to a semiconductor at 80 GPa [482], and then again to metal at 120 GPa [483, 484].

Unlike chemical doping and nano-size controls, pressure can be effectively used as a 'clean' tuning parameter affecting the interplay of electron correlation and lattice distortions. Vanadium oxides (VO_2 and V_2O_3) display interesting metal-insulating transitions, governed by two well-known phenomena: the strong electron correlation (Mott–Hubbard) effect mediated by a weak cation–cation interaction and the lattice dimerization (Peierls distortion) [485–488]. VO_2 was first identified as a classic Peierls transition due to the formation of spin singlets associated with V–V dimers in the monoclinic phase [489]. A recent study shows that tensile strain can tune this phase transition to become purely electronic without the Peierls distortion [490]. V_2O_3, on the other hand, is a prototypical Mott–Hubbard system [491]. At HP, the formation of the cation–cation bonding is observed, similar to a 2D Peierls-like distortion, where the cation–cation dimer chains are connected along the *c*-axis of the monoclinic cell [492, 493].

4.4.3. Spin-pairing. Spin-pairing occurs when the crystal field splitting changes or electron band widens [494]. Both XES and NFS (Mössbauer effect) are sensitive to the spin state of the transition metal ions. The K_β emission line of *3d*

metal ions has a satellite in the high-spin state, which disappears in the low-spin state as illustrated in figure 26. In NFS data, the spin-pairing is identified by magnetic splitting in the hyperfine structure.

Spin crossovers of Fe at HP have significant implications in the mineralogy and dynamics of the deep earth. Following the observation of spin-pairing of Fe^{2+} in troilite (FeS) at 6.5 GPa [235] and ferropericlase (Fe, Mg)O at 60 GPa [243], spin transitions of both Fe^{2+} and Fe^{3+} have been observed in other major deep earth materials, such as bridgmanite, post-bridgmanite, and the core materials such as Fe_3S and Fe_3C (see [174] and references therein). The spin transitions in minerals affect their densities and *P-V-T* EOS [172, 173, 495], sound velocities [286, 496, 497], transport properties [498–501], and element partitioning [222, 243]. In ferropericlase, these effects have been well documented, whereas the effects of the spin transition of iron (Fe^{2+} and Fe^{3+}) in bridgmanite and post-bridgmanite are much more complex and remain debated.

In transition-metal compounds, particularly oxides, sulfides, and halides, systematics for the *d–d* Coulomb energy U and the ligand-to-metal charge transfer energy Δ are generally used for describing the band gaps and electronic structures of the compounds [502]. Pressure-induced spin pairing strongly influences both U and Δ, providing an important mechanism in the pressure induced electronic structure changes of Mott–Hubbard ($U > \Delta$) or charge-transfer ($U < \Delta$) insulators. FeS falls at the boundary between charge-transfer and Mott–Hubbard insulators with $\Delta < U$ and U relatively small. A reversible electronic transition in FeS is closely related to the structural transition from a manganese phosphide-like phase to a monoclinic phase, with no sign of metallization at the transition [503]. The XES result is consistent with the disappearance of the magnetic splitting from Mössbauer spectroscopy [504]. Late transition metal oxides (MnO, FeO, CoO) are typical Mott insulators of charge-transfer type ($U < \Delta$). Both MnO and CoO show spin-pairings at about 80 and 100 GPa, respectively [505, 506]. The spin-transition pressures are consistent with the structural changes reported for MnO around 80–90 GPa from the rB1 to the nB8 structure [505], and for CoO around 90–95 GPa from the rB1 phase to a high-density rhombohedral phase [507]. FeO remains a magnetic insulator up to 150 GPa [241]. However, when the FeO sample was laser heated at 140 GPa, clear spin paring was observed in XES data [508], consistent with the structural change from rhombohedral to B8 (NiAs-type) structure [509]. From first principle computations, the spin-pairings in late transition oxides result from band broadening due to shorter nearest neighbor distances, rather than an increase of the crystal field splitting [510].

4.4.4. Electron delocalization. Electron delocalization occurs when tightly bound, atomic-like orbitals begin to mix with orbitals on neighboring lattice sites. HP can be used to effectively tune the electronic correlations, while experimentally measuring quantum observables by x-ray probes as the correlation evolves. Light rare-earth metals exhibit pressure-driven volume collapses attributable to 4*f* electron delocalization (e.g. Ce, Pr, and Gd). Their behavior has been approached by various models [511–513], and recently by a fully dynamical treatment of correlations in the lattice using dynamical mean-field theory (DMFT) [514]. HP RXES provides detailed information on the 4*f* electron occupancy as a function of pressure. Such results can be directly compared to DMFT predictions, making a powerful connection between experiment and theory.

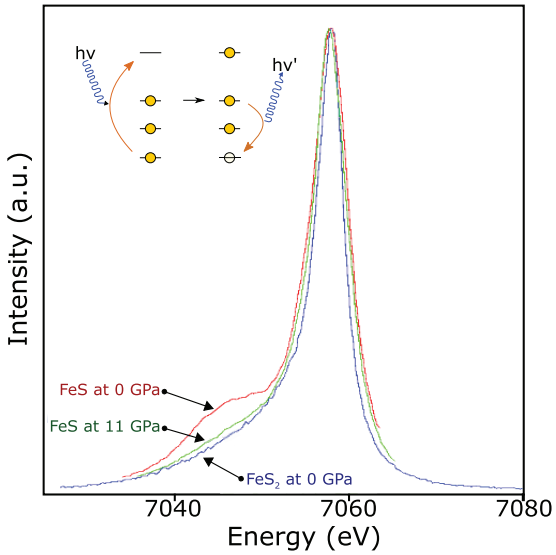

Figure 26. Iron K_β emission spectra for several iron compounds. The spin-pairing state leaves a signature as satellite, showing a high spin state of FeS at ambient pressure and low spin states of FeS_2 at ambient pressure and FeS at 11 GPa.

The development of 4*f* occupation has been measured for Pr at pressures over 30 GPa (figure 27), crossing the transition from localized and nonbonding to delocalized and bonding at 20 GPa [249]. Comparison of the results to DMFT calculations indicates a strong connection between the 4*f* electronic structure and the volume-collapse. Similarly using RXES, L_γ emission of Ce metal has been measured across the γ-α volume collapse transition [250]. The satellite peak of L_γ decreases 30% across the volume collapse, directly validating the Kondo model in conjunction with previous measurements [515]. The RXES data on Gd metal to 113 GPa also suggest Kondo-like aspects in the delocalization of 4*f* electrons [276]. However, a prolonged and continuous delocalization was observed for Gd throughout the entire pressure range, indicating that the volume-collapse transition for Gd at 59 GPa is only part of the electron delocalization. The $L_{\gamma 1}$ XES spectra indicate no apparent change in the 4*f* moment across the collapse, suggesting that Kondo screening is responsible for the expected Pauli-like behavior in magnetic susceptibility.

4.5. Phonon structure

Phonons, as delocalized and collective excitations, describe the dynamics of atomic motions in condensed matter. Phonon structure and phonon density of states are used to calculate fundamental thermodynamic quantities pertinent to lattice vibrations, including vibrational energy, vibrational entropy, specific heat capacity, and Debye temperature etc. Phonons

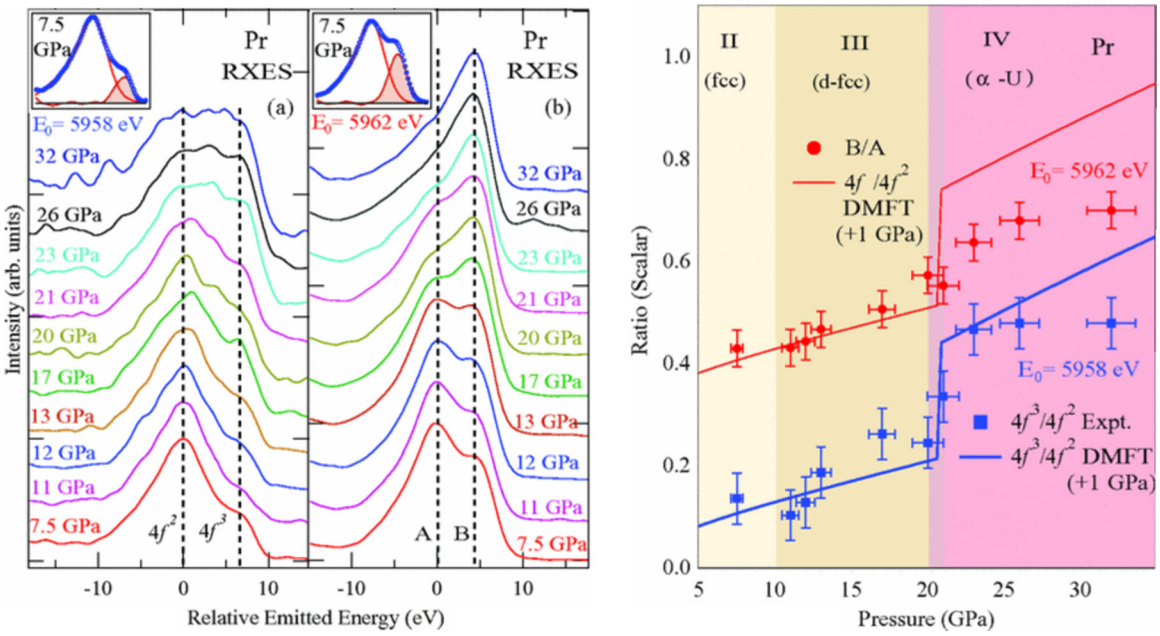

Figure 27. (left) RXES spectra for Pr at high pressures at energies of 5958 eV and 5962 eV, respectively. Data points of the ratio of the A and B features in the $E_0 = 5962$ eV data are plotted on the right. (right) Comparison of experimental and theoretical $4f^3$ to $4f^2$ occupancy ratios as a function of pressure for Pr metal. (Modified with permission from [249]. Copyright 2012 by the American Physical Society.)

are studied by optical Brillouin scattering (acoustic), Raman and IR spectroscopy. However, their dispersion throughout the Brillouin zone can only be measured by x-ray or neutron scattering (e.g. inelastic neutron scattering—INS). As shown in figure 13, IXS have a relative advantage over INS for studying collective excitations at the high energy transfer region. More importantly, due to the large sample required in INS, x-ray studies of phonons at HP become unique.

4.5.1. Phonon density of states. HP NRIXS is a primary x-ray technique used for deriving (partial) phonon density of state (DOS) at HP. Iron is a suitable Mössbauer element and has been widely used in HP NRIXS studies for pure iron, iron containing materials and minerals. Since the first x-ray results of the phonon DOS of Fe at ambient pressure [296, 297], the phonon DOS of hcp-Fe has been extended to high pressures up to 42 GPa [155], 153 GPa [63], 171 GPa [300, 516], and recently to 136 GPa using a quasi-hydrostatic medium [517]. High temperatures have been added in the phonon DOS determination for Fe at HP [298, 299]. Figure 28 shows an example of the phonon DOS of Fe at 153 GPa, together with its derived thermodynamic quantities. A number of implications may be obtained from the phonon DOS. For example, the HP data on phonon DOS suggest restricted thermal atomic motion at high compression; the volume dependence of vibrational entropy may be used to determine the product of the vibrational thermal expansion coefficient and isothermal bulk modulus [516]. From the low-energy region of each phonon DOS, Debye sound velocity can be derived.

Phonon DOS has been determined for a number of iron compounds and alloys: FeO [518, 519], FeS [520], Fe–Ni [521], Fe–Si alloys [288, 521], FeH [522], Fe_3S [523], Fe_3C [524–526], Fe_2O_3 [527], (Mg,Fe)O [496], and (Mg,Fe)SiO_3 enstatite [528]. For nanocrystalline Fe, large distortions were found in its phonon DOS [529], showing a lifetime broadening at high energies and an enhancement in its phonon DOS at energies below 15 meV.

By using both INS and NRIXS, the combined data sets provide the total phonon DOS and partial phonon DOS for elements other than Fe. For example, the determined vibrational entropy in FeV was found to increase as ordering increased [530], contrary to the behavior of common ordering alloys. Phonons in the ordered FeV phase are softer than in the solid solution; and it is likely that high temperatures may stabilize the ordered phase. In Au–Fe alloys, a stiffening of the Au partial phonon DOS was found to increase with Fe concentration, which is consistent with the first principles calculations showing a local stiffening of Au–Au bonds close to Fe atoms [531]. Crossing the pressure-induced Invar transition (vanishing thermal expansion) in Pd_3Fe, the stiffening of the partial DOS with decreasing volume was found to be slower, owing to a relative softening of the first-nearest-neighbor Fe–Pd longitudinal force constants at the Invar transition [532, 533].

HP studies on phonon DOS of elements other than Fe are relatively scarce. Some examples include Sn [534, 535], Kr [536], and Dy [537].

4.5.2. Sound velocities. In the low energy region, the phonon DOS shows Debye-like behavior, displaying a parabolic form with energy (E):

$$g(E) = \frac{M}{\rho}\frac{E^2}{2\pi^2\hbar^3 V_D^3} \tag{4.3}$$

where $g(E)$ is the phonon DOS; M is the mass of the resonant nucleus, and ρ is the mass density of the solid. The projected sound velocity V_D is Debye velocity, which can be obtained by the parabolic fitting of the low energy slope. Because the

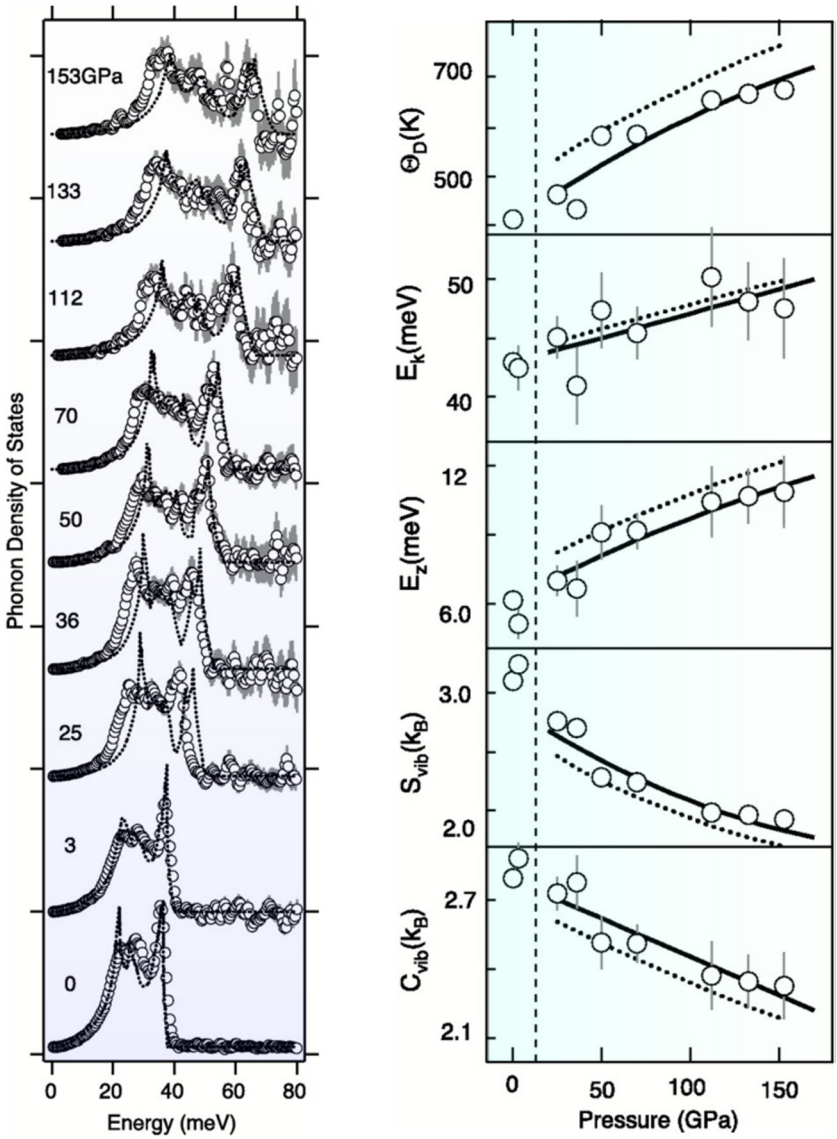

Figure 28. (left) Phonon density of states of ^{57}Fe measured by NRIXS at high pressures are shown as circles with error bars. The thin dotted curves are from *ab initio* theory. (right) Thermodynamic parameters of Fe derived from phonon density of states. Solid curves show the fit to experimental data; dotted curves are from simulations. (Modified with permission from [63]. Copyright 2001 American Association for the Advancement of Science.)

Debye velocity is related to compressional velocity (V_P) and shear velocity (V_S) by:

$$\frac{3}{V_D^3} = \frac{1}{V_P^3} + \frac{2}{V_S^3}, \tag{4.4}$$

and V_P and V_S are related bulk elastic moduli by

$$V_P^2 = \frac{4}{3}V_S^2 + \frac{K_S}{\rho} \tag{4.5}$$

$$V_S^2 = \frac{G}{\rho} \tag{4.6}$$

where K_S and G are adiabatic bulk modulus and shear modulus, respectively, both V_P and V_S can be determined by solving equations (4.4) through (4.6). Examples of sound velocity determination using NRIXS include: Fe [63, 298, 516, 517], FeO [518, 519], FeS [520], Fe–Ni [521], Fe–Si alloys [288, 521], FeH [522], Fe_3S [523], Fe_3C [524–526], Fe_2O_3 [527], and (Mg,Fe)O [496]. The Debye parabola is best constrained at the low-energy limit, and a resolution of better than 2 meV is therefore essential in NRIXS for approaching that limit. It should be noted that V_D is heavily weighted (>90%) to V_S (see equation (4.4)). Thus sound velocities determined by NRIXS are a good measure of shear velocities. However, from equation (4.5), we can see that V_P is mainly constrained by the term K_S/ρ (that is determined by other methods e.g. XRD), which may contribute to the uncertainties in V_P determination, in particular, when K_S is not well constrained at HP.

V_P can be more directly determined using HP HERIXS technique. By measuring the dispersion of longitudinal acoustic phonons, V_P can be determined by fitting the dispersion curve, assuming a dispersion relation (e.g. a sine function). This method was applied to polycrystalline iron in a DAC, and the determined V_P as a function of pressure was found to follow the Birch law [12]. V_P in a highly textured hcp-Fe sample displayed a difference of 4–5% between the two velocities at 50° and 90° from

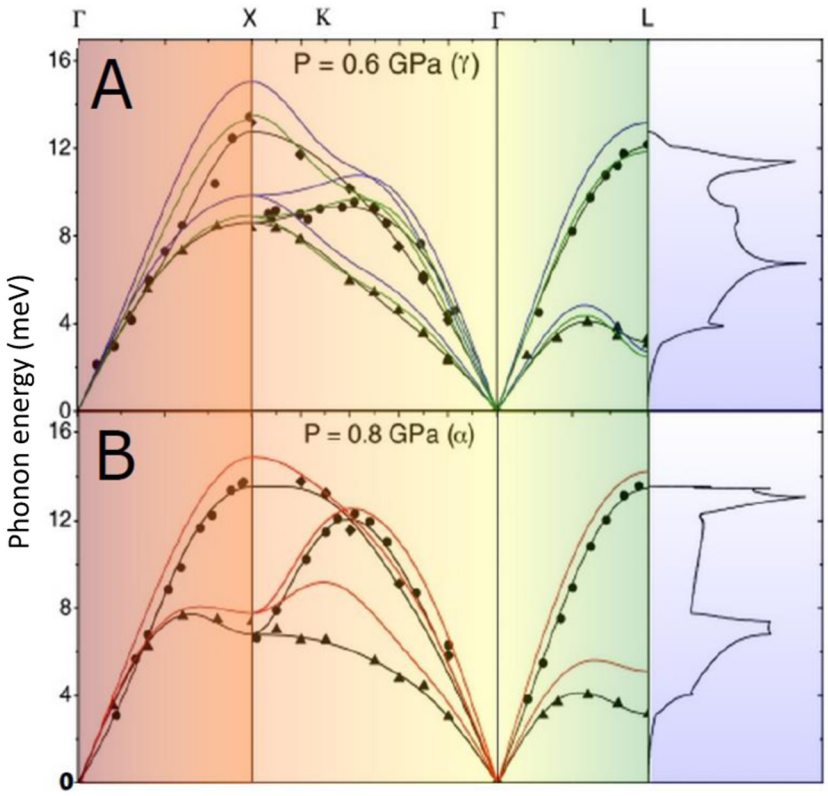

Figure 29. Phonon dispersion of cerium metal at 0.6 GPa (γ-phase) and at 0.8 GPa (α-phase) determined by inelastic x-ray scattering. LA branches (circles), $T1\langle 1\,1\,0\rangle$ branch (triangles), and $T2\langle 0\,0\,1\rangle$ branches (diamonds). The lines are the results of theoretical fit, using different potentials. (Modified with permission from [290]. Copyright 2011 National Academy of Sciences.)

the c-axis, which is of the same order of the seismic anisotropy in Earth's inner core [538, 539]. The effects of light elements on the sound velocities in iron were studied by measuring V_P in FeO, FeSi, FeS, $Fe_{0.89}Ni_{0.04}Si_{0.07}$, and FeS_2 at HP [287, 288, 540, 541]. HERIXS measurements have been recently extended to high temperatures [292–294]. These results are used to constrain the composition of the Earth's core. Besides iron, other elements can also be studied with the HERIXS technique. For instance, the longitudinal acoustic phonon dispersion in polycrystalline Co up to 99 GPa has been measured using HERIXS [542], with a softening found at around 75 GPa.

4.5.3. Phonon dynamics. Complete phonon dispersion curves may be determined by HERIXS when a single-crystal sample is kept at HP. Sample quality and the hydrostatic environment become critical factors in the measurement of phonon dispersion relations. The lattice dynamics of Mo has been successfully studied up to 37 GPa [101]. A significant decrease in the H-point phonon in Mo was observed at HP, possibly due to a decrease in the magnitude of electron–phonon coupling. The phonon dispersion relations of f-electron element, Ce, were measured at HP across the isostructural γ-α transition [290]. Clear phonon softening across the transition was found (figure 29), indicating large modifications in the phonon–electron interactions. The lattice contribution to the phase transition is reflected by the derived vibrational entropy of 0.33 k_B, compared to the total entropy change of 1.5 k_B.

Thermal diffuse scattering (TDS) has been used for obtaining information on phonon dispersion relations [543], e.g. for Si [544] and V [545], all at ambient pressure. HP applications are still limited because of the weak diffuse signals and the need for accurate background subtraction arising from surrounding materials (anvil or gasket). Nevertheless, it may be feasible to determine how TDS (hence phonon dispersions) changes with pressure if the phonon structure of materials is well determined at ambient pressure.

4.6. Mechanical properties

Materials under compression undergo deformations. If the deformations are reversible upon the removal of load, it is called elastic deformation. Permanent deformations will occur when the stress reaches a critical value (the yield point), resulting in irreversible or plastic deformations. The elastic and plastic behaviors of materials at HP are well studied using x-ray synchrotron probes.

4.6.1. Elasticity. Materials' elastic behavior is described by various elastic moduli and by elastic tensor (C_{ij}) or elastic compliances (S_{ij}). Commonly used elastic moduli include Young's modulus, shear modulus (G), and bulk modulus (K); all of which are measures of the stiffness of a material, or resistance to deformation under an applied load. These parameters are related to each other (e.g. equations (4.4)–(4.6)). There are several HP techniques available for measuring these properties (radial XRD, ultrasonic techniques, Brillouin scattering, NRIXS, and HERIXS), each with their own merits and limitations.

The compressibility of materials arises from information on specific volumes at HP, which can be obtained from XRD and x-ray nano-imaging. Compression data from XRD or imaging give isothermal bulk modulus, K_T, which is a fitting parameter to empirical EOS. The adiabatic and isothermal bulk moduli are related by $K_S = K_T(1 + \alpha\gamma T)$, where α and γ are thermal expansion coefficient and the Grüneisen parameter, respectively. Data from ultrasonic techniques, HERIXS, NRIXS, and Brillouin scattering provide adiabatic bulk modulus K_S. The $K_S - K_T$ conversion uncertainty should be considered when comparing data from different techniques. For V_P, although it can be determined by ultrasonic techniques (limited to low pressure) and optical Brillouin scattering (limited to transparent samples), a direct and accurate x-ray probe is HERIXS, as discussed in section 3.4.3. For V_S, the x-ray technique NRIXS provides a good measure on shear properties because the measured V_D from NRIXS depends heavily on V_S. Note that NRIXS only works for Mössbauer elements. For other materials, shear properties are largely determined by ultrasonic techniques [546], Brillouin scattering [547, 548], and momentum resolved IXS on single-crystal samples.

The determination of the elastic tensor requires multiple measurements to be performed on different directions on a single-crystal. For a low-symmetry crystalline sample, it requires the measurement of many different directions within the sample, thus making relatively few complete determinations of low symmetry materials. For high symmetry materials, such as cubic symmetry, C_{ij} can be determined from moduli or sound velocities plus density [93, 549]:

$$K_S = \frac{1}{3}(C_{11} + 2C_{12}) = \rho\left(V_P^2 - \frac{4}{3}V_S^2\right) \tag{4.7}$$

$$G = C_{44} = \frac{1}{2}(C_{11} - C_{12}) = \rho V_S^2 \tag{4.8}$$

4.6.2. Plasticity. Plasticity describes the deformation of a material undergoing non-reversible changes in shape, length, and volume. Unlike the elastic properties which can be considered as state variables, plastic processes are irreversible and dependent on pathways.

The origins of plastic deformations are more complex. In metals and other crystalline materials, the occurrence of plastic deformations at the micro-scale level is due to the motion of dislocations and the migration of grain boundaries on the micro-level. In granular materials, plastic flow is due to both the irreversible rearrangement of individual particles and to the irreversible crushing of individual particles. Plastic deformation is usually driven by non-hydrostatic (deviatoric) stress. Key information for determining plasticity includes a well-controlled measure of deforming stress and a measure of plastic strain, as well as the time dependence of the stress–strain relation. Using two opposing anvils, DAC naturally generates uniaxial stress. On the basis of anisotropic linear elasticity theory [550], the deviatoric stress (t) in DAC may be expressed by:

$$t = \sigma_1 - \sigma_3 = 6G\langle Q(hkl)\rangle \tag{4.9}$$

where σ_1 and σ_3 are the stress components along and perpendicular to the loading axis, respectively. $\langle Q(hkl)\rangle$ denotes the average of all $Q(hkl)$ which can be obtained from strain ε_{hkl} measurements as a function of ϕ, the angle between the loading axis and the momentum transfer, using the radial XRD technique:

$$\varepsilon_{hkl} = (1 - 3\cos^2\phi)Q(hkl). \tag{4.10}$$

Note that the t in equation (4.9) is also related to the shear property G [62, 551]. In a data evaluation of MgO, it has been observed that plastic deformation effects a change in the stress field for subpopulations of grains, which represents different crystallographic orientations with respect to the applied stress field [552]. Quantitative measurement of deviatoric stress in the DAC remains a challenging task, partly because pressure generation and uniaxial stress are coupled in the DAC. A device called 'deformation-DIA' has been developed [210, 553], which allows independent control of the differential stress and deformation strain under a certain confining pressure. Alternatively, a rotational Drickamer apparatus has been used for additional torsion through anvil rotation under a confining pressure [554]. In these devices, strains of samples are measured by x-ray radiography. Differential stress can be estimated according to linear elasticity theory [551, 555, 556].

Materials under uniaxial stress develop preferred lattice orientation (or texture) which has a profound effect on the anisotropy of physical properties. Preferred orientation develops during dislocation glide which can be used to infer deformation mechanisms [91, 308, 493, 557]. Radial XRD offers a good measure of lattice preferred orientation. In the case of a polycrystalline sample, the intensity recorded at a certain sample orientation is proportional to the volume fraction of crystallites with their lattice planes in reflection geometry. This is often represented by the pole figure, a 2D projection of the 3D preferred orientation distribution (figure 30). With the orientation distribution information, we can calculate polycrystal physical properties based on our knowledge of single-crystal physical properties (e.g. see a review article [558] and references therein). Pole figure analysis also provides important information in understanding the mechanisms of texture, such as the dislocation glide during deformation [90, 558–560], dislocation mechanism of nanomaterials [308, 492], recrystallization (e.g. [561]), grain boundary effect (e.g. [562]), and inherited textures through phase transformations (e.g. [563]).

4.6.3. Strength. The strength of a material is the ability to withstand an applied load without failure. Here, the 'failure' may be referred to as either the beginning of plastic deformation (i.e. yield strength) or complete failure, in the manner of ductile failure or brittle failure (i.e. compressive strength).

By determining the radial distribution of pressure in a DAC and assuming that the pressure gradient is supported by the sample's strength [67], the strength of materials has been estimated based on the equation of force balance [564–567]. Using radial XRD, the deviatoric stress t is determined according to linear elasticity theory, which is then used to represent the strength of materials at HP [45, 329, 568–570]. In most cases,

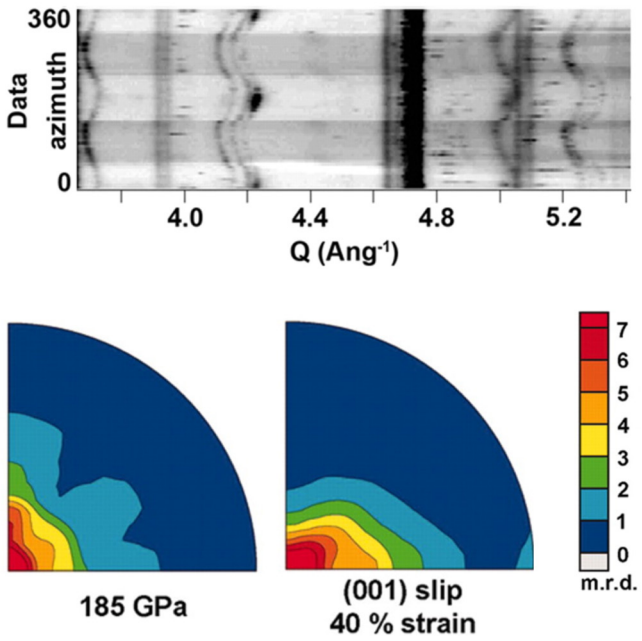

Figure 30. (top) Diffraction image of $MgSiO_3$ post-bridgmanite at 185 GPa, with evident texture as systematic intensity variations along diffraction peaks. (bottom) Inverse pole figures of $MgSiO_3$ post-bridgmanite at 185 GPa, compared with simulation results for dominant slip on (0 0 1) and 40% compressive strain, imply a slip mechanism along (0 0 1) planes. (Modified with permission from [90]. Copyright 2010 American Association for the Advancement of Science.)

because materials under DAC uniaxial stress undergo plastic deformation, the determined strength is usually a measure of compressive strength, but not yield strength. In particular, the plastic deformation of the sample may result in the reduction of the crystallite size and sample thickness, leading to strengthening due to grain size and work hardening. Thus, the strength determined from radial XRD could be significantly larger than the yield strength. For instance, the multifold increased strength of Re under pressure cannot be explained by shear-modulus scaling alone. Work hardening effect appears to be the dominant factor leading to strengthening of Re under pressure [569].

If a relationship between deviatoric stress and strain is determined, the yield point can be detected by examining the derivative of the curve [571]. Information on deviatoric stress as a function of time allows us to locate the yield point of the material and thus obtain yield strength (e.g. [572]). The yield strength of some mantle minerals at HP-HT has been determined [572–576].

4.7. New chemistry, new materials

Pressure is a fertile dimension for new chemistry and new compounds through an interplay of atomic (molecular) and electronic interactions. Many recent discoveries of novel bonding and material structures at HP indicate that our conventional descriptions of atomic and electron behaviors are no longer adequate under pressure. The Periodic Table at HP is very different from the one at ambient pressure. New 'rules' of chemistry emerge [21, 473, 577–579] at extreme conditions.

4.7.1. High pressure chemistry. Because the compression energy ($P\Delta V$) can be comparable to or even exceed chemical bonding energy (~eV), observation of novel chemistry at HP is the norm [21, 578]. The question becomes what new 'rules' govern chemical bonding, structure, and reactivity at HP? Electron distributions at HP tend to be more delocalized, resulting in a tremendous richness in HP chemistry, including complex phase diagrams of 'simple' metals [345, 480], new forms of matter [151, 200], novel intermetallic compounds [99, 462], unexpected stoichiometry [195, 580, 581], and new noble gas chemistry [457, 582, 583]. For example, the valence state is usually derived from interatomic distances and the coordination number via bond valence sum rules [584]. At HP, the same rules no longer apply. By combining XAS, NFS, and XRD, the valence state of Eu atoms in EuO has been measured to 90 GPa [16]. Eu atoms display a mixed-valence state composed of discrete Eu^{2+} and Eu^{3+}, with an increasing averaged-valence as pressure is increased (figure 31). Unexpectedly at higher pressures, along with the NaCl → CsCl transition, a reentrant Eu transition into a lower valence state (nearly Eu^{2+}) becomes obvious from both the XANES and NFS measurements.

In addition to inducing complex structural and electronic transformations, compression drives unexpected chemical reactivity. Methane has been synthesized from wüstite, calcite and water at HP [585], demonstrating abiogenic pathways for the formation of hydrocarbons in the Earth's deep interior at 200–300 km depth beneath the surface. In nitrogen chemistry, applying pressure induces bonding changes [586, 587], amorphization [588], changes in quencheability [74, 589], metallization [590], and novel structures [392, 591–598]. Many exotic nitrides have been synthesized under HP [22, 599–603], including new durable noble Ir, Pt, and Os metal nitrides synthesized at HP coupled with laser heating [603–606]. These new compounds have bulk moduli comparable to those of traditional superhard materials. In alkali and alkaline metals, because the energies of the *s* orbitals increase more rapidly with pressure than the energies of the *d* orbitals, pressure induced hybridization, such as *s*-to-*d* transfer, is widely observed [607]. For instance, at ambient pressure, no compounds can be formed between the alkali metals (except lithium) and the transition metals to the left of gold in the Periodic Table [608], because the formation of transition metal alloys is favored between two metals with small differences in electron charge density (Miedema rules [609, 610]). As *s*-to-*d* transfer occurs under HP, charge density of the alkali metals increases significantly, allowing alloy formation with transition elements. Several compounds have been reported to form under pressure between K and Ni [99, 610] and Ag [611, 612]. Recently, a novel Rb–Pt alloy at pressures above 17 GPa has been successfully synthesized [613]. The pressure-induced *s*-to-*d* electronic transition in Rb was monitored experimentally *in situ* by means of XANES at the Rb *K*-edge at HP. The alloying process with Pt in the pressure range of 17–23 GPa was revealed by both XANES and XRD, indicating that the synthesis started with the *s*-to-*d* electronic transition in Rb, followed by the compound formation of Rb–Pt at higher pressures. In *f*-electron metals, two very dissimilar elements in atomic size and electronegativity, Ce and Al, form a substitutive alloy [58,

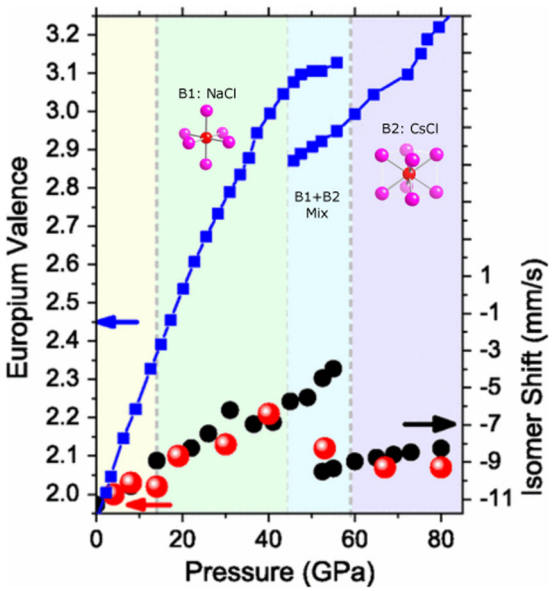

Figure 31. Europium valence determined by x-ray absorption (XANES, red-circles) and nuclear forward scattering (NFS, black circles) techniques. Both the XANES and the NFS results are in good agreement but in stark difference to the bond-valence parametrization method (blue squares) results. (Modified with permission from [16]. Copyright 2012 by the American Physical Society.)

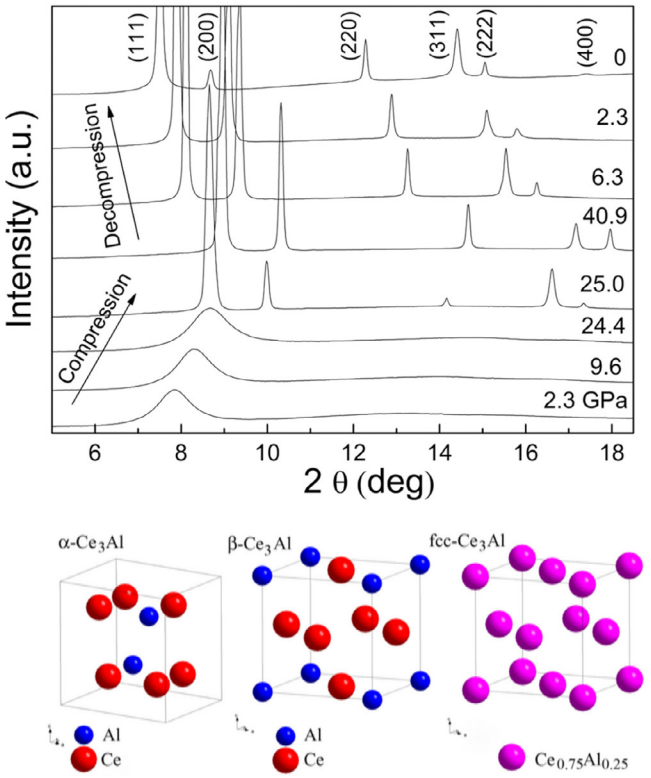

Figure 32. (top) A metallic glass in Ce_3Al composition crystallizes into an alloy with a FCC structure under compression above 25 GPa. The alloy persists when the pressure is released. (bottom) Crystal structures of the two ordered compounds, α-Ce_3Al and β-Ce_3Al, and the new disordered fcc-Ce_3Al alloy with diminishing size differences. (Modified with permission from [58]. Copyright 2009 National Academy of Sciences.)

200, 216], largely due to the Kondo volume collapse of Ce 4*f* electrons at HP greatly reducing its difference to Al (figure 32). Once formed, the alloy persists when the pressure is released.

In material synthesis, pressure adds a new dimension in creating exotic alloys and properties [614–618]. The formation of extended solids (polymers) is a common observation under HP, e.g. polymeric cg-N [586, 619]. Polymerization of formic acid is observed under HP [453]. A new polymeric form of silicon (Si_{24}) has also been synthesized with a quasi-direct band gap that falls within the desired range for solar absorption [581]. Unlike the conventional diamond structure, this new allotrope consists of an interesting zeolite-type structure, which is comprised of channels with five-, six-and eight-membered silicon rings. Another interesting example of unprecedented reactivity and bonding is the reactivity of xenon at HP, forming novel xenon–hydrogen compounds [100, 583]. Mixtures of Xe–H_2 at modest pressures (4.9, 5.4 GPa) were found to sequentially form high-hydrogen content xenon complexes $Xe(H_2)_7$ and $Xe(H_2)_8$ with intact H_2 groups (figure 33). The fact that pressure induces reactivity in xenon may not come as a surprise, considering that xenon is known to become metallic at HP. However, what is surprising is that a number of unexpected compounds dissimilar to those synthesized at ambient pressures are synthesized at HP and some of them are retrieved at ambient pressure on pressure release. These discoveries reveal the possibility of synthesizing a whole new class of compounds that have unexpected electronic properties due to xenon. The structures contain an exceptionally large molar equivalent of bound hydrogen, important for potential hydrogen storage applications [620].

4.7.2. Photochemistry. Ionizing radiation (UV to x-rays) can produce free radicals in irradiated solids, and the products of irradiation can often be preserved at cryogenic temperatures [621]. Irradiating samples with x-rays may induce ionization into fragmented ions and thus promote chemical reactions, enabling an otherwise inaccessible reaction pathway because the ionization barrier is often too big for thermal excitation or visible-to-IR lasers. Soft x-ray and UV is unusable at HP because it is completely blocked by the anvils or gasket. Irradiation with hard x-rays, in the region of 5–12 keV, not only provides penetrating power but also a sufficient absorption cross section to induce ionization, becoming a powerful technique to study irradiation chemistry at HP. The bond in molecules (e.g. O_2, N_2, CO_2, H_2O) can be broken by x-ray photons of tens of eV [622–624]. Some reaction products may be thermodynamically stable at ambient pressure.

For example, water (H_2O) molecules ionized and subsequently formed O–O and H–H bonds, resulting in a molecular alloy of O_2 and H_2 [457] (figure 34). The formed crystalline solid remained stable with respect to variations in pressure and temperature, and further x-ray and laser exposure. It differs from previously known phases. Similarly when irradiating a mixture of liquid N_2 and O_2, the strong covalent bonding of the molecules is broken down, forming ionic compounds of complex nitrogen oxide ions [582]. Nitrogen and oxygen do not react with each other at room temperature due to the large covalent bond energy of the molecules. Irradiating a liquid mixture of O_2 and N_2, contained in a DAC under pressure with a 10.2 keV synchrotron radiation, caused dissociation

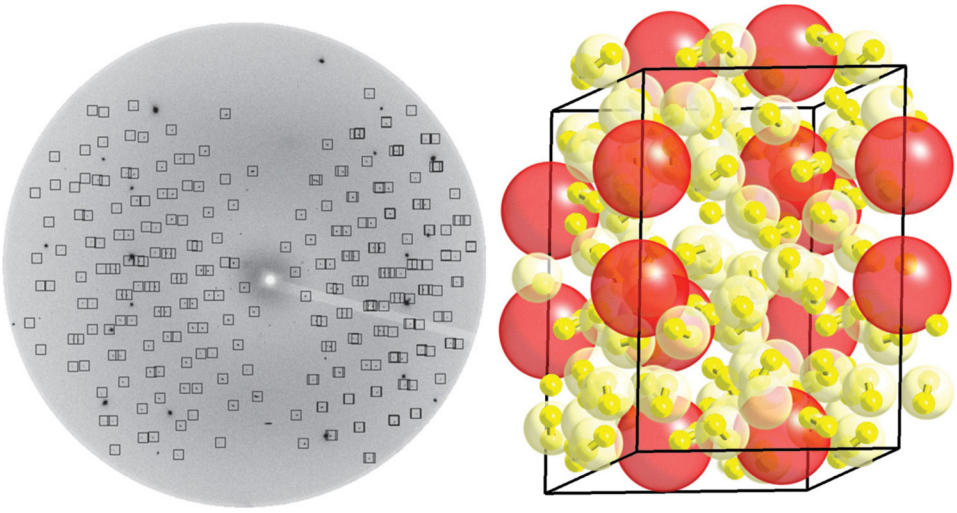

Figure 33. (left) X-ray single-crystal diffraction of Xe–H_2 compound at 4.9 GPa. A total of 201 reflections could be indexed on a hexagonal unit cell. (right) Model structure of $Xe(H_2)_7$. The xenon atoms are surrounded by dumbbell-shaped hydrogen molecules. (Modified with permission from [100]. Copyright 2010 Macmillan Publishers Limited.)

of O_2 and N_2 molecules and induced a chemical reaction to form $NO_2^+NO_3^-$, an ionic phase of N_2O_5 [582]. In a study of the x-ray induced decomposition of $KClO_3$ and KIO_3 [625], the decomposition rate is found to be energy dependent, with an apparent resonance near 15 keV, maximizing the chemical decomposition rate. The resonance is likely related to the O–O distance in x-ray induced reactions. Irradiation chemistry at HP is widely used for studying the optimal pathways of hydrogen synthesis [626], gas-loading [627, 628], and synthesizing new compounds [629–631].

4.7.3. Superconductors. The superconductivity of a large number of elements and compounds including cuprates [632, 633], fullerides [634], intermetallic boron carbides [635], layered nitrides [636], magnesium diboride [637], iron pnictides [638], and recently hydrides [639, 640], can be strongly altered and tuned by pressure [641, 642]. Many elements, although not superconducting at ambient pressure, become superconductors at HP. The record high T_c (25 K) for elements has been observed in Ca at 161 GPa [643]. The search for new superconducting materials with high T_c was motivated by the discovery of superconductivity in cuprate in 1986 [632]. Soon after, a large positive pressure coefficient of T_c was detected, leading to an even higher T_c for cuprates up to liquid nitrogen temperatures [632]. The record high T_c in cuprates high-T_c superconductors has been further driven to 164 K under HP [644].

Superconductivity and magnetism are considered to be in competition with each other. In the iron-based high-T_c superconductors, however, the origin of superconductivity is closely related to the magnetism of iron. By combining NFS and XRD, magnetic and structural transitions of the parent compound of iron-based superconductors $BaFe_2As_2$ have been studied under HP and low T conditions [645]. It is found that the magnetic ordering transition precedes the structural transition in $BaFe_2As_2$. The pressure-decoupled effect is quite different from the results by chemical-doping, where structural transitions always precede or coincide with magnetic transitions.

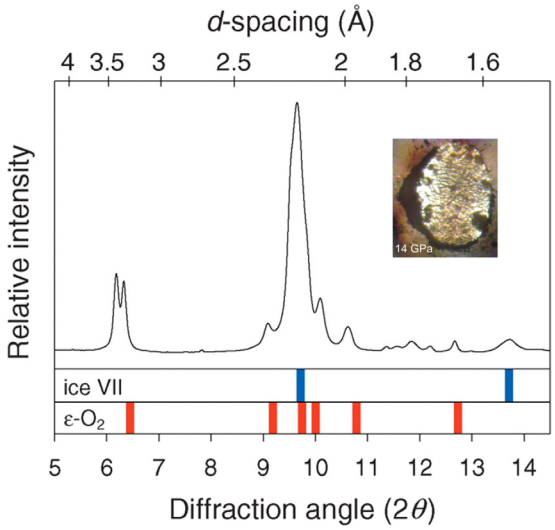

Figure 34. X-ray-induced dissociation of H_2O and the formation of an O_2–H_2 alloy. Sharp powder diffraction rings indicate that the alloy is a well-crystallized solid. Its diffraction pattern shows some similarity, but does not exactly fit, to ε-O_2. The inset is a photograph of the sample after x-ray exposure at 15.3 GPa. (Modified with permission from [457]. Copyright 2006 American Association for the Advancement of Science.)

Superconductivity is closely related to crystallographic structure, electronic charge, and orbital and spin degrees of freedom. These can all be altered by pressure, temperature, magnetic field and chemical doping. Pressure is very useful in elucidating mechanisms of superconductivity as well as the search for new high-T_c superconducting materials. The physical understanding of the pressure effects on superconductivity is related to all parameters of the phonon and electron systems, as well as their interactions. Information from x-ray probes greatly enhances our understanding of these materials by probing their structure (XRD), spin (XES), magnetic properties (NFS), electron excitations (RIXS, XANES), and phonons (NRIXS, HERIXS).

Superconductors may display a positive pressure coefficient of T_c. Pressure-tuned T_c often reaches a maximum

value and then drops monotonically at higher pressures [579, 646]. In a recent study on iron chalcogenides [647], a second superconducting phase suddenly reemerges above 11.5 GPa, after the T_c drops from the first maximum of 32 K at 1 GPa (figure 35). The T_c of the re-emerging superconducting phase is higher than the first maximum, reaching 48.0–48.7 K. Interestingly, XRD experiments show that the basic structure of these compounds was not changed in this pressure range. Therefore, the re-emergence of superconductivity with higher T_c reflects detailed structural variances within the basic unit cell. The two superconducting domes were likely the result of different charge carriers. The two-step enhancement of T_c is also found in trilayer $Bi_2Sr_2Ca_2Cu_3O_{10+\delta}$ (Bi2223) [648]. In a rare-earth-doped $Ca_{0.86}Pr_{0.14}Fe_2As_2$ single-crystalline sample, the electrical resistance measurements using a designer DAC show an intriguing observation of superconductivity under pressure, with T_c as high as ~51 K at 1.9 GPa [649].

4.7.4. Superhard materials. Hardness is a measure of the resistance of solids to deformation and is characterized by indenting a material using a hard indenter. Materials with Vickers hardness larger than 40 GPa are generally referred as superhard materials. These materials may be empirically related to high bulk modulus [650] and high shear modulus [599]. Strengthening due to grain size and nanotwinned structures also contributes to super hardness [651, 652], resulting in hardness higher than that of single-crystal diamond [652].

Microscopically, hardness can be defined as the combined resistance of chemical bonds in a crystal to indentation, with the determining factors of superhard materials being high bond strength, short bond distance, and high valence electron density (e.g. [653, 654]). These factors can all be enhanced at HP, making HP a common route for synthesizing and studying superhard materials. *In situ* x-ray probes can be used to study the bonding (IXS), structure and atomic distance (XRD), and electron density distribution (single-crystal XRD), and have been widely used in the quest for superhard materials [38, 655–658].

In general, superhard materials are all covalent and polar covalent solids. The major types of superhard materials are the B–C–N–O compounds with characteristics of short and strong 3D covalent bonds. Diamond, the hardest known substance until recently [652], is a well-known carbon form that can be synthesized from graphite at HP conditions [659]. When graphite is compressed under ambient temperature, x-ray IXS experiments showed that it undergoes a transition at 17 GPa, where half of the π-bonds between graphite layers convert to σ-bonds, whereas the other half remain as π-bonds in the HP form [72]. The HP form has a distorted M-carbon structure [660] and is super hard, capable of indenting cubic-diamond single crystals. Similarly, compressing fullerenes causes crushed C_{60} cages, forming superhard forms of carbon that are quenchable to ambient pressure [421, 661]. Individual C_{60} molecules are estimated to have an extremely high elastic modulus of 800–900 GPa [662]. High hardness and high plasticity have been observed for 3D-polymerized C_{60}-based materials [663–665]. When a glassy carbon, composing of disordered graphene layers, is compressed to 40 GPa, a new carbon form has been observed with a fully σ-bonded amorphous

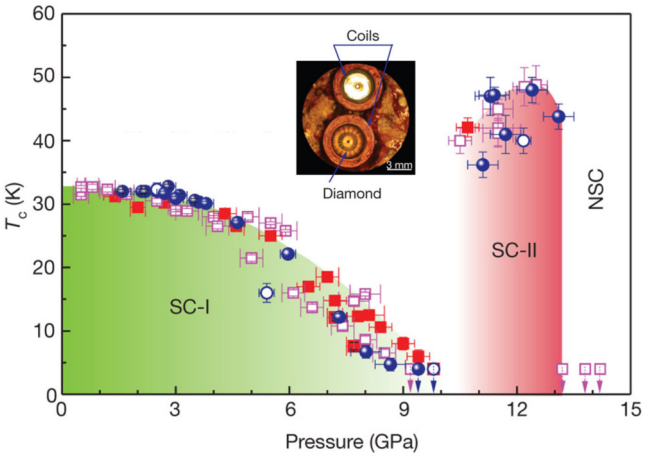

Figure 35. Pressure dependence of T_c for the iron-based superconductors, showing the re-appearance of superconductivity at high pressure. The symbols represent the pressure–temperature conditions for which T_c values were observed for four different samples from the resistive and alternating-current susceptibility measurements. Two superconducting regions (SC-I and SC-II) are separated by a critical pressure at around 10 GPa. NSC: the non-superconducting region above 13.2 GPa. The inset is the setup for susceptibility measurements in DACs, with a signal coil and a compensating coil. (Modified with permission from [647]. Copyright 2012 Royal Society of Chemistry.)

structure [261]. The HP glassy form is capable of holding a large stress difference of >70 GPa, indicating the high hardness of this HP carbon allotrope. Adding boron into carbon, a cubic diamond-like BC_5 phase has been synthesized at 24 GPa and about 2200 K [666], which exhibits extreme Vickers hardness (71 GPa) and high thermal stability (up to 1900 K). Light element compounds in the B–C–N–O system are the most appealing materials for novel superhard materials; inspiring extensive studies e.g. [22, 654, 667–669].

Another type includes the compounds formed by light elements (B, C, and N) and heavy transition metals (e.g. [670]). The metals of high valence electron density provide high incompressibility, while light elements enable directional covalent bonds to form. However, in transition metal compounds the enhancement effect from valence electrons is largely offset by the large bond length. For example, ReB_2 is reported to have an average hardness of 48 GPa [671]. Radial diffraction indicates that ReB_2 is able to support a remarkably high differential stress. In OsB_2, the axis compressibility in the orthorhombic *c*-direction is less than the axis compressibility found in diamond [672]. Transition metal nitrides (e.g. PtN, PtN_2, IrN_2, OsN_2) are found to have bulk moduli comparable with those of the traditional superhard materials [605, 606]. For IrN2, the measured bulk modulus ($K0 = 428(12)$ GPa) is second only to that of diamond ($K0 = 440$ GPa).

It should be noted that super hardness can be enhanced via nanotwinning and grain size effect. Recently, nanotwinned diamond and nanotwinned cubic boron nitride have displayed unprecedented hardness and stability [651, 652]. Bulk nanocrystalline diamonds and cubic boron nitrides have been synthesized under HP conditions with an enhanced hardness of 140 GPa [38] and 85 GPa [673], respectively.

4.7.5. Energy materials. Energy materials include those with properties for energy production, storage, conversion, and transfer, those used in energy technology with excellent thermomechanical, chemical, and radiation performance, and electromagnetic extreme environments with minimal fatigue, corrosion, and degradation over time. HP studies not only provide an important route towards discovering new materials with exceptional properties, but also the fundamental knowledge of understanding the performance of these materials.

Many potential hydrogen storage materials have been studied under pressure (see a recent review [674] and references therein) and belong to four major classes; simple hydride, complex hydride, chemical hydride and hydrogen containing materials. The highest hydrogen content in a compound is that of the van der Waals compound $(H_2)_4CH_4$ discovered at HP [675, 676] with 92.3% (atomic) and 50% (weight) hydrogen. Two hydrogen hydrates $H_2(H_2O)$ and $H_2(H_2O)_6$ were first discovered at 2 GPa [677]. In an attempt to recover the hydrate at low temperature, a new $H_2(H_2O)_2$ clathrate was discovered at 0.2 GPa and recovered at ambient pressure well above liquid nitrogen temperature [678, 679]. The application of pressure successfully yielded even more hydrogen in many hydrogen-rich compounds, such as ammonia borane [680] and SiH_4 [620].

Transport processes in materials, such as ion diffusion and polaron hopping in many cathode materials for Li-ion batteries, usually involve a kinetic step. The activation volume, which may be measured by HP NFS, sets the pressure dependence of the transport process. For example, HP NFS studies provide information on the valence fluctuations of Fe [681–683] in iron-containing compounds. The application of pressure reveals the activation volume of the polaron hopping in $Li_{0.6}FePO_4$ to be large and positive [684]. The motion of the electron polaron strongly correlates with the motion of Li^+ ions, suppressing polaron hopping and making it sensitive to lattice defects.

4.8. Earth and planetary sciences

The bulk of Earth and other planets are hidden within their deep interiors under HP-HT conditions. The behavior of these materials at HP-HT provides crucial information for understanding the formation, evolution, and present state of the planets. HP experimentation becomes an important component in mineral sciences, and relates to a rich array of large-scale processes and phenomena observed by geophysical, geodynamical, and geochemical studies. For example: the fate of deeply subducted slabs, the origin of plumes, the nature of the core-mantle boundary, the differentiation of materials to form the present-day crust, mantle, and core, the distribution of trace elements, and the uptake and recycling of volatiles throughout planetary histories.

The experimental geophysics of the Earth and planetary interiors have been studied extensively with various x-ray techniques, as summarized in numerous review articles [3, 6, 685, 686]. Specific HP investigations of mineral physical properties include: XRD methods for HP mineral structures [165]; synchrotron x-ray Raman scattering for the analysis of bonding, electronic and magnetic properties of earth materials [31, 174, 382, 510]; synchrotron NRIXS for phonon and Mössbauer effects [687]; and synchrotron x-ray methods for elastic and rheological properties [247, 688–690].

5. Future perspectives

After the pioneering integration of HP and synchrotron x-ray techniques in the 1990s, and the symbiotic development, consolidation, and exploitation in the past decade, how does the next decade look like? Obviously, we are facing numerous exciting opportunities for x-ray studies at HP, including vast improvements in x-ray beam properties, novel HP technologies, advanced x-ray optics, detectors, and theory. A new era is likely to emerge in HP-SR science, one that revolutionarily redefines the scope of HP research and promises an in-depth understanding of matter under extreme conditions across the entire hierarchy of length and time scales.

As in the past with the arrival of the third generation synchrotron facilities, new breakthroughs will emerge with the development of new x-ray sources. A new avenue for creating high brightness x-ray beams has been adopted in several storage ring based synchrotron sources worldwide, based on the use of multi-bend achromat (MBA) magnet lattices [691, 692]. With the new MBA, the emittance in horizontal direction will be significantly reduced, resulting in a 'round' x-ray beam ideal for developing powerful new capabilities for HP research. Together with the use of advanced undulators and x-ray focusing optics, the MBA upgrade will provide an increase of 2–3 orders of magnitude in brightness and coherence at high energy [693]. The low emittance and high brightness will dramatically improve the ability to study smaller samples and faster processes with greater precision and accuracy. The exceptionally high coherence fraction will allow new coherence based x-ray imaging techniques to be developed for 3D morphology and strain distributions of HP samples, and for studies of the slow dynamics of various equilibrium and non-equilibrium processes at HP. Ultrahigh pressure frontiers will be extensively explored using ever smaller x-ray beams to reduce stress gradients at multi-megabar pressures. DACs are currently capable of obtaining pressures in excess of 400 GPa. With particular anvil geometry including the double stage arrangement [48, 50], there is currently an international effort to extend the pressure range to 1 TPa and beyond. The extended pressure range will revolutionarily redefine the scope of HP research.

The vast scope will greatly benefit from the advanced x-ray probes that will have orders of magnitude improvements in both spatial and temporal resolution in HP experiments. These advances will significantly enhance the precision and accuracy of HP measurements, in particular at megabar pressures. We will have an in-depth understanding of matter under more extreme conditions, such as precisely defining phase relations at megabar pressures, accurately determining *P*-*V*-*T*-structure relations at megabar pressures and at $T > 6000$ K, measuring melting curves of materials beyond 300 GPa, addressing polyamorphism in liquids at extreme conditions, detailing

chemical reactions at megabar pressures, and establishing 'new rules' in chemistry at megabars.

An important aspect from the increase in photon brightness is the enhancement of time resolved x-ray capabilities from currently ms level to ns level. This can be further improved to 100 fs level with the free electron laser (FEL) sources, with peak brightness about 10^9 times higher than the existing storage ring sources. Coupled with the advancement in rapid compression (or decompression) and modulated heating (or cooling), the enhanced time resolution will broadly address materials' dynamic processes and properties, including:

- transformation pathways—nucleation, growth and metastable or intermediate phases,
- stress relaxation, plasticity, and rheological properties at megabar pressures,
- non-equilibrium transformations, e.g. super-heating/cooling, over-/under-pressurization,
- material dynamics that occur during material synthesis (e.g. nucleation, growth) or during material failure (e.g. under stress and radiation),
- microstructure interactions and evolution, and
- incomplete transformations, phase hysteresis, retained phases.

The great improvement of x-ray spatial resolution below μm toward nm level couples well with the extreme HP that is accomplished on ever smaller sample size. Focused incident x-ray beam below 100 nm enables diffraction, spectroscopy, and imaging studies of submicron samples at multimegabar pressures [694]. Perhaps the biggest changes will come from the advanced capabilities of nm spatial resolution to examine *in situ* the hierarchical structures from the electron level to the macroscopic level, and study how they change in time and in response to external *P-T* conditions. Modeling the properties of polycrystalline components is a complex multiple length scale problem. Grains are characterized by their crystallographic orientation and boundary topology. Individual grains and boundaries have anisotropic properties but are constrained by their neighborhood until damage occurs. It is therefore crucial to observe the individual states of grains and boundaries before macroscopic averaging to reveal underlying physical principles. The sub-micron x-ray probes will provide crystallographic information on single grains of powder samples for detailed crystallographic data at ultrahigh pressures including structure refinement, thermal parameters, detail atomic positions, and even electron density topology. Bonding and electronic dynamics at megabar pressures will be studied using IXS and XRS techniques. Meanwhile, the nanometer spatial resolution will allow for studies of materials microstructures and grain-boundaries using various x-ray imaging techniques including diffraction contrast, phase contrast, and coherent diffraction imaging. Property specific 3D images, such as composition, phase, valence, magnetic, strain, and shape, will be mapped for materials in response to extreme *P-T* conditions and time. Frontier research areas will emerge for studying matter under extreme conditions, such as:

- effects of inhomogeneities on antiferromagnetic order and superconductivity in high-T_c superconductors,
- electronic origins of materials behavior and performance,
- pressure induced band gap engineering via precursors, intermediates and metastable phases,
- lattice defects, domains, and their transport in materials and condensed matter systems, and
- materials strength and plasticity by measuring the evolution of local orientations and sub-grain strains within deformed materials.

Acknowledgment

We thank Samuel Pan for his assistance in producing the figures, Rui Li for figures 10 and 11, Eric Rod for figure 12, Daijo Ikuta for figure 20, Yoshio Kono for figure 17, Yuming Xiao and Paul Chow for figure 15, and Stanislav Sinogeikin, Jesse Smith, and Ligang Bai for figures 5, 6 and 23. Comments from Freyja O'Toole and two anonymous reviewers improved the manuscript. GS acknowledges the support of the US Department of Energy grants (No. DE-FG02-99ER45775 and No. DE-NA0001974). HKM acknowledges the support of the US National Science Foundation grants (EAR-1345112 and EAR-1447438) and Natural Science Foundation of China Grant No. U1530402. HPCAT operations are supported by DOE-NNSA under Award No. DE-NA0001974 and DOE-BES under Award No. DE-FG02-99ER45775, with partial instrumentation funding by NSF. The Advanced Photon Source is a US Department of Energy (DOE) Office of Science User Facility operated for the DOE Office of Science by Argonne National Laboratory under Contract No. DE-AC02-06CH11357.

References

[1] Hemley R J 2000 Effects of high pressure on molecules *Annu. Rev. Phys. Chem.* **51** 763–800
[2] Mao H K and Hemley R J 1998 New windows on the Earth's deep interior *Ultra High Pressure Mineralogy—Physics and Chemistry of the Earth's Deep Interior* (*Reviews in Mineralogy* vol 37) ed R J Hemley (Washington, DC: Mineralogical Society of America) pp 1–28
[3] Duffy T S 2005 Synchrotron facilities and the study of the Earth's deep interior *Rep. Prog. Phys.* **68** 1811–59
[4] Bassett W A and Brown G E 1990 Synchrotron radiation: applications in the earth sciences *Annu. Rev. Earth Planet. Sci.* **18** 387–447
[5] Hemley R J, Mao H K and Struzhkin V V 2005 Synchrotron radiation and high pressure: new light on materials under extreme conditions *J. Synchrotron Radiat.* **12** 135–54
[6] Shen G and Wang Y 2014 High-pressure apparatus integrated with synchrotron radiation *Rev. Mineral. Geochem.* **78** 745–77
[7] Mao H K and Bell P M 1978 High-pressure physics: sustained static generation to 1.36–1.72 megabars *Science* **200** 1145–7
[8] Kawashima Y *et al* 2013 Monitoring system for a synthesizer at spring-8 synchrotron radiation facility and obtained results *Nucl. Instrum. Methods* A **701** 243–8
[9] Emery L and Borland M 2000 Progress towards top-up mode operations at the advanced photon source *AIP Conf. Proc.* **521** 409–14

[10] Mao H-K *et al* 2001 Inelastic x-ray scattering at ultrahigh pressures *J. Phys.: Cond. Mat.* **13** 7847
[11] Rueff J-P 2010 An introduction to inelastic x-ray scattering *Magnetism and Synchrotron Radiation Springer Proceedings in Physics* ed E Beaurepaire *et al* (Berlin: Springer) p 263 ch 9
[12] Fiquet G *et al* 2001 Sound velocities in iron to 110 gigapascals *Science* **291** 468–71
[13] Luo S N *et al* 2012 Gas gun shock experiments with single-pulse x-ray phase contrast imaging and diffraction at the advanced photon source *Rev. Sci. Instrum.* **83** 073903
[14] Jensen B J *et al* 2012 Ultrafast, high resolution, phase contrast imaging of impact response with synchrotron radiation *AIP Adv.* **2** 012170
[15] Haskel D *et al* 2011 Stability of the ferromagnetic ground state of La_2MnNiO_6 against large compressive stress *Phys. Rev.* B **84** 100403
[16] Souza-Neto N M *et al* 2012 Reentrant valence transition in EuO at high pressures: beyond the bond-valence model *Phys. Rev. Lett.* **109** 026403
[17] Pfeifer M A *et al* 2006 Three-dimensional mapping of a deformation field inside a nanocrystal *Nature* **442** 63–6
[18] Le Bolloch D, Itie J P, Polian A and Ravy S 2009 Combining high pressure and coherent diffraction: a first feasibility test *High Press. Res.* **29** 635–8
[19] Yang W *et al* 2013 Coherent diffraction imaging of nanoscale strain evolution in a single crystal under high pressure *Nat. Commun.* **4** 1680
[20] Ashcroft N W 2009 Condensed-matter physics: pressure for change in metals *Nature* **458** 158–9
[21] McMillan P F 2006 Chemistry at high pressure *Chem. Soc. Rev.* **35** 855–7
[22] McMillan P F 2002 New materials from high-pressure experiments *Nat. Mater.* **1** 19–25
[23] Duffy T S 2008 Mineralogy at the extremes *Nature* **451** 269–70
[24] Mao H K and Hemley R J 2007 The high-pressure dimension in earth and planetary science *Proc. Natl Acad. Sci.* **104** 9114–5
[25] Smeller L, Roemich H and Lange R 2006 Proteins under high pressure *Biochim. Biophysi. Acta (BBA)* **1716** 329–30
[26] Akahama Y and Kawamura H 2007 Diamond anvil Raman gauge in multimegabar pressure range *High Press. Res.* **27** 473–82
[27] Dubrovinsky L, Dubrovinskaia N, Prakapenka V B and Abakumov A M 2012 Implementation of micro-ball nanodiamond anvils for high-pressure studies above 6 Mbar *Nat. Commun.* **3** 1163
[28] Yamazaki D *et al* 2014 Over 1 Mbar generation in the Kawai-type multianvil apparatus and its application to compression of $(Mg_{0.92}Fe_{0.08})SiO_3$ perovskite and stishovite *Phys. Earth Planet. Inter.* **228** 262–7
[29] Smith R F *et al* 2014 Ramp compression of diamond to five terapascals *Nature* **511** 330–3
[30] Bassett W A 2009 Diamond anvil cell, 50th birthday *High Press. Res.* **29** 163–86
[31] Hemley R J, Struzhkin V V and Cohen R E 2007 Measuring high-pressure electronic and magnetic properties *Treatise on Geophysics* ed G Shubert (Amsterdam: Elsevier) pp 293–337
[32] Mao H K and Mao W L 2007 Diamond-anvil cells and probes for high *P-T* mineral physics *Treatise on Geophysics* ed G D Price (Amsterdam: Elsevier) pp 231–68
[33] Mao H K *et al* 1990 Static compression of iron to 300 GPa and $Fe_{0.8}Ni_{0.2}$ alloy to 260 GPa: implications for composition of the core *J. Geophys. Res.* **95** 21737–42
[34] Boehler R 2000 High pressure experiments and the phase diagram of lower mantle and core materials *Rev. Geophys.* **38** 221–45
[35] Webb A W, Gubser D U and Towle L C 1976 Cryostat for generating pressures to 100 kilobar and temperatures to 0.03 K *Rev. Sci. Instrum.* **47** 59–62
[36] Lazicki A *et al* 2009 Anomalous optical and electronic properties of dense sodium *Proc. Natl Acad. Sci.* **106** 6525–8
[37] Prakapenka V B, Shen G and Dubrovinsky L S 2004 Carbon transport in diamond anvil cell *High Temp.—High Press.* **35/36** 237–49
[38] Irifune T *et al* 2003 Materials: ultrahard polycrystalline diamond from graphite *Nature* **421** 599–600
[39] Irifune T *et al* 2003 Correction: ultrahard polycrystalline diamond from graphite *Nature* **421** 806
[40] Ohfuji H *et al* 2010 Laser heating in nano-polycrystalline diamond anvil cell *J. Phys.: Conf. Ser.* **215** 012192
[41] Goncharenko I N 2004 Neutron diffraction experiments in diamond and sapphire anvil cells *High Press. Res.* **24** 193–204
[42] Wang Z *et al* 2010 Portable high pressure sapphire anvil cell for gas hydrates research *Rev. Sci. Instrum.* **81** 085102
[43] Xu J-A and Mao H-K 2000 Moissanite: a window for high-pressure experiments *Science* **290** 783–5
[44] Boehler R and De Hantsetters K 2004 New anvil designs in diamond-cells *High Press. Res.* **24** 391–6
[45] Hemley R J *et al* 1997 X-ray imaging of stress and strain of diamond, iron, and tungsten at megabar pressures *Science* **276** 1242
[46] Merkel S, Hemley R J and Mao H K 1999 Finite element modeling of diamond deformation at multimegabar pressures *Appl. Phys. Lett.* **74** 656–8
[47] Mao H K, Bell P M and Hemley R J 1985 Ultrahigh pressures: optical observations and Raman measurements of hydrogen and deuterium to 1.47 Mbar *Phys. Rev. Lett.* **55** 99–102
[48] Dubrovinsky L *et al* 2015 The most incompressible metal osmium at static pressures above 750 gigapascals *Nature* **525** 226–9
[49] Dubrovinskaia N *et al* 2016 Terapascal static pressure generation with ultrahigh yield strength nanodiamond *Sci. Adv.* **2** e1600341
[50] Sakai T *et al* 2015 High-pressure generation using double stage micro-paired diamond anvils shaped by focused ion beam *Rev. Sci. Instrum.* **86** 033905
[51] Vohra Y K *et al* 2015 High pressure studies using two-stage diamond micro-anvils grown by chemical vapor deposition *High Press. Res.* **35** 282–8
[52] Boehler R 2006 New diamond cell for single-crystal x-ray diffraction *Rev. Sci. Instrum.* **77** 115103
[53] Bassett W A, Anderson A J, Mayanovic R A and Chou I M 2000 Hydrothermal diamond anvil cell for XAFS studies of first-row transition elements in aqueous solution up to supercritical conditions *Chem. Geol.* **167** 3–10
[54] Dadashev A, Pasternak M P, Rozenberg G K and Taylor R D 2001 Applications of perforated diamond anvils for very high-pressure research *Rev. Sci. Instrum.* **72** 2633–7
[55] Ding Y *et al* 2009 Pressure-induced magnetic transition in manganite $(La_{0.75}Ca_{0.25}MnO_3)$ *Phys. Rev. Lett.* **102** 237201
[56] Ding Y *et al* 2008 Novel pressure-induced magnetic transition in magnetite (Fe_3O_4) *Phys. Rev. Lett.* **100** 045508
[57] Rueff J P *et al* 2006 Probing the gamma-alpha transition in bulk Ce under pressure: a direct investigation by resonant inelastic x-ray scattering *Phys. Rev. Lett.* **96** 237403
[58] Zeng Q-S *et al* 2009 Substitutional alloy of Ce and AI *Proc. Natl Acad. Sci.* **106** 2515–8
[59] Haskel D, Tseng Y C, Lang J C and Sinogeikin S 2007 Instrument for x-ray magnetic circular dichroism measurements at high pressures *Rev. Sci. Instrum.* **78** 083904
[60] Benmore C J *et al* 2010 Structural and topological changes in silica glass at pressure *Phys. Rev.* B **81** 054105

[61] Mei Q *et al* 2010 High-pressure x-ray diffraction measurements on vitreous GeO_2 under hydrostatic conditions *Phys. Rev.* B **81** 174113
[62] Mao H K *et al* 1998 Elasticity and rheology of iron above 200 GPa and the nature of the Earth's inner core *Nature* **396** 741–3
[63] Mao H K *et al* 2001 Phonon density of states of iron up to 153 Gigapascals *Science* **292** 914–6
[64] Merkel S and Yagi T 2005 X-ray transparent gasket for diamond anvil cell high pressure experiments *Rev. Sci. Instrum.* **76** 046109
[65] Jackson D D *et al* 2003 Magnetic susceptibility measurements at high pressure using designer diamond anvils *Rev. Sci. Instrum.* **74** 2467–71
[66] Weir S T *et al* 2000 Epitaxial diamond encapsulation of metal microprobes for high pressure experiments *Appl. Phys. Lett.* **77** 3400–2
[67] Sung C-M, Goetze C and Mao H K 1977 Pressure distribution in the diamond anvil press and the shear strength of fayalite *Rev. Sci. Instrum.* **48** 1386–91
[68] Dunstan D J 1989 Theory of the gasket in diamond anvil high-pressure cells *Rev. Sci. Instrum.* **60** 3789–95
[69] Zou G T *et al* 2001 A diamond gasket for the laser-heated diamond anvil cell *Rev. Sci. Instrum.* **72** 1298–301
[70] He D *et al* 2003 Bulk metallic glass gasket for high pressure, *in situ* x-ray diffraction *Rev. Sci. Instrum.* **74** 3012–6
[71] Lin J F *et al* 2003 Amorphous boron gasket in diamond anvil cell research *Rev. Sci. Instrum.* **74** 4732–6
[72] Mao W L *et al* 2003 Bonding changes in compressed superhard graphite *Science* **302** 425–7
[73] Mao W L *et al* 2006 Iron-rich post-perovskite and the origin of ultralow-velocity zones *Science* **312** 564–5
[74] Eremets M I, Hemley R J, Mao H K and Gregoryanz E 2001 Semiconducting non-molecular nitrogen up to 240 GPa and its low-pressure stability *Nature* **411** 170–4
[75] Funamori N and Sato T 2008 A cubic boron nitride gasket for diamond-anvil experiments *Rev. Sci. Instrum.* **79** 053903
[76] Hrubiak R *et al* 2015 The laser micro-machining system for diamond anvil cell experiments and general precision machining applications at the High Pressure Collaborative Access Team *Rev. Sci. Instrum.* **86** 072202
[77] Shen G *et al* 2002 Molar volumes of liquids measured in a diamond anvil cell *Appl. Phys. Lett.* **81** 1411–3
[78] Besson J M and Pinceaux J P 1979 Melting of helium at room temperature and high pressure *Science* **206** 1073–5
[79] Piermarini G J, Block S and Barnett J D 1973 Hydrostatic limits in liquids and solids to 100 kbar *J. Appl. Phys.* **44** 5377–82
[80] Loubeyre P *et al* 1996 X-ray diffraction and equation of state of hydrogen at megabar pressures *Nature* **383** 702–4
[81] Takemura K and Singh A K 2006 High-pressure equation of state for Nb with a helium-pressure medium: powder x-ray diffraction experiments *Phys. Rev.* B **73** 224119
[82] Dewaele A, Loubeyre P and Mezouar M 2004 Equations of state of six metals above 94 GPa *Phys. Rev.* B **70** 094112
[83] Klotz S, Chervin J C, Munsch P and Marchand G L 2009 Hydrostatic limits of 11 pressure transmitting media *J. Phys. D: Appl. Phys.* **42** 075413
[84] Mills R L, Liebenberg D H, Bronson J C and Schmidt L C 1980 Procedure for loading diamond cells with high-pressure gas *Rev. Sci. Instrum.* **51** 891–5
[85] Rivers M *et al* 2008 The COMPRES/GSECARS gas-loading system for diamond anvil cells at the advanced photon source *High Press. Res.* **28** 273–92
[86] Takemura K, Sahu P C, Yoshiyasu K and Yasuo T 2001 Versatile gas-loading system for diamond anvil cells *Rev. Sci. Instrum.* **72** 3873–6
[87] Zhao J, Shen G, Sturhahn W and Alp E E 2004 Highly efficient gaseous sample loading technique for diamond anvil cells *Rev. Sci. Instrum.* **75** 5149–51
[88] Durham W B, Weidner D J, Karato S-I and Wang Y 2002 New developments in deformation experiments at high pressure *Rev. Mineral. Geochem.* **51** 21–49
[89] Singh A K 1993 The lattice strains in a specimen (cubic system) compressed nonhydrostatically in an opposed anvil device *J. Appl. Phys.* **73** 4278–86
[90] Miyagi L *et al* 2010 Slip systems in $MgSiO_3$ post-perovskite: implications for D'' anisotropy *Science* **329** 1639–41
[91] Merkel S, Liermann H P, Miyagi L and Wenk H R 2013 *In situ* radial x-ray diffraction study of texture and stress during phase transformations in bcc-, fcc- and hcp-iron up to 36 GPa and 1000 K *Acta Mater.* **61** 5144–51
[92] Mao H K, Bell P M, Shaner J and Steinberg D 1978 Specific volume measurements of Cu, Mo, Pd, and Ag and calibration of the ruby R_1 fluorescence pressure gauge from 0.06 to 1 Mbar *J. Appl. Phys.* **49** 3276–83
[93] Zha C-S, Mao H-K and Hemley R J 2000 Elasticity of MgO and a primary pressure scale to 55 GPa *Proc. Natl Acad. Sci.* **97** 13494–9
[94] Forman R A, Piermarini G J, Barnett J D and Block S 1972 Pressure measurement made by the utilization of ruby sharp-line luminescence *Science* **176** 284–5
[95] Mao H K, Xu J and Bell P M 1986 Calibration of the ruby pressure gauge to 800 kbar under quasihydrostatic conditions *J. Geophys. Res.* **91** 4673–6
[96] Chijioke A D, Nellis W J and Silvera I F 2005 High-pressure equations of state of Al, Cu, Ta, and W *J. Appl. Phys.* **98** 073526
[97] Fei Y W *et al* 2007 Toward an internally consistent pressure scale *Proc. Natl Acad. Sci.* **104** 9182–6
[98] Goncharov A F *et al* 2007 Probing of structure factor of water to 57 GPa and 1500 K *Materials Research Society Symp. Proc.* vol 987 p 0987-PP0904-0903
[99] Parker L J, Atou T and Badding J V 1996 Transition element-like chemistry for potassium under pressure *Science* **273** 95–7
[100] Somayazulu M *et al* 2010 Pressure-induced bonding and compound formation in xenon–hydrogen solids *Nat. Chem.* **2** 50–3
[101] Farber D L *et al* 2006 Lattice dynamics of molybdenum at high pressure *Phys. Rev. Lett.* **96** 115502
[102] Shen G *et al* 2012 Direct observation of a pressure-induced precursor lattice in silicon *Phys. Rev. Lett.* **109** 205503
[103] Li R *et al* 2015 Pressure-induced changes in the electron density distribution in α-Ge near the $\alpha - \beta$ transition *Appl. Phys. Lett.* **107** 072109
[104] Zhao Y-X, Buehler F, Sites J R and Spain I L 1986 New metastable phases of silicon *Solid State Commun.* **59** 679–82
[105] Haberl B *et al* 2014 Controlled formation of metastable germanium polymorphs *Phys. Rev.* B **89** 144111
[106] Evans W J *et al* 2007 Dynamic diamond anvil cell (dDAC): a novel device for studying the dynamic-pressure properties of materials *Rev. Sci. Instrum.* **78** 073904
[107] Lin C *et al* 2016 Kinetics of the *B*1-*B*2 phase transition in KCl under rapid compression *J. Appl. Phys.* **119** 045902
[108] Sinogeikin S V *et al* 2015 Online remote control systems for static and dynamic compression and decompression using diamond anvil cells *Rev. Sci. Instrum.* **86** 072209
[109] Daniels W B and Ryschkewitsch M G 1983 Simple double diaphragm press for diamond anvil cells at low-temperatures *Rev. Sci. Instrum.* **54** 115–6
[110] Smith J S *et al* 2015 Developments in time-resolved high pressure x-ray diffraction using rapid compression and decompression *Rev. Sci. Instrum.* **86** 072208
[111] Haberl B *et al* 2015 Thermal evolution of the metastable r8 and bc8 polymorphs of silicon *High Press. Res.* **35** 99–116

[112] Konôpková Z *et al* 2015 *In situ* x-ray diffraction of fast compressed iron: analysis of strains and stress under non-hydrostatic pressure *Phys. Rev.* B **91** 144101

[113] Pugh E 2013 Note: compact optical fiber coupler for diamond anvil high pressure cells *Rev. Sci. Instrum.* **84** 106108

[114] Graf D E, Stillwell R L, Purcell K M and Tozer S W 2011 Nonmetallic gasket and miniature plastic turnbuckle diamond anvil cell for pulsed magnetic field studies at cryogenic temperatures *High Press. Res.* **31** 533–43

[115] Morris I C, Read D A and Temple B K 1970 A simple helium gas-flow cryostat for the temperature range 4–300 K *J. Phys. E: Sci. Instrum.* **3** 343

[116] Yamaoka H *et al* 2012 Ruby pressure scale in a low-temperature diamond anvil cell *J. Appl. Phys.* **112** 124503

[117] Fei Y and Mao H K 1994 *In situ* determination of the NiAs phase of FeO at high pressure and high temperature *Science* **266** 1678–80

[118] Jenei Z, Cynn H, Visbeck K and Evans W J 2013 High-temperature experiments using a resistively heated high-pressure membrane diamond anvil cell *Rev. Sci. Instrum.* **84** 095114

[119] Dubrovinsky L *et al* 2000 *In situ* x-ray study of thermal expansion and phase transition of iron at multimegabar pressure *Phys. Rev. Lett.* **84** 1720–3

[120] Seal M 1963 The effect of surface orientation on the graphitization of diamond *Phys. Status Solidi* b **3** 658–64

[121] Shen G *et al* 2007 Distinct thermal behavior of GeO_2 glass in tetrahedral, intermediate, and octahedral forms *Proc. Natl Acad. Sci.* **104** 14576–9

[122] Shen G *et al* 2010 A portable laser heating microscope for high pressure research *J. Phys.* **215** 012191

[123] Boehler R 1986 The phase diagram of iron to 430 kbar *Geophy. Res. Lett.* **13** 1153–6

[124] Mao H K, Bell P M and Hadidiacos C 1987 Experimental phase relations of iron to 360 kbar and 1400 C, determined in an internally heated diamond anvil apparatus *High Pressure Research in Mineral Physics* ed M H Manghnani and Y Syono (Tokyo: Terra Scientific) pp 135–8

[125] Zha C S and Bassett W A 2003 Internal resistive heating in diamond anvil cell for *in situ* x-ray diffraction and Raman scattering *Rev. Sci. Instrum.* **74** 1225–62

[126] Bureau H *et al* 2006 Intelligent anvils applied to experimental investigations: state-of-the-art *High Press. Res.* **26** 251–65

[127] Weir S T and Vohra Y K 2012 Advances in customized diamond anvils *High-Pressure Physics* ed J Loveday (Boca Raton, FL: CRC Press) pp 61–80

[128] Liu L 1976 Orthorhombic perovskite phases observed in olivine, pyroxene, and garnet at high pressures and temperatures *Phys. Earth Planet. Inter.* **11** 289–98

[129] Mao H K, Yagi T and Bell P M 1977 Mineralogy of the Earth's deep mantle: quenchng experiments of mineral compositions at high pressures and temperatures *Carnegy Inst. Wash. Year Book* **76** 502–4

[130] Murakami M *et al* 2004 Post-perovskite phase transition in $MgSiO_3$ *Science* **304** 855–8

[131] Mao W L *et al* 2004 Ferromagnesian postperovskite silicates in the D'' layer of the Earth *Proc. Natl Acad. Sci.* **101** 15867–9

[132] Shen G, Mao H K and Hemley R J 1996 Laser-heating diamnd-anvil cell technique: double-sided heating with multimode Nd:YAG laser *Advanced Materials'96—New Trends in High Pressure Research* (Tsukuba: NIRIM) pp 149–52

[133] Mao H K, Shen G, Hemley R J and Duffy T S 1998 X-ray diffraction with a double hot plate laser heated diamond cell *Properties of Earth and Planetary Materials* ed M H Manghnani and T Yagi (Washington, DC: AGU) pp 27–34

[134] Meng Y *et al* 2015 New developments in laser-heated diamond anvil cell with *in situ* synchrotron x-ray diffraction at high pressure collaborative access team *Rev. Sci. Instrum.* **86** 072201

[135] Shen G, Rivers M L, Wang Y and Sutton S J 2001 A laser heated diamond cell system at the advanced photon source for *in situ* x-ray measurements at high pressure and temperature *Rev. Sci. Instrum.* **72** 1273–82

[136] Prakapenka V B *et al* 2008 Advanced flat top laser heating system for high pressure research at GSECARS: application to the melting behavior of germanium *High Press. Res.* **28** 225–35

[137] Heinz D L and Jeanloz R 1987 Temperature measurements in the laser heated diamond cell *High Pressure Researches in Mineral Physics* ed H M Manghnani and Y Syono (Washington, DC: AGU) pp 113–27

[138] Zhao J *et al* 2004 Nuclear resonant scattering at high pressure and high temperature *High Press. Res.* **24** 447–57

[139] Meng Y, Shen G and Mao H-K 2006 Double-sided laser heating system at HPCAT for *in situ* x-ray diffraction at high pressures and high temperatures *J. Phys.: Condens. Matter* **18** s1097–103

[140] Watanuki T *et al* 2001 Construction of laser-heated diamond anvil cell system for in situ x-ray diffraction study at SPring-8 *Rev. Sci. Instrum.* **72** 1289

[141] Schultz E *et al* 2005 Double-sided laser heating system for *in situ* high pressure and high temperature monochromatic x-ray diffraction at the ESRF *High Press. Res.* **25** 71–83

[142] Boehler R *et al* 2009 Portable laser-heating stand for synchrotron applications *Rev. Sci. Instrum.* **80** 045103

[143] Dubrovinsky L *et al* 2009 Portable laser-heating system for diamond anvil cells *J. Synchrotron Radiat.* **16** 737–41

[144] Deemyad S *et al* 2005 Pulsed laser heating and temperature determination in a diamond anvil cell *Rev. Sci. Instrum.* **76** 125104

[145] Funamori N and Sato T 2006 Heating in a diamond-anvil cell using relaxation oscillations of a Q-switched Nd:YAG laser *Rev. Sci. Instrum.* **77** 093903

[146] Beck P *et al* 2007 Measurement of thermal diffusivity at high pressure using a transient heating technique *Appl. Phys. Lett.* **91** 181914

[147] Goncharov A F *et al* 2009 Laser heating in diamond anvil cells: developments in pulsed and continuous techniques *J. Synchrotron Radiat.* **16** 769–72

[148] Goncharov A F *et al* 2010 X-ray diffraction in the pulsed laser heated diamond anvil cell *Rev. Sci. Instrum.* **81** 113902

[149] Du Z, Amulele G, Robin Benedetti L and Lee K K M 2013 Mapping temperatures and temperature gradients during flash heating in a diamond-anvil cell *Rev. Sci. Instrum.* **84** 075111

[150] Wang Y *et al* 2005 High-pressure x-ray tomography microscope: synchrotron computed microtomography at high pressure and temperature *Rev. Sci. Instrum.* **76** 073709

[151] Wang J *et al* 2012 High pressure nano-tomography using an iterative method *J. Appl. Phys.* **111** 112626

[152] Mayanovic R A, Anderson A J, Bassett W A and Chou I M 2007 Synchrotron x-ray spectroscopy of Eu/HNO_3 aqueous solutions at high temperatures and pressures and Nb-bearing silicate melt phases coexisting with hydrothermal fluids using a modified hydrothermal diamond anvil cell and rail assembly *Rev. Sci. Instrum.* **78** 053904

[153] Cainrs R J R, Ottewill R H, Osmond D W J and Wagstraff I 1976 Studies on the preparation and properties of latices in nonpolar media *J. Colloid Interface Sci.* **54** 45–51

[154] Sturhahn W 2004 Nuclear resonant scattering *J. Phys.: Condens. Matter* **16** S497–530

[155] Lübbers R, Grünsteudel H F, Chumakov A I and Wortmann G 2000 Density of states in iron at high pressure *Science* **287** 1250–3

[156] Yoo C S *et al* 2011 Time- and angle-resolved x-ray diffraction to probe structural and chemical evolution during Al–Ni intermetallic reactions *Rev. Sci. Instrum.* **82** 113901–6

[157] Shen G *et al* 2008 HPCAT: an integrated high-pressure synchrotron facility at the advanced photon source *High Press. Res.* **28** 145–62

[158] Mezouar M *et al* 2005 Development of a new state-of-the-art beamline optimized for monochromatic single-crystal and powder x-ray diffraction under extreme conditions at the ESRF *J. Synchrotron Radiat.* **12** 659–64

[159] Kono Y *et al* 2014 Toward comprehensive studies of liquids at high pressures and high temperatures: combined structure, elastic wave velocity, and viscosity measurements in the Paris–Edinburgh cell *Phys. Earth Planet. Inter.* **228** 269–80

[160] Kono Y *et al* 2016 Ultrahigh-pressure polyamorphism in GeO_2 glass with coordination number >6 *Proc. Natl Acad. Sci.* **113** 3436–41

[161] Mezouar M *et al* 2002 Multichannel collimator for structural investigation of liquids and amorphous materials at high pressures and temperatures *Rev. Sci. Instrum.* **73** 3570–4

[162] Chow P *et al* 2015 Focusing polycapillary to reduce parasitic scattering for inelastic x-ray measurements at high pressure *Rev. Sci. Instrum.* **86** 072203

[163] Takahashi T, Mao H K and Bassett W A 1969 Lead: x-ray diffraction study of a high-pressure polymorph *Science* **165** 1352–3

[164] Taylor L A and Mao H K 1970 A high-pressure polymorph of troilite *Science* **170** 850–1

[165] Lavina B, Dera P and Downs R T 2014 Modern x-ray diffraction methods in mineralogy and geosciences *Rev. Mineral. Geochem.* **78** 1–31

[166] Sørensen Henning O *et al* 2012 Multigrain crystallography *Z. Kristallogr. Cryst. Mater.* **227** 63

[167] Zhang L *et al* 2013 Single-crystal structure determination of $(Mg,Fe)SiO_3$ postperovskite. *Proc. Natl Acad. Sci.* **110** 6292–5

[168] Zhang L *et al* 2016 *In situ* crystal structure determination of seifertite SiO_2 at 129 GPa: studying a minor phase near Earth's core-mantle boundary *Am. Mineral.* **101** 231–4

[169] Ding Y *et al* 2007 Structural phase transition of vanadium at 69 GPa *Phys. Rev. Lett.* **98** 085502

[170] Occelli F *et al* 2004 Experimental evidence for a high-pressure isostructural phase transition in osmium *Phys. Rev. Lett.* **93** 095502

[171] Ahart M *et al* 2008 Origin of morphotropic phase boundaries in ferroelectrics *Nature* **451** 545–8

[172] Fei Y *et al* 2007 Spin transition and equations of state of (Mg, Fe)O solid solutions *Geophys. Res. Lett.* **34** L17307

[173] Lin J-F *et al* 2005 Spin transition of iron in magnesiowüstite in the Earth's lower mantle *Nature* **436** 377–80

[174] Lin J-F, Speziale S, Mao Z and Marquardt H 2013 Effects of the electronic spin transitions of iron in lower mantle minerals: implications for deep mantle geophysics and geochemistry *Rev. Geophys.* **51** 244–75

[175] Rütt U *et al* 2001 Diffractometer for high energy x-rays at the APS *Nucl. Instrum. Methods* A **467–8** 1026–9

[176] Wang Y *et al* 2004 A new technique for angle-dispersive powder diffraction using an energy-dispersive setup and synchrotron radiation *J. Appl. Cryst.* **37** 947–56

[177] Yang W, Shen G, Wang Y and Mao H K 2008 A scanning angle energy-dispersive x-ray diffraction technique for high-pressure structure studies in diamond anvil cells *High Press. Res.* **28** 193–201

[178] Rietveld H M 1966 A method for including line profiles of neutron powder diffraction peaks in determination of crystal structures *Acta Crystallogr.* **S 21** A228

[179] Shen G, Prakapenka V B, Rivers M L and Sutton S R 2003 Structural investigation of amorphous materials at high pressures using the diamond anvil cell *Rev. Sci. Instrum.* **74** 3021–6

[180] Chapman K W *et al* 2010 Optimizing high-pressure pair distribution function measurements in diamond anvil cells *J. Appl. Crystal.* **43** 297–307

[181] Soignard E, Benmore C J and Yarger J L 2010 A perforated diamond anvil cell for high-energy x-ray diffraction of liquids and amorphous solids at high pressure *Rev. Sci. Instrum.* **81** 035110

[182] Eggert J H, Weck G, Loubeyre P and Mezouar M 2002 Quantitative structure factor and density measurements of high-pressure fluids in diamond anvil cells by x-ray diffraction: argon and water *Phys. Rev.* B **65** 174105

[183] Oganov A R 2010 *Modern Methods of Crystal Structure Prediction* (New York: Wiley)

[184] Wang Y and Ma Y 2014 Perspective: crystal structure prediction at high pressures *J. Chem. Phys.* **140** 040901

[185] Boffa Ballaran T, Kurnosov A and Trots D 2013 Single-crystal x-ray diffraction at extreme conditions: a review *High Press. Res.* **33** 453–65

[186] Dera P *et al* 2013 High pressure single-crystal micro x-ray diffraction analysis with GSE_ADA/RSV software *High Press. Res.* **33** 466–84

[187] Mao H-K *et al* 1988 Synchrotron x-ray diffraction measurements of single-crystal hydrogen to 26.5 Gigapascals *Science* **239** 1131–4

[188] Friedrich A *et al* 2007 Single-crystal structure refinement of diaspore at 50 GPa *Am. Mineral.* **92** 1640–4

[189] Lavina B *et al* 2010 Structure of siderite $FeCO_3$ to 56 GPa and hysteresis of its spin-pairing transition *Phys. Rev.* B **82** 064110

[190] Ice G E, Dera P, Liu W J and Mao H K 2005 Adapting polychromatic x-ray microdiffraction techniques to high-pressure research: energy scan approach *J. Synchrotron Radiat.* **12** 608–17

[191] Ice G E and Pang J W L 2009 Tutorial on x-ray micro Laue diffraction *Mater. Charact.* **60** 1191–201

[192] Popov D, Park C, Kenney-Benson C and Shen G 2015 High pressure Laue diffraction and its application to study microstructural changes during the $\alpha \rightarrow \beta$ phase transition in Si *Rev. Sci. Instrum.* **86** 072204

[193] Gregoryanz E *et al* 2008 Structural diversity of sodium *Science* **320** 1054–7

[194] Loubeyre P *et al* 1999 Modulated phases and proton centring in ice observed by x-ray diffraction up to 170 GPa *Nature* **397** 503–6

[195] Zhang L *et al* 2014 Disproportionation of $(Mg,Fe)SiO_3$ perovskite in Earth's deep lower mantle *Science* **344** 877–82

[196] Wilding M C, Wilson M and McMillan P F 2006 Structural studies and polymorphism in amorphous solids and liquids at high pressure *Chem. Soc. Rev.* **35** 964–86

[197] Tsuji K *et al* 1989 Measurements of x-ray diffraction for liquid metals under high pressure *Rev. Sci. Instrum.* **60** 2425–8

[198] Katayama Y *et al* 2000 A first order liquid-liquid phase transition in phosphorus *Nature* **403** 170–3

[199] Deb S K, Wilding M, Somayazulu M and McMillan P F 2001 Pressure-induced amorphization and an amorphous-amorphous transition in densified porous silicon *Nature* **414** 528–30

[200] Zeng Q *et al* 2011 Long-range topological order in metallic glass *Science* **332** 1404–6

[201] Meade C, Hemley R J and Mao H K 1992 High pressure x-ray diffraction of SiO_2 glass *Phys. Rev. Lett.* **69** 1387–90

[202] Funakoshi K 1995 Energy-dispersive x-ray diffraction study for alkali silicate melts using synchrotron radiation under high pressure and temperature *PhD Thesis* Institute of Technology, Tokyo

[203] Yamada A *et al* 2011 High-pressure x-ray diffraction studies on the structure of liquid silicate using a Paris–Edinburgh type large volume press *Rev. Sci. Instrum.* **82** 015103
[204] Sakamaki T *et al* 2012 Structure of jadeite melt at high pressures up to 4.9 GPa *J. Appl. Phys.* **111** 112623
[205] Guthrie M *et al* 2004 Formation and structure of a dense octahedral glass *Phys. Rev. Lett.* **93** 15502
[206] Wenk H R *et al* 2000 The plastic deformation of iron at pressures of the Earth's inner core *Nature* **405** 1044–7
[207] Merkel S *et al* 2006 Plastic deformation of $MgGeO_3$ post-Perovskite at lower mantle pressures *Science* **311** 644–6
[208] Wenk H R *et al* 2005 Texture development and deformation mechanisms in ringwoodite *Phys. Earth Planet. Inter.* **152** 191–9
[209] Hilairet N *et al* 2012 Deformation of olivine under mantle conditions: an *in situ* high-pressure, high-temperature study using monochromatic synchrotron radiation *J. Geophys. Res.* **117** B01203
[210] Wang Y, Durham W B, Getting I C and Weidner D J 2003 The deformation-DIA: a new apparatus for high temperature triaxial deformation to pressures up to 15 GPa *Rev. Sci. Instrum.* **74** 3002–11
[211] Wang Y *et al* 2000 High pressure research using large-volume presses at GeoSoilEnviroCARS advanced photon source *AIRAPT-17* pp 1047–52
[212] Yamazaki D and Karato S 2001 High pressure rotational deformation apparatus to 15 GPa *Rev. Sci. Instrum.* **72** 4207–11
[213] Nishiyama N *et al* 2007 Rheology of ε-iron up to 19 GPa and 600 K in the D-DIA *Geophys. Res. Lett.* **34** L23304
[214] Hilairet N *et al* 2007 High-pressure creep of serpentine, interseismic deformation, and initiation of subduction *Science* **318** 1910–3
[215] Ingalls R, Garcia G A and Stern E A 1978 X-ray absorption at high pressure *Phys. Rev. Lett.* **40** 334
[216] Zeng Q S *et al* 2010 Origin of pressure-induced polyamorphism in $Ce_{75}Al_{25}$ metallic glass *Phys. Rev. Lett.* **104** 105702
[217] Ishimatsu N *et al* 2012 Glitch-free x-ray absorption spectrum under high pressure obtained using nano-polycrystalline diamond anvils *J. Synchrotron Radiat.* **19** 768–72
[218] Baldini M *et al* 2011 High-pressure EXAFS measurements of crystalline Ge using nanocrystalline diamond anvils *Phys. Rev.* B **84** 014111
[219] Hong X *et al* 2009 High quality x-ray absorption spectroscopy measurements with long energy range at high pressure using diamond anvil cell *Rev. Sci. Instrum.* **80** 073908
[220] Park C *et al* 2015 New developments in micro-x-ray diffraction and x-ray absorption spectroscopy for high-pressure research at 16-BM-D at the advanced photon source *Rev. Sci. Instrum.* **86** 072205
[221] Pascarelli S and Mathon O 2010 Advances in high brilliance energy dispersive x-ray absorption spectroscopy *Phys. Chem. Chem. Phys.* **12** 5535–46
[222] Andrault D *et al* 2010 Experimental evidence for perovskite and post-perovskite coexistence throughout the whole D'' region *Earth Planet. Sci. Lett.* **293** 90–6
[223] Aquilanti G *et al* 2009 Development of micro-XANES mapping in the diamond anvil cell *J. Synchrotron Radiat.* **16** 376–9
[224] Ohtaka O *et al* 2004 Pressure-induced sharp coordination change in liquid germanate *Phys. Rev. Lett.* **92** 155506
[225] Itie J P *et al* 1989 Pressure-induced coordination changes in crystalline and vitreous GeO_2 *Phys. Rev. Lett.* **63** 398
[226] Mobilio S and Meneghini C 1998 Synchrotron radiation in the study of amorphous materials *J. Non·Cryst. Solids* **232–4** 25–37
[227] Caldwell D, Thorne A J M and Eyring H 1971 Magnetic circular dichroism *Annu. Rev. Phys. Chem.* **22** 259–78
[228] Torchio R, Mathon O and Pascarelli S 2014 XAS and XMCD spectroscopies to study matter at high pressure: probing the correlation between structure and magnetism in the 3D metals *Coord. Chem. Rev.* **277–8** 80–94
[229] Gorria P *et al* 2009 Stress-induced large Curie temperature enhancement in $Fe_{64}Ni_{36}$ Invar alloy *Phys. Rev.* B **80** 064421
[230] Iota V *et al* 2007 Electronic structure and magnetism in compressed 3D transition metals *Appl. Phys. Lett.* **90** 042505
[231] Fabbris G *et al* 2013 Different routes to pressure-induced volume collapse transitions in gadolinium and terbium metals *Phys. Rev.* B **88** 245103
[232] Sanchez-Benitez J, Tancharakorn S, Hutchison M K and Kamenev K V 2008 High-pressure cell for a SQUID magnetometer with a plug for *in situ* pressure measurements *J. Phys.: Conf. Ser.* **121** 122001
[233] Kamenev K V, Tancharakorn S, Robertson N and Harrison A 2006 Long symmetric high-pressure cell for magnetic measurements in superconducting quantum interference device magnetometer *Rev. Sci. Instrum.* **77** 073905
[234] Badro J *et al* 1999 Magnetism in FeO at megabar pressures from x-ray emission spectroscopy *Phys. Rev. Lett.* **83** 4101–4
[235] Rueff J P *et al* 1999 Pressure-induced high-spin to low-spin transition in FeS evidenced by x-ray emission spectroscopy *Phys. Rev. Lett.* **82** 3284–7
[236] Struzhkin V V *et al* 2006 Valence band x-ray emission spectra of compressed germanium *Phys. Rev. Lett.* **96** 137402
[237] Xiao Y M *et al* 2015 New developments in high pressure x-ray spectroscopy beamline at high pressure collaborative access team *Rev. Sci. Instrum.* **86** 072206
[238] Xiao Y, Chow P and Shen G 2016 High pressure x-ray emission spectroscopy at the advanced photon source *High Press. Res.* **36** 1–17
[239] Pacold J I *et al* 2012 A miniature x-ray emission spectrometer (miniXES) for high pressure studies in a diamond anvil cell *J. Synchrotron Radiat.* **19** 245–51
[240] Lin J-F *et al* 2005 X-ray emission spectroscopy with a laser-heated diamond anvil cell: a new experimental probe of the spin state of iron in the Earth's interior *J. Synchrotron Radiat.* **12** 637–41
[241] Badro J *et al* 1999 Pressure transition and magnetic collapse in FeO at pressures to 150 GPa *Phys. Rev. Lett.* **20** 4101–4
[242] Badro J *et al* 2002 Nature of the high-pressure transition in Fe_2O_3 hematite *Phys. Rev. Lett.* **89** 205504
[243] Badro J *et al* 2003 Iron partitioning in Earth's mantle: toward a deep lower mantle discontinuity *Science* **300** 789–91
[244] Li J *et al* 2004 Electronic spin state of iron in lower mantle perovskite *Proc. Natl Acad. Sci.* **101** 14027–30
[245] Lin J-F *et al* 2012 Electronic spin states of ferric and ferrous iron in the lower-mantle silicate perovskite *Am. Mineral.* **97** 592–7
[246] Yamanaka T *et al* 2012 Crystal structures of $(Mg_{1-x},Fe_x)SiO_3$ postperovskite at high pressures *Proc. Natl Acad. Sci.* **109** 1035–40
[247] Wang S *et al* 2010 High-pressure evolution of Fe_2O_3 electronic structure revealed by x-ray absorption *Phys. Rev.* B **82** 144428
[248] de Groot F M F, Krisch M H and Vogel J 2002 Spectral sharpening of the Pt\textit(L) edges by high-resolution x-ray emission *Phys. Rev.* B **66** 195112
[249] Bradley J A *et al* 2012 4f electron delocalization and volume collapse in praseodymium metal *Phys. Rev.* B **85** 100102
[250] Lipp M J *et al* 2012 X-ray emission spectroscopy of cerium across the $\gamma - \alpha$ volume collapse transition *Phys. Rev. Lett.* **109** 195705
[251] Schmidt C and Rickers K 2003 *In situ* determination of mineral solubilities in fluids using a hydrothermal

diamond-anvil cell and SR-XRF: solubility of AgCl in water *Am. Mineral.* **88** 288–92
[252] Tanis E A *et al* 2012 Solubility of xenotime in a 2 M HCl aqueous fluid from 1.2 to 2.6 GPa and 300–500 °C *Am. Mineral.* **97** 1708–13
[253] Schmidt C, Rickers K, Bilderback D H and Huang R 2007 *In situ* synchrotron-radiation XRF study of REE phosphate dissolution in aqueous fluids to 800 °C *Lithos* **95** 87–102
[254] Tanis E A *et al* 2016 Rutile solubility in NaF–NaCl–KCl-bearing aqueous fluids at 0.5–2.79 GPa and 250–650 °C *Geochim. Cosmochim. Acta* **177** 170–81
[255] Petitgirard S *et al* 2009 A diamond anvil cell for x-ray fluorescence measurements of trace elements in fluids at high pressure and high temperature *Rev. Sci. Instrum.* **80** 033906
[256] Tanis E A *et al* 2015 The mobility of Nb in rutile-saturated NaCl- and NaF-bearing aqueous fluids from 1–6.5 GPa and 300–800 °C *Am. Mineral.* **100** 1600–9
[257] Wilke M *et al* 2010 A confocal set-up for micro-XRF and XAFS experiments using diamond-anvil cells *J. Synchrotron Radiat.* **17** 669–75
[258] Wang W, Sokolov D A, Huxley A D and Kamenev K V 2011 Large volume high-pressure cell for inelastic neutron scattering *Rev. Sci. Instrum.* **82** 073903
[259] Schülke W 2007 *Electron Dynamics Studied by Inelastic X-Ray Scattering* (Oxford: Oxford University Press)
[260] Ho-kwang M, Chichang K and Russell J H 2001 Inelastic x-ray scattering at ultrahigh pressures *J. Phys.: Condens. Matter* **13** 7847
[261] Lin Y *et al* 2011 Amorphous diamond: a high-pressure superhard carbon allotrope *Phys. Rev. Lett.* **107** 175504
[262] Meng Y *et al* 2004 The formation of sp^3 bonding in compressed BN *Nat. Mater.* **3** 111–4
[263] Lee S K, Eng P J, Mao H K and Shu J F 2008 Probing and modeling of pressure-induced coordination transformation in borate glasses: inelastic x-ray scattering study at high pressure *Phys. Rev.* B **78** 214203
[264] Fister T T *et al* 2007 Local electronic structure of dicarba-closo-dodecarboranes $C_2B_{10}H_{12}$ *J. Am. Chem. Soc.* **130** 925–32
[265] Lin J-F *et al* 2007 Electronic bonding transition in compressed SiO_2 glass *Phys. Rev.* B **75** 012201
[266] Lelong G *et al* 2012 Evidence of fivefold-coordinated Ge atoms in amorphous GeO_2 under pressure using inelastic x-ray scattering *Phys. Rev.* B **85** 134202
[267] Yi Y S and Lee S K 2012 Pressure-induced changes in local electronic structures of SiO_2 and $MgSiO_3$ polymorphs: insights from *ab initio* calculations of O *K*-edge energy-loss near-edge structure spectroscopy *Am. Mineral.* **97** 897–909
[268] Cai Y Q *et al* 2005 Ordering of hydrogen bonds in high-pressure low-temperature H_2O *Phys. Rev. Lett.* **94** 025502
[269] Fister T T *et al* 2009 Intermediate-range order in water ices: nonresonant inelastic x-ray scattering measurements and real-space full multiple scattering calculations *Phys. Rev.* B **79** 174117
[270] Huotari S *et al* 2000 *Proc. of AIRAPT 17* ed M H Manghnani *et al* (University Press) pp 1017–20
[271] Arms D A *et al* 2001 Exciton dispersion and electronic excitations in hcp He_4 *Phys. Rev. Lett.* **87** 156402
[272] Mao H K *et al* 2010 Electronic structure of crystalline ^{4}He at high pressures *Phys. Rev. Lett.* **105** 186404
[273] Hill J P *et al* 1996 Inelastic x-ray scattering study of solid and liquid Li and Na *Phys. Rev. Lett.* **77** 3665–8
[274] Mao H-K *et al* 2011 Electronic dynamics and plasmons of sodium under compression *Proc. Natl Acad. Sci.* **108** 20434–7
[275] Ament L J P *et al* 2011 Resonant inelastic x-ray scattering studies of elementary excitations *Rev. Mod. Phys.* **83** 705–67
[276] Maddox B 2006 Pressure-induced electronic phase transitions in transition metal oxides and rare earth metals *PhD Thesis* University of California, Davis
[277] Lipp M J *et al* 2016 Comparison of the high-pressure behavior of the cerium oxides Ce_2O_3 and CeO_2 *Phys. Rev.* B **93** 064106
[278] Huotari S *et al* 2006 Resonant inelastic hard x-ray scattering with diced analyzer crystals and position-sensitive detectors *Rev. Sci. Instrum.* **77** 053102
[279] Gog T *et al* 2013 Spherical analyzers and monochromators for resonant inelastic hard x-ray scattering: a compilation of crystals and reflections *J. Synchrotron Radiat.* **20** 74–9
[280] Burkel E, Peisl J and Dorner B 1987 Observation of inelastic x-ray scattering from phonons *Europhys. Lett.* **3** 957
[281] Sette F *et al* 1995 Collective dynamics in water by high energy resolution inelastic x-ray scattering *Phys. Rev. Lett.* **75** 850–3
[282] Alp E E *et al* 2002 Vibrational dynamics studies by nuclear resonant inelastic x-ray scattering *Hyperfine Interact.* **144** 3–20
[283] Baron A Q R *et al* 2001 Early commissioning of the Spring-8 beamline for high resolution inelastic x-ray scattering *Nucl. Instrum. Methods* A **467–8** 627–30
[284] Wong J *et al* 2003 Phonon dispersions of fcc δ-plutonium-gallium by inelastic x-ray scattering *Science* **301** 1078–80
[285] Manley M E *et al* 2003 Phonon dispersion in uranium measured using inelastic x-ray scattering *Phys. Rev.* B **67** 052302
[286] Antonangeli D *et al* 2011 Spin crossover in ferropericlase at high pressure: a seismologically transparent transition? *Science* **331** 64–7
[287] Antonangeli D *et al* 2010 Composition of the Earth's inner core from high-pressure sound velocity measurements in Fe–Ni–Si alloys *Earth Planet. Sci. Lett.* **295** 292–6
[288] Mao Z *et al* 2012 Sound velocities of Fe and Fe–Si alloy in the Earth's core *Proc. Natl Acad. Sci.* **109** 10239–44
[289] Bosak A *et al* 2008 Lattice dynamics of vanadium: inelastic x-ray scattering measurements *Phys. Rev.* B **78** 020301
[290] Krisch M *et al* 2011 Phonons of the anomalous element cerium *Proc. Natl Acad. Sci.* **108** 9342–5
[291] Fukui H *et al* 2013 A compact system for generating extreme pressures and temperatures: an application of laser-heated diamond anvil cell to inelastic x-ray scattering *Rev. Sci. Instrum.* **84** 113902
[292] Kamada S *et al* 2014 The sound velocity measurements of Fe_3S *Am. Mineral.* **99** 98–101
[293] Shibazaki Y *et al* 2012 Sound velocity measurements in dhcp-FeH up to 70 GPa with inelastic x-ray scattering: implications for the composition of the Earth's core *Earth Planet. Sci. Lett.* **313–4** 79–85
[294] Ohtani E *et al* 2013 Sound velocity of hexagonal close-packed iron up to core pressures *Geophys. Res. Lett.* **40** 2013GL057667
[295] Sakamaki T *et al* 2016 Constraints on Earth's inner core composition inferred from measurements of the sound velocity of hcp-iron in extreme conditions *Sci. Adv.* **2** e1500802
[296] Seto M *et al* 1995 Observation of nuclear resonant scattering accompanied by phonon excitation using synchrotron radiation *Phys. Rev. Lett.* **74** 3828–31
[297] Sturhahn W *et al* 1995 Phonon density of states measured by inelastic nuclear resonant scattering *Phys. Rev. Lett.* **74** 3832–5
[298] Lin J F *et al* 2005 Sound velocities of hot dense iron: Birch's law revisited *Science* **308** 1892–4
[299] Shen G *et al* 2004 Phonon density of states in iron at high pressures and high temperatures *Phys. Chem. Mineral.* **31** 353–9

[300] Murphy C A, Jackson J M, Sturhahn W and Chen B 2011 Grüneisen parameter of hcp-Fe to 171 GPa *Geophys. Res. Lett.* **38** L24306

[301] Wicks J K, Jackson J M and Sturhahn W 2010 Very low sound velocities in iron-rich (Mg,Fe)O: implications for the core-mantle boundary region *Geophys. Res. Lett.* **37** L15304

[302] Murphy C A, Jackson J M, Sturhahn W and Chen B 2011 Melting and thermal pressure of hcp-Fe from the phonon density of states *Phys. Earth Planet. Inter.* **188** 114–20

[303] Hastings J B *et al* 1991 Mössbauer spectroscopy using synchrotron radiation *Phys. Rev. Lett.* **66** 770–3

[304] Takano M *et al* 1991 Pressure-induced high-spin to low-spin transition in $CaFeO_3$ *Phys. Rev. Lett.* **67** 3267–70

[305] Nasu S 1996 High pressure Mossbauer spectroscopy with nuclear forward scattering of synchrotron radiation *High Press. Res.* **14** 405–12

[306] Chefki M *et al* 1998 Pressure-induced transition of the sublattice magnetization in $EuCo_2P_2$: change from local moment Eu(4*f*) to itinerant Co(3*d*) magnetism *Phys. Rev. Lett.* **80** 802–5

[307] Catalli K *et al* 2011 Effects of the Fe^{3+} spin transition on the properties of aluminous perovskite—new insights for lower-mantle seismic heterogeneities *Earth Planet. Sci. Lett.* **310** 293–302

[308] Chen B *et al* 2012 Spin crossover equation of state and sound velocities of $(Mg_{0.65}Fe_{0.35})O$ ferropericlase to 140 GPa *J. Geophys. Res.* **117** B08208

[309] Jackson J M *et al* 2005 A synchrotron Mossbauer spectroscopy study of (Mg,Fe)SiO_3 perovskite up to 120 GPa *Am. Mineral.* **90** 199–205

[310] Shim S-H *et al* 2009 Electronic and magnetic structures of the postperovskite-type Fe_2O_3 and implications for planetary magnetic records and deep interiors *Proc. Natl Acad. Sci.* **106** 5508–12

[311] Speziale S *et al* 2005 Iron spin transition in Earth's mantle *Proc. Natl Acad. Sci.* **102** 17918–22

[312] Jackson J M *et al* 2013 Melting of compressed iron by monitoring atomic dynamics *Earth Planet. Sci. Lett.* **362** 143–50

[313] Oomi G *et al* 1998 High-pressure system for Compton scattering experiments *J. Synchrotron Radiat.* **5** 932–4

[314] Tse J S *et al* 2005 Compton scattering of elemental silicon at high pressure *Appl. Phys. Lett.* **87** 259602

[315] Hämäläinen K *et al* 2000 Free electron gas under high pressure *Phys. Rev.* B **62** R735–8

[316] Baublitz M A, Arnold V and Ruoff A L 1981 Energy dispersive x-ray diffraction from high pressure polycrystalline specimens using synchrotron radiation *Rev. Sci. Instrum.* **52** 1616–24

[317] Vohra Y K, Weir S T and Ruoff A L 1985 High-pressure phase transitions and equation of state of the III–V compound InAs up to 27 GPa *Phys. Rev.* B **31** 7344–8

[318] Dewaele A, Loubeyre P, Andre R and Hartwig J 2006 An x-ray topographic study of diamond anvils: correlation between defects and helium diffusion *J. Appl. Phys.* **99** 104906

[319] Liang Q *et al* 2013 Developments in synthesis, characterization, and application of large, high-quality CVD single crystal diamond *J. Superhard Mater.* **35** 195–213

[320] Hong X *et al* 2007 Intermediate states in GeO_2 glass under pressures up to 35 GPa *Phys. Rev.* B **75** 104201

[321] Katayama Y *et al* 1996 Density of liquid tellurium under pressure *J. Non-Cryst. Solids* **205** 451–4

[322] Kanzaki M *et al* 1987 A new technique to measure the viscosity and density of silicate melts at high pressure *High-pressure Research in Mineral Physics* ed M H Manghnani and Y Syono (Tokyo: TERRA) pp 195–200

[323] Rutter M D *et al* 2002 Viscosity of liquid Fe at high pressure *Phys. Rev.* B **66** 060102

[324] Kono Y *et al* 2013 Anomaly in the viscosity of liquid KCl at high pressures *Phys. Rev.* B **87** 024302

[325] Zeng Q *et al* 2016 General 2.5 power law of metallic glasses *Proc. Natl Acad. Sci.* **113** 1714–8

[326] Shi C Y *et al* 2013 Formation of an interconnected network of iron melt at Earth's lower mantle conditions *Nat. Geosci.* **6** 971–5

[327] Zeng Q *et al* 2014 Universal fractional noncubic power law for density of metallic glasses *Phys. Rev. Lett.* **112** 185502

[328] Lin Y, Zeng Q, Yang W and Mao W L 2013 Pressure-induced densification in GeO_2 glass: a transmission x-ray microscopy study *Appl. Phys. Lett.* **103** 191908

[329] Gleason A E and Mao W L 2013 Strength of iron at core pressures and evidence for a weak Earth's inner core *Nat. Geosci.* **6** 571–4

[330] Wilkins S W *et al* 1996 Phase-contrast imaging using polychromatic hard x-rays *Nature* **384** 335–8

[331] Langer M, Cloetens P, Pacureanu A and Peyrin F 2012 X-ray in-line phase tomography of multimaterial objects *Opt. Lett.* **37** 2151–3

[332] Liu Y *et al* 2011 Phase retrieval using polychromatic illumination for transmission x-ray microscopy *Opt. Express* **19** 540–5

[333] Kono Y *et al* 2015 X-ray imaging for studying behavior of liquids at high pressures and high temperatures using Paris–Edinburgh press *Rev. Sci. Instrum.* **86** 072207

[334] Nugent K A 2010 Coherent methods in the x-ray sciences *Adv. Phys.* **59** 1–99

[335] Chapman H N and Nugent K A 2010 Coherent lensless x-ray imaging *Nat. Photon.* **4** 833–9

[336] Robinson I and Harder R 2009 Coherent x-ray diffraction imaging of strain at the nanoscale *Nat. Mater.* **8** 291–8

[337] Larson B C *et al* 2002 Three-dimensional x-ray structural microscopy with submicrometre resolution *Nature* **415** 887–90

[338] Grubel G, Madsen A and Robert A 2008 X-ray photon correlation spectroscopy *Soft-Matter Characterization* ed R Borsali and R Pecora (Berlin: Springer) pp 953–95

[339] Style R W *et al* 2015 Stiffening solids with liquid inclusions *Nat. Phys.* **11** 82–7

[340] Jamieson J C and Lawson A W 1962 X-ray diffraction studies in the 100 kbar pressure range *J. Appl. Phys.* **33** 776–80

[341] Jamieson J C, Lawson A W and Nachtrieb N D 1959 New device for obtaining x-ray diffraction patterns from substances exposed to high pressure *Rev. Sci. Instrum.* **30** 1016–9

[342] Merrill L and Bassett W A 1974 Miniature diamond anvil pressure cell for single crystal x-ray diffraction studies *Rev. Sci. Instrum.* **45** 290–4

[343] Weir C, Block S and Piermarini G J 1965 Single crystal x-ray diffraction at high pressures *J. Res. Natl Bur. Stand.* C **69C** 275–81

[344] Mao H-K, Bassett W A and Takahashi T 1967 Effect of pressure on crystal structure and lattice parameters of iron up to 300 kbar *J. Appl. Phys.* **38** 272–6

[345] Guillaume C L *et al* 2011 Cold melting and solid structures of dense lithium *Nat. Phys.* **7** 211–4

[346] Gregoryanz E *et al* 2005 Melting of dense sodium *Phys. Rev. Lett.* **94** 185502

[347] Fujihisa H *et al* 2006 O_8 cluster structure of the epsilon phase of solid oxygen *Phys. Rev. Lett.* **97** 085503

[348] Lundegaard L F *et al* 2006 Observation of an O_8 molecular lattice in the ε phase of solid oxygen *Nature* **443** 201–4

[349] Degtyareva O, Gregoryanz E, Mao H K and Hemley R J 2005 Crystal structure of S and Se up to 160 GPa *High Press. Res.* **25** 17–33

[350] Degtyareva O *et al* 2005 Novel chain structures in group VI elements *Nat. Mater.* **4** 152–5

[351] McMahon M I and Nelmes R J 2006 High-pressure structures and phase transformations in elemental metals *Chem. Soc. Rev.* **35** 943–63

[352] Nelmes R J, Allan D R, McMahon M I and Belmonte S A 1999 Self-hosting incommensurate structure of barium IV *Phys. Rev. Lett.* **83** 4081–4

[353] McMahon M I *et al* 2000 Observation of the incommensurate barium-IV structure in strontium phase V *Phys. Rev.* B **61** 3135–8

[354] McMahon M I, Rekhi S and Nelmes R J 2001 Pressure dependent incommensuration in Rb-IV *Phys. Rev. Lett.* **87** 055501

[355] McMahon M I, Degtyareva O and Nelmes R J 2000 Ba-IV-type incommensurate crystal structure in group-V metals *Phys. Rev. Lett.* **85** 4896–9

[356] Degtyareva O, McMahon M I and Nelmes R J 2004 Pressure-induced incommensurate-to-incommensurate phase transition in antimony *Phys. Rev.* B **70** 184119

[357] McMahon M I *et al* 2006 Different incommensurate composite crystal structure for Sc-II *Phys. Rev.* B **73** 134102

[358] Hejny C and McMahon M I 2003 Large structural modulations in incommensurate Te-III and Se-IV *Phys. Rev. Lett.* **91** 215502

[359] Kenichi T, Kyoko S, Hiroshi F and Mitsuko O 2003 Modulated structure of solid iodine during its molecular dissociation under high pressure *Nature* **423** 971–4

[360] Kume T *et al* 2005 High pressure Raman study of bromine and iodine: soft phonon in the incommensurate phase *Phys. Rev. Lett.* **94** 065506

[361] Hanfland M, Syassen K, Christensen N E and Novikov D L 2000 New high-pressure phases of lithium *Nature* **408** 174–8

[362] McMahon M I, Nelmes R J and Rekhi S 2001 Complex crystal structure of cesium-III *Phys. Rev. Lett.* **87** 255502

[363] Nelmes R J, McMahon M I, Loveday J S and Rekhi S 2002 Structure of Rb-III: novel modulated stacking structures in alkali metals *Phys. Rev. Lett.* **88** 155503

[364] Degtyareva O, McMahon M I, Allan D R and Nelmes R J 2004 Structural complexity in gallium under high pressure: relation to alkali elements *Phys. Rev. Lett.* **93** 205502

[365] McMahon M I, Loa I, Stinton G W and Lundegaard L F 2013 Determining complex crystal structures from high pressure single-crystal diffraction data collected on synchrotron sources *High Press. Res.* **33** 485–500

[366] Merlini M and Hanfland M 2013 Single-crystal diffraction at megabar conditions by synchrotron radiation *High Press. Res.* **33** 511–22

[367] Yamanaka T 2007 Single-crystal structure and electron-density analyses of Earth's interior under high-pressure and high-temperature conditions using synchrotron radiation *Geol. Soc. Am. Spec. Pap.* **421** 175–88

[368] Tse J S *et al* 2014 Pressure-induced changes on the electronic structure and electron topology in the direct FCC → SH transformation of silicon *J. Phys. Chem.* C **118** 1161–6

[369] Ikuta D, Sinogeikin S, Jacobsen S D and Shen G Electron density distributions across the spin transition of iron in ferropericlase unpublished

[370] Li R 2015 The development and application of high pressure single crystal and multigrain diffraction technologies *PhD Thesis* University of Chinese Academy of Sciences

[371] Nisr C *et al* 2012 High resolution three-dimensional x-ray diffraction study of dislocations in grains of $MgGeO_3$ post-perovskite at 90 GPa *J. Geophys. Res.* **117** 2156–202

[372] Belonoshko A B *et al* 2008 Molybdenum at high pressure and temperature: melting from another solid phase *Phys. Rev. Lett.* **100** 135701

[373] Antao S M *et al* 2008 Network rigidity in $GeSe_2$ glass at high pressure *Phys. Rev. Lett.* **100** 115501

[374] Brazhkin V V *et al* 2008 AsS melt under pressure: one substance, three liquids *Phys. Rev. Lett.* **100** 145701

[375] Brazhkin V V *et al* 2008 Nature of the structural transformations in B_2O_3 glass under high pressure *Phys. Rev. Lett.* **101** 035702

[376] Rouxel T, Ji H, Hammouda T and Moréac A 2008 Poisson's ratio and the densification of glass under high pressure *Phys. Rev. Lett.* **100** 225501

[377] Mookherjee M, Stixrude L and Karki B 2008 Hydrous silicate melt at high pressure *Nature* **452** 983–6

[378] Sato T and Funamori N 2008 Sixfold-coordinated amorphous polymorph of SiO_2 under high pressure *Phys. Rev. Lett.* **101** 255502

[379] Sanloup C L, Gregoryanz E, Degtyareva O and Hanfland M 2008 Structural transition in compressed amorphous sulfur *Phys. Rev. Lett.* **100** 075701

[380] Mei Q *et al* 2006 The structure of permanently densified $CaAl_2O_4$ glass *J. Phys. Chem. Solids* **67** 2106–10

[381] Sinn H *et al* 2003 Microscopic dynamics of liquid aluminum oxide *Science* **299** 2047–9

[382] Lee S K, Eng P J and Mao H-K 2014 Probing of pressure-induced bonding transitions in crystalline and amorphous earth materials: insights from x-ray raman scattering at high pressure *Rev. Mineral. Geochem.* **78** 139–74

[383] Hong X *et al* 2007 Density measurements of noncrystalline materials at high pressure with diamond anvil cell *Rev. Sci. Instrum.* **78** 103905

[384] Lee S K *et al* 2005 Probing of bonding changes in B_2O_3 glasses at high pressure with inelastic x-ray scattering. *Nat. Mater.* **4** 851–4

[385] Sheng H W, Ma E, Liu H Z and Wen J 2006 Pressure tunes atomic packing in metallic glass *Appl. Phys. Lett.* **88** 171906

[386] Sheng H W *et al* 2007 Polyamorphism in a metallic glass *Nat. Mater.* **6** 192–7

[387] Soignard E *et al* 2008 High-pressure behavior of As_2O_3: amorphous–amorphous and crystalline-amorphous transitions *Phys. Rev.* B **77** 144113

[388] Zeng Q S *et al* 2007 Anomalous compression behavior in lanthanum/cerium-based metallic glass under high pressure *Proc. Natl Acad. Sci.* **104** 13565–8

[389] Campbell A J *et al* 2007 Partial melting in the iron–sulfur system at high pressure: a synchrotron x-ray diffraction study *Phys. Earth Planet. Inter.* **162** 119–28

[390] Errandonea D, Somayazulu M, Häusermann D and Mao H K 2003 Melting of tantalum at high pressure determined by angle dispersive x-ray diffraction in a double-sided laser-heated diamond-anvil cell *J. Phys.: Condens. Matter* **15** 7635–49

[391] Gavriliuk A G *et al* 2006 Equation of state and high pressure irreversible amorphization in $Y_3Fe_5O_{12}$ *Pisma Zh ETF* **83** 41–5

[392] Goncharov A F, Crowhurst J C, Struzhkin V V and Hemley R J 2008 Triple point on the melting curve and polymorphism of nitrogen at high pressure *Phys. Rev. Lett.* **101** 095502

[393] Goncharov A F *et al* 2009 Dissociative melting of ice VII at high pressure *J. Chem. Phys.* **130** 124514

[394] Lin J F *et al* 2004 High pressure-temperature Raman measurements of H_2O melting to 22 GPa and 900 K *J. Chem. Phys.* **121** 8423–7

[395] Lin J-F *et al* 2005 Melting behavior of H_2O at high pressures and temperatures *Geophys. Res. Lett.* **32** L11306

[396] Stemshorn A K *et al* 2009 Pressure-induced reversible amorphization in superconducting compound $FeSe_{0.5}Te_{0.5}$ *High Press. Res.* **29** 267–71

[397] Swamy V *et al* 2006 Size-dependent pressure-induced amorphization in nanoscale TiO_2 *Phys. Rev. Lett.* **96** 135702

[398] Tschauner O *et al* 2004 Shock-synthesized glassy and solid silica: intermediates between four and six fold coordination *High Press. Res.* **24** 471–9

[399] Lipinska-Kalita K E *et al* 2008 High-pressure structural integrity and structural transformations of glass-derived nanocomposites: a review *J. Phys. Chem. Solids* **69** 2268–73

[400] Lipinska-Kalita K E *et al* 2008 Stability and equation of state of a nanocrystalline Ga–Ge mullite in *a vitro* ceramic composite: a synchrotron x-ray diffraction study *Phys. Rev.* B **77** 134107

[401] Liu H *et al* 2008 Anomalous high-pressure behavior of amorphous selenium from synchrotron x-ray diffraction and microtomography *Proc. Natl Acad. Sci.* **105** 13229–34

[402] Brown K H and Barnett J D 1972 X-ray diffraction studies on liquids at very high pressures along the melting curve. I. Methods and techniques *J. Chem. Phys.* **57** 2009–15

[403] Shen G *et al* 2004 The structure of an amorphous iron at high pressures to 67 GPa measured in a diamond anvil cell *Phys. Earth Planet. Inter.* **143–4** 481–95

[404] Shen G, Prakapenka V B, Rivers M L and Sutton S R 2004 Structure of liquid iron at pressures up to 58 GPa *Phys. Rev. Lett.* **92** 185701

[405] Cadien A *et al* 2013 First-order liquid–liquid phase transition in cerium *Phys. Rev. Lett.* **110** 125503

[406] Mishima O, Calvert L D and Whalley E 1985 An apparently first-order transition between two amorphous phases of ice induced by pressure *Nature* **314** 76–8

[407] Poole P H, Grande T, Angell C A and McMillan P F 1997 Polymorphic phase transitions in liquids and glasses *Science* **275** 322–3

[408] Grimsditch M 1984 Polymorphism in amorphous SiO_2 *Phys. Rev. Lett.* **52** 2379

[409] Williams Q and Jeanloz R 1988 Spectroscopic evidence for pressure-induced coordination changes in silicate glasses and melts *Science* **239** 902–5

[410] Baldini M *et al* 2010 High-pressure EXAFS study of vitreous GeO_2 up to 44 GPa *Phys. Rev.* B **81** 024201

[411] Daisenberger D *et al* 2011 Polyamorphic amorphous silicon at high pressure: Raman and spatially resolved x-ray scattering and molecular dynamics studies *J. Phys. Chem.* **115** 14246–55

[412] Daisenberger D *et al* 2007 High-pressure x-ray scattering and computer simulation studies of density-induced polyamorphism in silicon *Phys. Rev.* B **75** 224118

[413] Brazhkin V V, Popova S V and Voloshin R N 1999 Pressure-temperature phase diagram of molten elements: selenium, sulfur and iodine *Physica* B **265** 64–71

[414] Brazhkin V V, Popova S V and Voloshin R N 1992 Metastable states in simple melts: the kinetics of transitions in liquid Se and S under high pressure *Phys. Lett.* A **166** 383–7

[415] Liu L *et al* 2014 Chain breakage in liquid sulfur at high pressures and high temperatures *Phys. Rev.* B **89** 174201

[416] Katayama Y *et al* 2004 Macroscopic separation of dense fluid phase and liquid phase of phosphorus *Science* **306** 848–51

[417] Wang Y *et al* 2014 Atomistic insight into viscosity and density of silicate melts under pressure *Nat. Commun.* **5** 3241

[418] Blanton T, Misture S, Dontula N and Zdzieszynski S 2011 *In situ* high-temperature x-ray diffraction characterization of silver sulfide, Ag_2S *Powder Diffr.* **26** 114–8

[419] Sposito G *et al* 1999 Surface geochemistry of the clay minerals *Proc. Natl Acad. Sci.* **96** 3358–64

[420] Elliott S R 1991 Medium-range structural order in covalent amorphous solids *Nature* **354** 445–52

[421] Wang L *et al* 2012 Long-range ordered carbon clusters: a crystalline material with amorphous building blocks *Science* **337** 825–8

[422] Vinet P, Rose J H, Ferrante J and Smith J R 1989 Universal features of the equation of state of solids *J. Phys.: Condens. Matter* **1** 1941

[423] Holzapfel W B, Hartwig M and Reiß G 2001 Equations of state for rare gas solids under strong compression *J. Low Temp. Phys.* **122** 401–12

[424] Kuchhal P and Dass N 2003 New isothermal equation of state of solids applied to high pressures *Pramana* **61** 753–7

[425] Duffy T S and Wang Y 1998 Pressure-volume-temperature equations of state *Rev. Mineral. Geochem.* **37** 425–57

[426] Fei Y *et al* 2004 A critical evaluation of pressure scales at high temperatures by *in situ* x-ray diffraction measurements *Phys. Earth Planet. Inter.* **143–4** 515–26

[427] Uchida T, Wang Y, Rivers M L and Sutton S R 2001 Stability field and thermal equation of state of ε-iron determined by synchrotron x-ray diffraction in a multianvil apparatus *J. Geophys. Res.* **B10** 21799–810

[428] Liu L and Bassett W A 1986 *Elements, Oxides, and Silicates—High-Pressure Phases with Implications for the Earth's Interior* (Oxford: Oxford University Press)

[429] Young D A 1991 *Phase Diagrams of the Elements* (Berkeley, CA: University of California Press)

[430] Tonkov E Y and Ponyatovsky E G 2000 *Phase Transformations of Elements under High Pressure* (Boca Raton, FL: CRC Press)

[431] Hazen R M and Finger L W 1982 *Comparative Crystal Chemistry: Temperature, Pressure, Composition, and the Variation of Crystal Structure* (New York: Wiley)

[432] Bassett W A, Takahashi T, Mao H K and Weaver J S 1968 Pressure-induced phase transformation in NaCl *J. Appl. Phys.* **39** 319–25

[433] Liu L-G 1975 Post-oxide phases of olivine and pyroxene and mineralogy of the mantle *Nature* **258** 510–2

[434] Liu L-G 1975 Chemistry and structure of high pressure phase of garnets rich in almandite *Nature* **255** 213–5

[435] Lipp M J, Evans W J, Baer B J and Yoo C-S 2005 High-energy-density extended CO solid *Nat. Mater.* **4** 211–5

[436] Iota V, Yoo C S and Cynn H 1999 Quartzlike carbon dioxide: an optically nonlinear extended solid at high pressures and temperatures *Science* **283** 1510–2

[437] Yoo C S *et al* 1999 Crystal structure of carbon dioxide at high pressure: 'superhard' polymeric carbon dioxide *Phys. Rev. Lett.* **83** 5527–30

[438] Dong J, Tomfohr J K and Sankey O F 2000 Non-molecular carbon dioxide (CO_2) solids *Science* **287** 11a

[439] Iota V and Yoo C-S 2001 Phase diagram of carbon dioxide: evidence for a new associated phase *Phys. Rev. Lett.* **86** 5922–5

[440] Tschauner O, Mao H K and Hemley R J 2001 New transformations of CO_2 at high pressures and temperatures *Phys. Rev. Lett.* **87** 075701

[441] Yoo C-S, Iota V and Cynn H 2001 Nonlinear carbon dioxide at high pressures and temperatures *Phys. Rev. Lett.* **86** 444–7

[442] Iota V *et al* 2007 Six-fold coordinated carbon dioxide VI *Nat. Mater.* **6** 34–8

[443] McMillan P F 2006 Solid-state chemistry—a glass of carbon dioxide *Nature* **441** 823

[444] Santoro M *et al* 2006 Amorphous silica-like carbon dioxide *Nature* **441** 857–60

[445] Klotz S *et al* 2009 The preparation and structure of salty ice VII under pressure *Nat. Mater.* **8** 405–9

[446] Caracas R 2008 Dynamical instabilities of ice X *Phys. Rev. Lett.* **101** 085502

[447] Strässle T *et al* 2007 Experimental evidence for a crossover between two distinct mechanisms of amorphization in ice I*h* under pressure *Phys. Rev. Lett.* **99** 175501
[448] Chou I-M *et al* 1998 *In situ* observations of a high-pressure phase of H_2O ice *Science* **281** 809–12
[449] Struzhkin V V, Goncharov A F, Hemley R J and Mao H K 1997 Cascading Fermi resonances and the soft mode in dense ice *Phys. Rev. Lett.* **78** 4446–9
[450] Goncharov A F *et al* 1996 Compression of ice to 210 gigapascals: infrared evidence for a symmetric hydrogen-bonded phase *Science* **273** 218–20
[451] Hemley R J, Chen L C and Mao H K 1989 New transformations between crystalline and amorphous ice *Nature* **338** 638–40
[452] Goncharov A F *et al* 2005 Dynamic ionization of water under extreme conditions *Phys. Rev. Lett.* **94** 125508
[453] Goncharov A F *et al* 2005 Polymerization of formic acid under high pressure *Phys. Rev. Lett.* **94** 065505
[454] Kumar P, Franzese G and Stanley H E 2008 Predictions of dynamic behavior under pressure for two scenarios to explain water anomalies *Phys. Rev. Lett.* **100** 105701
[455] Tse J S *et al* 2008 X-ray Raman spectroscopic study of water in the condensed phases *Phys. Rev. Lett.* **100** 095502
[456] Goncharov A F, Struzhkin V V, Mao H K and Hemley R J 1999 Raman spectroscopy of dense H_2O and the transition to symmetric hydrogen bonds *Phys. Rev. Lett.* **83** 1998–2001
[457] Mao W L *et al* 2006 X-ray-induced dissociation of H_2O and formation of an O_2–H_2 alloy at high pressure *Science* **314** 636–8
[458] Somayazulu M *et al* 2008 *In situ* high-pressure x-ray diffraction study of H_2O ice VII *J. Chem. Phys.* **128** 064510
[459] Santoro M, Gregoryanz E, Mao H K and Hemley R J 2004 New phase diagram of oxygen at high pressure and temperature *Phys. Rev. Lett.* **93** 265701
[460] Meng Y *et al* 2008 Inelastic x-ray scattering of dense solid oxygen: evidence for intermolecular bonding *Proc. Natl Acad. Sci.* **105** 11640–4
[461] Cynn H *et al* 2001 Martensitic fcc-to-hcp transformation observed in xenon at high pressure *Phys. Rev. Lett.* **86** 4552–5
[462] Hu Q Y *et al* 2015 Polymorphic phase transition mechanism of compressed coesite *Nat. Commun.* **6** 6630
[463] Haines J, Cambon O, Le Parc R and Levelut C 2007 The effect of static disorder on pressure-induced phase transitions and amorphization in α-quartz-type solid solutions *Phase Transit.* **80** 1039–49
[464] Machon D *et al* 2014 Pressure-induced amorphization and polyamorphism: inorganic and biochemical systems *Prog. Mat. Sci.* **61** 216–82
[465] Machon D *et al* 2010 Absence of pressure-induced amorphization in $LiKSO_4$ *J. Phys.: Condens. Matter* **22** 315401
[466] Boehler R, Von Bargen N and Chopelas A 1990 Melting, thermal expansion, and phase transitions of iron at high pressures *J. Geophys. Res.* **95** 21731–6
[467] Heinz D L 1986 *Melting Curve of Magnesian Silicate Perovskite* (Berkeley, CA: University of California Press)
[468] Shen G, Lazor P and Saxena S K 1993 Melting of wustite and iron up to pressures of 600 kbar *Phys. Chem. Mineral.* **20** 91–6
[469] Yang L, Karandikar A and Boehler R 2012 Flash heating in the diamond cell: melting curve of rhenium *Rev. Sci. Instrum.* **83** 063905
[470] Dewaele A, Mezouar M, Guignot N and Loubeyre P 2010 High melting points of tantalum in a laser-heated diamond anvil cell *Phys. Rev. Lett.* **104** 255701
[471] Anzellini S *et al* 2013 Melting of iron at Earth's inner core boundary based on fast x-ray diffraction *Science* **340** 464–6
[472] Aquilanti G *et al* 2015 Melting of iron determined by x-ray absorption spectroscopy to 100 GPa *Proc. Natl Acad. Sci.* **112** 12042–5
[473] Grochala W, Hoffmann R, Feng J and Ashcroft N W 2007 The chemical imagination at work in very tight places *Angew. Chem. Inter. Ed.* **46** 3620–42
[474] Prewitt C T and Downs R T 1998 *High-Pressure Crystal Chemistry* (Washington, DC: Mineralogical Society of America) pp 283–317
[475] Donev A, Stillinger F H, Chaikin P M and Torquato S 2004 Unusually dense crystal packings of ellipsoids *Phys. Rev. Lett.* **92** 255506
[476] McMahon M and Nelmes R 2004 *Z. Kristall.* **219** 742
[477] Bridgman P W 1964 *Collected Experimental Papers* (Cambridge, MA: Harvard University Press)
[478] Nayak A P *et al* 2014 Pressure-induced semiconducting to metallic transition in multilayered molybdenum disulphide *Nat. Commun.* **5** 3731
[479] Rousseau B and Ashcroft N W 2008 Interstitial electronic localization *Phys. Rev. Lett.* **101** 046407
[480] McMahon M I *et al* 2007 Structure of sodium above 100 GPa by single-crystal x-ray diffraction *Proc. Natl Acad. Sci.* **104** 17297–9
[481] Ma Y *et al* 2009 Transparent dense sodium *Nature* **458** 182–5
[482] Matsuoka T and Shimizu K 2009 Direct observation of a pressure-induced metal-to-semiconductor transition in lithium *Nature* **458** 186–9
[483] Matsuoka T *et al* 2014 Pressure-induced reentrant metallic phase in lithium *Phys. Rev.* B **89** 144103
[484] Naumov I I and Hemley R J 2015 Origin of transitions between metallic and insulating states in simple metals *Phys. Rev. Lett.* **114** 156403
[485] Goodenough J B 1960 Direct cation–cation interactions in several oxides *Phys. Rev.* **117** 1442–51
[486] Blanco-Canosa S *et al* 2009 Enhanced dimerization of TiOCl under pressure: spin-Peierls to peierls transition *Phys. Rev. Lett.* **102** 056406
[487] Zhang Y-Z, Jeschke H O and Valentí R 2008 Two pressure-induced transitions in TiOCl: Mott insulator to anisotropic metal *Phys. Rev. Lett.* **101** 136406
[488] Bai L *et al* 2015 Pressure-induced phase transitions and metallization in VO_2 *Phys. Rev.* B **91** 104110
[489] Wentzcovitch R M, Schulz W W and Allen P B 1994 VO_2: Peierls or Mott–Hubbard? A view from band theory *Phys. Rev. Lett.* **72** 3389–92
[490] Laverock J *et al* 2012 Photoemission evidence for crossover from Peierls-like to Mott-like transition in highly strained VO_2 *Phys. Rev.* B **86** 195124
[491] McWhan D B, Rice T M and Remeika J P 1969 Mott transition in Cr-doped V_2O_3 *Phys. Rev. Lett.* **23** 1384–7
[492] Ding Y *et al* 2014 Novel high-pressure monoclinic metallic phase of V_2O_3 *Phys. Rev. Lett.* **112** 056401
[493] Bai L *et al* 2015 Pressure-induced cation–cation bonding in V_2O_3 *Phys. Rev.* B **92** 134106
[494] Cohen R E, Mazin I I and Isaak D G 1997 Magnetic collapse in transition metal oxides at high pressure: implications for the Earth *Science* **275** 654–7
[495] Mao Z *et al* 2011 Iron-rich perovskite in the Earth's lower mantle *Earth Planet. Sci. Lett.* **309** 179–84
[496] Lin J-F *et al* 2006 Sound velocities of ferropericlase in the Earth's lower mantle *Geophys. Res. Lett.* **33** L22304
[497] Crowhurst J C, Brown J M, Goncharov A F and Jacobsen S D 2008 Elasticity of (Mg,Fe)O through the spin transition of iron in the lower mantle *Science* **319** 451–3

[498] Lin J-F *et al* 2007 Electrical conductivity of the lower-mantle ferropericlase across the electronic spin transition *Geophys. Res. Lett.* **34** L16305

[499] Ohta K *et al* 2010 Electrical conductivities of pyrolitic mantle and MORB materials up to the lowermost mantle conditions *Earth Planet. Sci. Lett.* **289** 497–502

[500] Keppler H, Dubrovinsky L S, Narygina O and Kantor I 2008 Optical absorption and radiative thermal conductivity of silicate perovskite to 125 Gigapascals *Science* **322** 1529–32

[501] Goncharov A F, Struzhkin V V and Jacobsen S D 2006 Reduced radiative conductivity of low-spin (Mg,Fe)O in the lower mantle *Science* **312** 1205–8

[502] Zaanen J, Sawatzky G A and Allen J W 1985 Band gaps and electronic structure of transition-metal compounds *Phys. Rev. Lett.* **55** 418–21

[503] Takele S and Hearne G R 1999 Electrical transport, magnetism, and spin-state configurations of high-pressure phases of FeS *Phys. Rev.* B **60** 4401–3

[504] Kobayashi H *et al* 1997 The effect of pressure on the electronic states of FeS studied by Mössbauer spectroscopy *J. Phys.: Condens. Matter* **9** 515

[505] Yoo C S *et al* 2005 First-order isostructural Mott transition in highly compressed MnO *Phys. Rev. Lett.* **94** 115502

[506] Rueff J-P *et al* 2005 Electronic properties of transition-metal oxides under high pressure revealed by x-ray emission spectroscopy *J. Phys.: Condens. Matter* **17** S717

[507] Guo Q *et al* 2002 The phase transitions of CoO under static pressure to 104 GPa *J. Phys.: Condens. Matter* **14** 11369

[508] Mattila A *et al* 2007 Metal-ligand interplay in strongly correlated oxides: a parametrized phase diagram for pressure-induced spin transitions *Phys. Rev. Lett.* **98** 196404

[509] Fischer R A *et al* 2011 Equation of state and phase diagram of FeO *Earth Planet. Sci. Lett.* **304** 496–502

[510] Hemley R J, Struzhkin V V, Cohen R E and Shen G 2015 2.13—measuring high-pressure electronic and magnetic properties *Treatise on Geophysics* 2nd edn, ed G Schubert (Amsterdam: Elsevier) pp 313–49

[511] Aerts C M *et al* 2004 Half-metallic to insulating behavior of rare-earth nitrides *Phys. Rev.* B **69** 045115

[512] Söderlind P 2002 Delocalization and phase transitions in Pr: theory *Phys. Rev.* B **65** 115105

[513] Allen J W and Martin R M 1982 Kondo volume collapse and the $\gamma \rightarrow \alpha$ transition in cerium *Phys. Rev. Lett.* **49** 1106–10

[514] McMahan A K, Scalettar R T and Jarrell M 2009 Screening of 4*f* moments and delocalization in the compressed light rare earths *Phys. Rev.* B **80** 235105

[515] Lipp M J *et al* 2008 Thermal signatures of the Kondo volume collapse in cerium *Phys. Rev. Lett.* **101** 165703

[516] Murphy C A, Jackson J M and Sturhahn W 2013 Experimental constraints on the thermodynamics and sound velocities of hcp-Fe to core pressures *J. Geophys. Res.* **118** 1999–2016

[517] Gleason A E, Mao W L and Zhao J Y 2013 Sound velocities for hexagonally close-packed iron compressed hydrostatically to 136 GPa from phonon density of states *Geophys. Res. Lett.* **40** 2983–7

[518] Struzhkin V V *et al* 2001 Nuclear inelastic x-ray scattering of FeO to 48 GPa *Phys. Rev. Lett.* **87** 255501

[519] Struzhkin V *et al* 2004 Phonon density of states and elastic properties of Fe-based materials under compression *Hyperfine Interact.* **153** 3–15

[520] Kobayashi H *et al* 2004 Phonon density of states and compression behavior in iron sulfide under pressure *Phys. Rev. Lett.* **93** 195503

[521] Lin J-F *et al* 2003 Sound velocities of iron–nickel and iron–silicon alloys at high pressures *Geophys. Res. Lett.* **30** 2112

[522] Mao W L *et al* 2004 Nuclear resonant x-ray scattering of iron hydride at high pressure *Geophys. Res. Lett.* **31** L15618

[523] Lin J F *et al* 2004 Magnetic transition and sound velocities of Fe_3S at high pressure: implications for Earth and planetary cores *Earth Planet. Sci. Lett.* **226** 33–40

[524] Gao L *et al* 2008 Pressure-induced magnetic transition and sound velocities of Fe_3C: implications for carbon in the Earth's inner core *Geophys. Res. Lett.* **35** L17306

[525] Gao L *et al* 2009 Sound velocities of compressed Fe_3C from simultaneous synchrotron x-ray diffraction and nuclear resonant scattering measurements *J. Synchrotron Radiat.* **16** 714–22

[526] Gao L *et al* 2011 Effect of temperature on sound velocities of compressed Fe3C, a candidate component of the Earth's inner core *Earth Planet. Sci. Lett.* **309** 213–20

[527] Lin J-F *et al* 2011 Phonon density of states of Fe_2O_3 across high-pressure structural and electronic transitions *Phys. Rev.* B **84** 064424

[528] Jackson J M, Hamecher E A and Sturhahn W 2009 Nuclear resonant x-ray spectroscopy of (Mg,Fe)SiO_3 orthoenstatites *Euro. J. Mineral.* **21** 551–60

[529] Fultz B *et al* 1997 Phonons in nanocrystalline ^{57}Fe *Phys. Rev. Lett.* **79** 937–40

[530] Muñoz J A *et al* 2011 Positive vibrational entropy of chemical ordering in FeV *Phys. Rev. Lett.* **107** 115501

[531] Muñoz J A *et al* 2013 Electronic structure and vibrational entropies of fcc Au–Fe alloys *Phys. Rev.* B **87** 014301

[532] Winterrose M L *et al* 2011 Dynamics of iron atoms across the pressure-induced Invar transition in Pd_3Fe *Phys. Rev.* B **83** 134304

[533] Winterrose M L *et al* 2009 Pressure-induced Invar behavior in Pd_3Fe *Phys. Rev. Lett.* **102** 237202

[534] Giefers H *et al* 2006 Phonon density of states of Sn in textured SnO under high pressure: comparison of nuclear inelastic x-ray scattering spectra to a shell model *Phys. Rev.* B **74** 094303

[535] Giefers H *et al* 2007 Phonon density of states of metallic Sn at high pressure *Phys. Rev. Lett.* **98** 245502

[536] Klug D D *et al* 2011 Dynamics of Kr in dense clathrate hydrates *Phys. Rev.* B **83** 184116

[537] Tanis E A 2010 Partial phonon density of states of 57-iron and 161-dysprosium in $DyFe_3$ by nuclear resonant inelastic x-ray scattering under high pressure *PhD Thesis* University of Nevada at Las Vegas

[538] Antonangeli D *et al* 2004 Elastic anisotropy in textured hcp-iron to 112 GPa from sound wave propagation measurements *Earth Planet. Sci. Lett.* **225** 243–51

[539] Mao W L *et al* 2008 Experimental determination of the elasticity of iron at high pressure *J. Geophys. Res.* **113** B09213

[540] Badro J *et al* 2007 Effect of light elements on the sound velocities in solid iron: implications for the composition of Earth's core *Earth Planet. Sci. Lett.* **254** 233–8

[541] Liu J, Lin J-F, Alatas A and Bi W 2014 Sound velocities of bcc-Fe and $Fe_{0.85}Si_{0.15}$ alloy at high pressure and temperature *Phys. Earth Planet. Inter.* **233** 24–32

[542] Antonangeli D *et al* 2005 Aggregate and single-crystalline elasticity of hcp cobalt at high pressure *Phys. Rev.* B **72** 134303

[543] Xu R and Chiang Tai C 2005 Determination of phonon dispersion relations by x-ray thermal diffuse scattering *Z. Kristall.* **220** 1009

[544] Gopalakrishnan G *et al* 2013 Thermal diffuse scattering as a probe of large-wave-vector phonons in silicon nanostructures *Phys. Rev. Lett.* **110** 205503

[545] Ding Y *et al* 2006 Determining thermal diffuse scattering of vanadium with x-ray transmission scattering *Appl. Phys. Lett.* **88** 061903

[546] Chigarev N *et al* 2011 Laser ultrasonic measurements in a diamond anvil cell on Fe and the KBr pressure medium *J. Phys.: Conf. Ser.* **278** 012017

[547] Liebermann R C and Li B 1998 Elasticity at high pressures and temperatures *Rev. Mineral. Geochem.* **37** 459–92

[548] Angel R J, Jackson J M, Reichmann H J and Speziale S 2009 Elasticity measurements on minerals: a review *Eur. J. Mineral.* **21** 525–50

[549] Sinogeikin S V and Bass J D 1999 Single-crystal elasticity of MgO at high pressure *Phys. Rev.* B **59** R14141–4

[550] Singh A K, Mao H-K, Shu J and Hemley R J 1998 Estimation of single-crystal elastic moduli from polycrystalline x-ray diffraction at high pressure: application to FeO and iron *Phys. Rev. Lett.* **80** 2157–60

[551] Duffy T S *et al* 1999 Elasticity, shear strength, and equation of state of molybdnum and gold under non-hydrostatic compression to 24 GPa *J. Appl. Phys.* **86** 6729–36

[552] Weidner D J, Li L, Davis M and Chen J 2004 Effect of plasticity on elastic modulus measurements *Geophys. Res. Lett.* **31** L06621

[553] Wang Y, Hilairet N and Dera P 2010 Recent advances in high pressure and temperature rheological studies *J. Earth Sci.* **21** 495–516

[554] Nishihara Y *et al* 2008 Plastic deformation of wadsleyite and olivine at high-pressure and high-temperature using a rotational Drickamer apparatus (RDA) *Phys. Earth Planet. Inter.* **170** 156–69

[555] Miyagi L *et al* 2014 Plastic anisotropy and slip systems in ringwoodite deformed to high shear strain in the rotational Drickamer apparatus *Phys. Earth Planet. Inter.* **228** 244–53

[556] Wenk H-R *et al* 2014 Rietveld texture analysis from synchrotron diffraction images. II. Complex multiphase materials and diamond anvil cell experiments *Powder Diffr.* **29** 220

[557] Wenk H-R and Houtte P V 2004 Texture and anisotropy *Rep. Prog. Phys.* **67** 1367

[558] Merkel S *et al* 2007 Deformation of (Mg,Fe)SiO_3 post-perovskite and D'' anisotropy *Science* **316** 1729–32

[559] Merkel S *et al* 2002 Deformation of polycrystalline MgO at pressures of the lower mantle *J. Geophys. Res.* **107** 2271

[560] Merkel S *et al* 2003 Deformation of ($Mg_{0.9}$, $Fe_{0.1}$)SiO_3 perovskite aggregates up to 32 GPa *Earth Planet. Sci. Lett.* **209** 351–60

[561] Wenk H R *et al* 1997 A deformation-based model for recrystallization of anisotropic materials *Acta Mater.* **45** 3283–96

[562] Shimizu I 1999 A stochastic model of grain size distribution during dynamic recrystallization *Phil. Mag.* A **79** 1217–31

[563] Vaidyanathan R, Bourke M A M and Dunand D C 2001 Texture, strain, and phase-fraction measurements during mechanical cycling in superelastic NiTi *Metall. Mater. Trans.* A **32** 777–86

[564] Kinsland G L and Bassett W A 1977 Strength of MgO and NaCl polycrystals to confining pressures of 250 kbar at 25 °C *J. Appl. Phys.* **48** 978–85

[565] Meade C and Jeanloz R 1990 Yield strength of Al_2O_3 at high pressures *Phys. Rev.* B **42** 2532–5

[566] Meade C and Jeanloz R 1990 The strength of mantle silicates at high pressures and room temperature: implications for the viscosity of the mantle *Nature* **348** 533–5

[567] Klepeis J-H P *et al* 2010 Diamond anvil cell measurement of high-pressure yield strength of vanadium using *in situ* thickness determination *Phys. Rev.* B **81** 134107

[568] He D and Duffy T S 2006 X-ray diffraction study of the static strength of tungsten to 69 GPa *Phys. Rev.* B **73** 134106

[569] Singh A K *et al* 2012 Strength of rhenium from x-ray diffraction experiments under nonhydrostatic compression to 250 GPa *J. Phys.: Conf. Ser.* **377** 012008

[570] Mao H-K *et al* 2006 Strength, anisotropy, and preferred orientation of solid argon at high pressures *J. Phys.: Condens. Matter* **18** S963

[571] Uchida T, Wang Y, Rivers M and Sutton S 2005 Stress and strain measurements of polycrystalline materials under controlled deformation at high pressure using monochromatic synchrotron radiation *Advances in High-pressure Technology for Geophysical Applications* ed Y Wang *et al* (Amsterdam: Elsevier)

[572] Chen J, Weidner D J and Vaughan M T 2002 The strength of $Mg_{0.9}Fe_{0.1}SiO_3$ perovskite at high pressure and temperature *Nature* **419** 824–6

[573] Chen J *et al* 1998 Strength and water weakening of mantle minerals, olivine, wadsleyite and ringwoodite *Geophys. Res. Lett.* **25** 575–8

[574] Weidner D J, Wang Y and Vaughan M T 1994 Yield strength at high pressure and temperature *Geophys. Res. Lett.* **21** 753–6

[575] Mosenfelder J L, Connolly J A D, Rubie D C and Liu M 2000 Strength of $(Mg,Fe)_2SiO_4$ wadsleyite determined by relaxation of transformation stress *Phys. Earth Planet. Inter.* **120** 63–78

[576] Yamamoto J *et al* 2008 *In situ* strength measurements on natural upper-mantle minerals *Phys. Chem. Miner.* **35** 249–57

[577] Manaa M R E 2005 *Chemistry at Extreme Conditions* (Amsterdam: Elsevier)

[578] Yoo C-S 2013 Physical and chemical transformations of highly compressed carbon dioxide at bond energies *Phys. Chem. Chem. Phys.* **15** 7949–66

[579] Torikachvili M S, Bud'ko S L, Ni N and Canfield P C 2008 Pressure induced superconductivity in $CaFe_2As_2$ *Phys. Rev. Lett.* **101** 057006

[580] Lobanov S S *et al* 2015 Stable magnesium peroxide at high pressure *Sci. Rep.* **5** 13582

[581] Kim D Y, Stefanoski S, Kurakevych O O and Strobel T A 2015 Synthesis of an open-framework allotrope of silicon *Nat. Mater.* **14** 169–73

[582] Meng Y *et al* 2006 Hard x-ray radiation induced dissociation of N_2 and O_2 molecules and the formation of ionic nitrogen oxide phases under pressure *Phys. Rev.* B **74** 214107

[583] Somayazulu M, Dera P, Smith J and Hemley R J 2015 Structure and stability of solid $Xe(H_2)_n$ *J. Chem. Phys.* **142** 104503

[584] Brese N E and O'Keeffe M 1991 Bond-valence parameters for solids *Acta Crystallogr.* B **47** 192–7

[585] Scott H P *et al* 2004 Generation of methane in the Earth's mantle: *in situ* high pressure-temperature measurements of carbonate reduction *Proc. Natl Acad. Sci.* **101** 14023–6

[586] Mailhiot C, Yang L H and McMahan A K 1992 Polymeric nitrogen *Phys. Rev.* B **46** 14419–35

[587] Olijnyk H and Jephcoat A P 1999 Vibrational dynamics of isotopically dilute nitrogen to 104 GPa *Phys. Rev. Lett.* **83** 332–5

[588] Goncharov A F *et al* 2000 Optical evidence for a nonmolecular phase of nitrogen above 150 GPa *Phys. Rev. Lett.* **85** 1262–5

[589] Ciezak J A 2008 Metastable polymeric nitrogen: the ultimate green high-energy-density material Army Research Laboratory ARL-TR-4478

[590] Chau R, Michell A C, Minich R W and Nellis W J 2003 Metallization of fluid nitrogen and the Mott transition in highly compressed low-Z fluid *Phys. Rev. Lett.* **90** 245501

[591] Gregoryanz E *et al* 2002 Raman, infrared, and x-ray evidence for new phases of nitrogen at high pressures and temperatures *Phys. Rev.* B **66** 224108

[592] Eremets M I *et al* 2004 Structural transformation of molecular nitrogen to a single-bonded atomic state at high pressures *J. Chem. Phys.* **121** 11296–300
[593] Gregoryanz E *et al* 2006 On the $\varepsilon - \zeta$ transition of nitrogen *J. Chem. Phys.* **124** 116102
[594] Gregoryanz E *et al* 2007 High *P-T* transformations of nitrogen to 170 GPa *J. Chem. Phys.* **126** 184505
[595] Ma Y *et al* 2009 Novel high pressure structures of polymeric nitrogen *Phys. Rev. Lett.* **102** 065501
[596] Eremets M I *et al* 2004 Single-bonded cubic form of nitrogen *Nat. Mater.* **3** 558–63
[597] Mattson W D, Sanchez-Portal D, Chiesa S and Martin R M 2004 Prediction of new phases of nitrogen at high pressure from first-principles simulations *Phys. Rev. Lett.* **93** 125501
[598] Mukherjee G D and Boehler R 2007 High-pressure melting curve of nitrogen and the liquid-liquid phase transition *Phys. Rev. Lett.* **99** 225701
[599] Teter D M and Hemley R J 1996 Low-compressibility carbon nitrides *Science* **271** 53–5
[600] Zerr A *et al* 1999 Synthesis of cubic silicon nitride *Nature* **400** 340–2
[601] Kroll P 2003 Hafnium nitride with thorium phosphide sturcture: physical properties and an assessment of the Hf–N, and Ti–N phase diagrams at high pressures and temperatures *Phys. Rev. Lett.* **90** 125501
[602] Utsumi W *et al* 2003 Congruent melting of gallium nitride at 6 GPa and its applicaiton to single-crystal growth *Nat. Mater.* **2** 735–8
[603] Zerr A, Miehe G and Riedel R 2003 Synthesis of cubic zirconium and hafnium nitride having Th_3P_4 structure *Nat. Mater.* **2** 185–9
[604] Gregoryanz E *et al* 2004 Synthesis and characterization of a binary noble metal nitride *Nat. Mater.* **3** 294–7
[605] Crowhurst J C *et al* 2006 Synthesis and characterization of the nitrides of platinum and iridium *Science* **311** 1275–8
[606] Young A F *et al* 2006 Synthesis of novel transition metal nitrides IrN_2 and OsN_2 *Phys. Rev. Lett.* **96** 155501
[607] Söderlind P and Ross M 2000 Rubidium at high pressure and temperature *J. Phys.: Condens. Matter* **12** 921
[608] Badding J V, Parker L J and Nesting D C 1995 High pressure synthesis of metastable materials *J. Solid State Chem.* **117** 229–35
[609] Miedema A R, de Châtel P F and de Boer F R 1980 Cohesion in alloys—fundamentals of a semi-empirical model *Physica B + C* **100** 1–28
[610] Takemura K and Syassen K 1983 High-pressure phase transitions in potassium and phase relations among heavy alkali metals *Phys. Rev.* B **28** 1193–6
[611] Atou T, Hasegawa M, Parker L J and Badding J V 1996 Unusual chemical behavior for potassium under pressure: potassium–silver compounds *J. Am. Chem. Soc.* **118** 12104–8
[612] Hasegawa M, Atou T and Badding J V 1997 High-pressure synthesis of an alkali metal-transition metal laves phase: KAg_2 *J. Solid State Chem.* **130** 311–5
[613] Shebanova O, Shen G, Yang W and Popov D Pressure-induced electronic transitions and formation of a new intermetallic Rb–Pt compound unpublished
[614] Dubrovinskaia N *et al* 2005 Beating the miscibility barrier between iron group elements and magnesium by high-pressure alloying *Phys. Rev. Lett.* **95** 245502
[615] Dubrovinsky L S *et al* 2001 Pressure-induced invar effect in Fe–Ni alloys *Phys. Rev. Lett.* **86** 4851–4
[616] Dubrovinsky L *et al* 2007 Body-centered cubic iron–nickel alloy in Earth's core *Science* **316** 1880–3
[617] Feng J, Hennig R G, Ashcroft N W and Hoffmann R 2008 Emergent reduction of electronic state dimensionality in dense ordered Li–Be alloys *Nature* **451** 445–8
[618] Matsuoka T *et al* 2008 Pressure-induced superconductivity in $CaLi_2$ *Phys. Rev. Lett.* **100** 197003
[619] Eremets M I, Gavriliuk A G and Trojan I A 2007 Single-crystalline polymeric nitrogen *Appl. Phys. Lett.* **90** 171904
[620] Strobel T A, Somayazulu M and Hemley R J 2009 Novel pressure-induced interactions in silane-hydrogen *Phys. Rev. Lett.* **103** 065701
[621] Alger R S, Anderson T H and Webb L A 1959 Irradiation effects in simple organic solids *J. Chem. Phys.* **10** 695–706
[622] Carlson T A and Krause M O 1972 Relative abundances and recoil energies of fragment ions formed from the x-ray photoionization of N_2, O_2, CO, NO, CO_2, and CF_4 *J. Chem. Phys.* **56** 3206–9
[623] Eberhardt W *et al* 1983 Correlation between electron emission and fragmentation into ions following soft-x-ray excitation of the N_2 molecule *Phys. Rev. Lett.* **51** 2370–3
[624] Samson J A R, Kemeny P C and Haddad G N 1977 Double ionization of CO_2 by photon impact *Chem. Phys. Lett.* **51** 75–6
[625] Pravica M, Bai L, Sneed D and Park C 2013 Measurement of the energy dependence of x-ray-induced decomposition of potassium chlorate *J. Phys. Chem.* A **117** 2302–6
[626] Ceppatelli M, Bini R and Schettino V 2009 High-pressure photodissociation of water as a tool for hydrogen synthesis and fundamental chemistry *Proc. Natl Acad. Sci.* **106** 11454–9
[627] Pravica M *et al* 2012 Note: experiments in hard x-ray chemistry: *in situ* production of molecular hydrogen and x-ray induced combustion *Rev. Sci. Instrum.* **83** 036102
[628] Pravica M *et al* 2011 Note: a novel method for *in situ* loading of gases via x-ray induced chemistry *Rev. Sci. Instrum.* **82** 106102
[629] Kung A *et al* 2011 Compressional, temporal, and compositional behavior of H_2–O_2 compound formed by high pressure x-ray irradiation *J. Chem. Phys.* **134** 234502
[630] Pravica M *et al* 2014 Studies in useful hard x-ray photochemistry: decomposition of potassium halates *J. Phys. Conf. Ser.* **500** 022009
[631] Pravica M *et al* 2014 Carbon tetrachloride under extreme conditions *J. Chem. Phys.* **140** 234502
[632] Chu C W *et al* 1987 Evidence for superconductivity above 40 K in the La–Ba–Cu–O compound system *Phys. Rev. Lett.* **58** 405–7
[633] Bednorz J G and Müller K A 1986 Possible high T_c superconductivity in the Ba − La − Cu − O system *Z. Phys.* B **64** 189–93
[634] Gunnarsson O 1997 Superconductivity in fullerides *Rev. Mod. Phys.* **69** 575–606
[635] Eisaki H *et al* 1994 Competition between magnetism and superconductivity in rare-earth nickel boride carbides *Phys. Rev.* B **50** 647–50
[636] Yamanaka S, Hotehama K-I and Kawaji H 1998 Superconductivity at 25.5 K in electron-doped layered hafnium nitride *Nature* **392** 580–2
[637] Nagamatsu J *et al* 2001 Superconductivity at 39 K in magnesium diboride *Nature* **410** 63–4
[638] Kamihara Y, Watanabe T, Hirano M and Hosono H 2008 Iron-based layered superconductor $La[O_{1-x}F_x]FeAs$ ($x = 0.05$–0.12) with $T_c = 26$ K *J. Am. Chem. Soc.* **130** 3296–7
[639] Drozdov A P *et al* 2015 Conventional superconductivity at 203 kelvin at high pressures in the sulfur hydride system *Nature* **525** 73–6
[640] Li Y *et al* 2014 The metallization and superconductivity of dense hydrogen sulfide *J. Chem. Phys.* **140** 174712
[641] Lorenz B and Chu C W 2005 High pressure effects on superconductivity *Frontiers in Superconducting Materials* ed A V Narlikar (Berlin: Springer) pp 59–497 ch 12

[642] Schilling J S 2001 What high pressure studies have taught us about high-temperature superconductivity *Frontiers of High Pressure Research II: Application of High Pressure to Low-Dimensional Novel Electronic Materials* (*NATO Science Series* vol 48) ed H D Hochheimer *et al* (Berlin: Springer) pp 345–60 ch 26

[643] Yabuuchi T, Matsuoka T, Nakamoto Y and Shimizu K 2006 Superconductivity of Ca Exceeding 25 K at megabar pressures *J. Phys. Soc. Japan* **75** 083703

[644] Gao L *et al* 1994 Superconductivity up to 164 K in $HgBa_2Ca_{m-1}Cu_mO_{2m+2+\delta}$ ($m = 1$, 2, and 3) under quasihydrostatic pressures *Phys. Rev.* B **50** 4260–3

[645] Wu J J *et al* 2013 Pressure-decoupled magnetic and structural transitions of the parent compound of iron-based 122 superconductors $BaFe_2As_2$ *Proc. Natl Acad. Sci.* **110** 17263–6

[646] Kanagaraj M *et al* 2012 Correlation between superconductivity and structural properties under high pressure of iron pnictide superconductor $Ce_{0.6}Y_{0.4}FeAsO_{0.8}F_{0.2}$ *Appl. Phys. Lett.* **100** 052601

[647] Sun L *et al* 2012 Re-emerging superconductivity at 48 kelvin in iron chalcogenides *Nature* **483** 67–9

[648] Chen X-J *et al* 2010 Enhancement of superconductivity by pressure-driven competition in electronic order *Nature* **466** 950–3

[649] Uhoya W *et al* 2014 High pressure effects on the superconductivity in rare-earth-doped $CaFe_2As_2$ *High Press. Res.* **34** 49–58

[650] Liu A Y and Cohen M L 1989 Prediction of new low compressibility solids *Science* **245** 841–2

[651] Tian Y *et al* 2013 Ultrahard nanotwinned cubic boron nitride *Nature* **493** 385–8

[652] Huang Q *et al* 2014 Nanotwinned diamond with unprecedented hardness and stability *Nature* **510** 250–3

[653] Tian Y, Xu B and Zhao Z 2012 Microscopic theory of hardness and design of novel superhard crystals *Int. J. Refract. Met. Hard Mater.* **33** 93–106

[654] Solozhenko V L and Gregoryanz E 2005 Synthesis of superhard materials *Mater. Today* **8** 44–51

[655] Pan Z, Sun H, Zhang Y and Chen C 2009 Harder than diamond: superior indentation strength of wurtzite BN and lonsdaleite *Phys. Rev. Lett.* **102** 055503

[656] Yan X Q *et al* 2009 Depressurization amorphization of single-crystal boron carbide *Phys. Rev. Lett.* **102** 075505

[657] Brazhkin V *et al* 2004 What does 'harder than diamond' mean? *Nat. Mater.* **3** 576–7

[658] Šimůnek A and Vackář J 2006 Hardness of covalent and ionic crystals: first-principle calculations *Phys. Rev. Lett.* **96** 085501

[659] Bundy F P, Hall H T, Strong H M and Wentorf R H 1955 Man-made diamonds *Nature* **176** 51–5

[660] Li Q *et al* 2009 Superhard monoclinic polymorph of carbon *Phys. Rev. Lett.* **102** 175506

[661] Horikawa T, Suito K, Kobayashi M and Oshima R 2005 High-pressure synthesis of superhard material from C_{60} *Japan. J. Appl. Phys.* **44** 3141

[662] Ruoff R S and Ruoff A L 1991 Is C_{60} stiffer than diamond? *Nature* **350** 663–4

[663] Brazhkin V V *et al* 1998 Mechanical properties of the 3D polymerized, sp^2–sp^3 amorphous, and diamond-plus-graphite nanocomposite carbon phases prepared from C_{60} under high pressure *J. Appl. Phys.* **84** 219–26

[664] Burgos E *et al* 2000 New superhard phases for three-dimensional C_{60}-based fullerites *Phys. Rev. Lett.* **85** 2328–31

[665] Yamanaka S *et al* 2006 Electron conductive three-dimensional polymer of cuboidal C_{60} *Phys. Rev. Lett.* **96** 076602

[666] Solozhenko V L *et al* 2009 Ultimate metastable solubility of boron in diamond: synthesis of superhard diamondlike BC_5 *Phys. Rev. Lett.* **102** 015506

[667] Zhao Y *et al* 2002 Superhard B–C–N materials synthesized in nanostructured bulks *J. Mater. Res.* **17** 3139–45

[668] Haines J, Léger J and Bocquillon G 2001 Synthesis and design of superhard materials *Ann. Rev. Mat. Res.* **31** 1–23

[669] Vepřek S 1999 The search for novel, superhard materials *J. Vac. Sci. Technol.* A **17** 2401–20

[670] Friedrich A, Winkler B, Juarez-Arellano E A and Bayarjargal L 2011 Synthesis of binary transition metal nitrides, carbides and borides from the elements in the laser-heated diamond anvil cell and their structure-property relations *Materials* **4** 1648–92

[671] Chung H-Y *et al* 2007 Synthesis of ultra-incompressible superhard rhenium diboride at ambient pressure *Science* **316** 436–9

[672] Cumberland R W *et al* 2005 Osmium diboride, an ultra-incompressible, hard material *J. Am. Chem. Soc.* **127** 7264–5

[673] Dubrovinskaia N *et al* 2007 Superhard nanocomposite of dense polymorphs of boron nitride: noncarbon material has reached diamond hardness *Appl. Phys. Lett.* **90** 101912

[674] Song Y 2013 New perspectives on potential hydrogen storage materials using high pressure *Phys. Chem. Chem. Phys.* **15** 14524–47

[675] Somayazulu M S, Finger L W, Hemley R J and Mao H K 1996 High-pressure compounds in methane-hydrogen mixtures *Science* **271** 1400–2

[676] Mao W L, Struzhkin V V, Mao H-K and Hemley R J 2005 Pressure-temperature stability of the van der Waals compound $(H_2)_4CH_4$ *Chem. Phys. Lett.* **402** 66–70

[677] Vos W L, Finger L W, Hemley R J and Mao H-K 1993 Novel H_2–H_2O clathrates at high pressures *Phys. Rev. Lett.* **71** 3150–3

[678] Mao W L *et al* 2002 Hydrogen clusters in clathrate hydrate *Science* **297** 2247–9

[679] Lokshin K A *et al* 2004 Structure and dynamics of hydrogen molecules in the novel clathrate hydrate by high pressure neutron diffraction *Phys. Rev. Lett.* **93** 125503

[680] Lin Y, Mao W L and Mao H K 2009 Storage of molecular hydrogen in a novel ammonia borane compound at high pressure *Proc. Natl Acad. Sci.* **106** 8113–6

[681] Dodd J L, Halevy I and Fultz B 2007 Valence fluctuations of ^{57}Fe in disordered $Li_{0.6}FePO_4$ *J. Phys. Chem.* C **111** 1563–6

[682] Tan H J, Dodd J L and Fultz B 2009 Thermodynamic and kinetic stability of the solid solution phase in nanocrystalline Li_xFePO_4 *J. Phys. Chem.* C **113** 20527–30

[683] Tan H and Fultz B 2011 Rapid electron dynamics at Fe atoms in nanocrystalline $Li_{0.5}FePO_4$ studied by Mössbauer spectrometry *J. Phys. Chem.* C **115** 7787–92

[684] Mauger L *et al* 2014 Nonharmonic phonons in a-iron at high temperatures *Phys. Rev.* B **90** 064303

[685] Mao H K and Mao W L 2007 2.09—theory and practice—diamond-Anvil cells and probes for high *P-T* mineral physics studies *Treatise on Geophysics* ed G Schubert (Amsterdam: Elsevier) pp 231–67

[686] Sanloup C 2012 High-pressure experimental geosciences: state of the art and prospects. *Bulletin de la Société géologique de France* **183** 175–87

[687] Lin J F, Alp E E and Goncharov A F 2014 15.11—Raman and nuclear resonant spectroscopy in geosciences *Treatise on Geochemistry* 2nd edn, ed H D Holland and K K Turekian (Amsterdam: Elsevier) pp 195–211

[688] Bass J D 2007 2.10—theory and practice—techniques for measuring high *P/T* elasticity *Treatise on Geophysics* ed G Schubert (Amsterdam: Elsevier) pp 269–291

[689] Bass J D and Zhang J S 2015 2.12—theory and practice: techniques for measuring high-*P-T* elasticity *Treatise on Geophysics* 2nd edn, ed G Schubert (Amsterdam: Elsevier) pp 293–312
[690] Weidner D J and Li L 2015 2.14—methods for the study of high *P-T* deformation and rheology *Treatise on Geophysics* 2nd edn, ed G Schubert (Amsterdam: Elsevier) pp 351–68
[691] Decker G 2014 Design study of an MBA lattice for the advanced photon source *Synchrotron Radiat. News* **27** 13–7
[692] Einfeld D 2014 Multi-bend achromat lattices for storage ring light sources *Synchrotron Radiat. News* **27** 4–7
[693] Borland M 2014 Ultra-low-emittance light sources *Synchrotron Radiat. News* **27** 2
[694] Wang L *et al* 2010 Nanoprobe measurements of materials at megabar pressures *Proc. Natl Acad. Sci.* **107** 6140–5

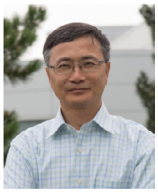

Dr. Guoyin Shen is a Research Scientist at Carnegie Institution for Science. His primary research has been to examine matter under extreme conditions and the behavior of relevant Earth materials at Earth's deep pressure-temperature conditions. Shen's research activities include investigations of phase transformations and melting lines in molecular solids, oxides, silicates and metals; polyamorphism in liquids and amorphous materials; new states of matter and their emergent properties under extreme conditions; and the development of enabling high-pressure synchrotron techniques for advancing high-pressure science. He received his PhD in Mineral Physics in 1994 from Uppsala University in Sweden and worked at the University of Chicago for 9 years. In 2005, Shen joined the High Pressure Collaborative Access Team (HPCAT) at the Advanced Photon Source, Argonne National Laboratory near Chicago as the project manager, and has been the Director of HPCAT since 2010. Under his leadership and working closely with the users' community, HPCAT has become a frontier synchrotron facility for high pressure research, with a myriad of x-ray techniques developed for investigations of the structural, vibrational, electronic, and magnetic properties of materials over a wide range of pressure-temperature conditions, isothermal (de)compression rates, and isobaric heating/cooling rates, addressing questions related to the nature, origins, and evolution of matter, planets and life.

Dr. Ho Kwang Mao is the Director of the Center for High Pressure Science and Technology Advanced Research in China, and a senior staff scientist at the Geophysical Laboratory, Carnegie Institute for Science. He received PhD degree in 1968 from the University of Rocheter, and worked at the Geophysical Laboratory on high-pressure research ever since. As a fundamental physical variable, high pressure alters all states of matter, but, for many years, its effects were poorly understood due to experimental limitations: either the pressure was too low to cause significant changes in liquids and solids, or samples under high pressure could not be subjected to thorough analyses. Advances in diamond-cell technology led by Mao have changed this prospect. He reached static high pressures of several megabars in the laboratory and developed an unprecedented array of laser, synchrotron and electromagnetic probes for accurate investigations of new phenomena through the diamond windows. He has pioneered the establishment of dedicated high-pressure synchrotron beamlines since 1980s and was the founding Director of the HPCAT Sector at the Advanced Photon Scource. With co-workers, Mao has made key discoveries in physics, chemistry, geoscience and materials science, and, in effect, added a new pressure dimension to science and technology.